GROWTH, ELECTRONIC STRUCTURE AND SURFACE MAGNETISM OF LATE TRANSITION METAL AND METAL OXIDE ULTRA-THIN FILMS

By

SUKANTA BARMAN

PHYS05201204012

Saha Institute Of Nuclear Physics, Kolkata

A thesis submitted to the
Board of Studies in Physical Sciences
In partial fulfillment of requirements
for the Degree of

DOCTOR OF PHILOSOPHY

of

HOMI BHABHA NATIONAL INSTITUTE

JULY, 2018

Homi Bhabha National Institute[1]

Recommendations of the Viva Voce Committee

As members of the Viva Voce Committee, we certify that we have read the dissertation prepared by **Sukanta Barman** entitled "**Growth, electronic structure and surface magnetism of late transition metal and metal oxide ultra-thin films**" and recommend that it may be accepted as fulfilling the thesis requirement for the award of Degree of Doctor of Philosophy.

SBhattacharyya 07/01/2019

Chairman - Prof. Satyaranjan Bhattacharyya **Date:**

Guide / Convener - Prof. Krishnakumar S.R. Menon **Date:** 7.01.2019

Sugata Ray

Examiner- Prof. Sugata Ray **Date:** 7/1/19

Member 1- Prof. P.M.G Nambisssan **Date:** 7.1.19

Tapas Kumar Chini 7.1.19

Member 2- Prof. Tapas Kumar Chini **Date:**

Prasanta Karmakar

Member 3- Dr. Prasanta Karmakar **Date:** 07/01/2019

Final approval and acceptance of this thesis is contingent upon the candidate's submission of the final copies of the thesis to HBNI.

I/We hereby certify that I/we have read this thesis prepared under my/our direction and recommend that it may be accepted as fulfilling the thesis requirement.

Date: 7.01.2019

Place: Kolkata

Co-guide (if applicable) **Guide**

---

[1] This page is to be included only for final submission after successful completion of viva voce.

Version approved during the meeting of Standing Committee of Deans held during 29-30 Nov 2013

STATEMENT BY AUTHOR

This dissertation has been submitted in partial fulfillment of requirements for an advanced degree at Homi Bhabha National Institute (HBNI) and is deposited in the Library to be made available to borrowers under rules of the HBNI.

Brief quotations from this dissertation are allowable without special permission, provided that accurate acknowledgement of source is made. Requests for permission for extended quotation from or reproduction of this manuscript in whole or in part may be granted by the Competent Authority of HBNI when in his or her judgment the proposed use of the material is in the interests of scholarship. In all other instances, however, permission must be obtained from the author.

Sukanta Barman

Sukanta Barman

DECLARATION

I, hereby declare that the investigation presented in the thesis has been carried out by me. The work is original and has not been submitted earlier as a whole or in part for a degree / diploma at this or any other Institution / University.

Sukanta Barman

Sukanta Barman

List of Publications arising from the thesis

Journals

1. "Growth optimization and electronic structure of ultrathin CoO films on Ag(001): A LEED and photoemission study", Sukanta Barman, Krishnakumar S.R. Menon, Journal of Crystal Growth, **2018**, 487, 28-33.
2. "Growth and coverage dependent electronic structure of MgO on Ag(001)", Sukanta Barman, Asish K. Kundu and Krishnakumar S.R. Menon, Surface Science, **2018**, 677, 60-67.

Conferences

1. "Incommensurate growth of Co thin film on close-packed Ag(111) surface", Sukanta Barman, Krishnakumar S.R. Menon, AIP Conference Proceedings, **2016**, 1728, 020178, 1-4.

Sukanta Barman

Sukanta Barman

Dedicated to my beloved parents

Acknowledgements

This thesis took more than five years to take shape and it would never have been possible without the help, support and encouragement of many people. I would like to take this opportunity to thank all of them.

I would like to express my heartfelt gratitude to Prof. Krishnakumar S.R. Menon, my thesis supervisor, for introducing me to the Angle-resolved Photoemission Spectroscopy technique and the interesting field of surface magnetism of transition metal oxides. I have been benefited from his valuable advice and scientific discussions. I am grateful to Prof. Satyaranjan Bhattacharyya, Head of the Surface Physics and Material Science division of SINP for his support.

I sincerely acknowledge the engineering and technical staffs at PREVAC sp. zoo. (Ltd.), Poland and VG SCIENTA, Sweden and OCI vacuum Microengineering, Inc. Canada for all technical helps in troubleshooting instrumental problems. A special thanks to Asish da, my senior cum co-author for his fruitful suggestions, discussion and he also helped me a lot to learn instruments handling and data analysis during my initial days in the ARPES laboratory. I am also thankful to Jayanta da and Suvankar da for their help and many scientific and technical discussion. I would also like to thanks my all other labmates, Bibhuti, Smruti, Arunava for academic discussion and creating a friendly and working atmosphere in our group. It's my pleasure to acknowledge all the teaching and non-teaching members in SPMS division, SINP for their support.

Few words are not sufficient to express the unconditional and endless love, support, encouragement of my family.

Kolkata

July, 2018 Sukanta Barman

Contents

SYNOPSIS

Electronic structure and magnetism of correlated transition metal oxides have been a topic of immense interest in surface science research in recent years. Fascinating properties of these two dimensional magnetic systems and their various use in device applications and different fields of material research have made the topic even more interesting. The properties of transition metal and metal oxides in reduced dimensions are quite different from the bulk due to the finite size, interfacial strain, film-substrate chemistry and breaking symmetry in the out-of-plane direction. However, to study the structural and magnetic properties in a reduced dimension, one has to prepare well-ordered stoichiometric surfaces. The most convenient way to prepare a well-ordered insulating oxides surface is to grow a few layers of film on a metallic single crystal substrate which will automatically rule out the possibility of charging effects due to the proximity to the metallic substrate in several surface sensitive techniques such as Low Energy Electron Diffraction (LEED), X-ray Photoelectron Spectroscopy (XPS), Angle-Resolved Photoemission Spectroscopy (ARPES) etc.

To study the electronic structure and surface magnetism of strongly correlated late transition metal oxides in the reduced dimension, we have taken rocksalt CoO as a model system. The small lattice mismatch of CoO ($\sim$4%) with Ag(001) enable us to grow epitaxial films by the reactive evaporation technique. However, to grow the epitaxial stoichiometric films, one requires a detailed understanding of the optimum growth conditions and the dependence of structural and electronic properties on growth parameters because non-equilibrium growth conditions can lead to different growth modes and film structures. Though there are studies available on the electronic structure of CoO thin films [1–3], however, detailed growth optimization and the effect of growth parameters on the surface electronic structures have not been addressed so far in the literature. We have grown CoO films on Ag(001) at different growth conditions by varying the external growth parameter such as substrate temperature, oxygen partial pressure, post-growth treatments and the optimum growth condition was established by investigating the surface geometric and electronic structures of the films using LEED and photoemission spectroscopic techniques, respectively. Coverage-dependent core level and valence electronic structures of the optimized film has been investigated by XPS and ARPES, respectively, are in good agreement with the single crystal results. Moreover, a closer inspection near the Fermi edge reveals the appearance of interfacial states for lower CoO film coverages has been ascribed as a general feature of transition metal oxides as it is also observed for the similar systems such as NiO/Ag(001) [3–5] and MnO/Ag(001) [6].

Nowadays, polar surfaces of metal oxides also grab attention in fundamental research due to their complex stabilization mechanisms [7] which are far from being well understood. The polar surface of CoO(111) consists of alternate stacking of cation (Co^{2+}) and anion (O^{2-}) layers bring a net dipole moment normal to the surface [8] leading to a surface instability. Understanding the stabilization mechanism of polar surfaces even for the structurally simplest (111) surfaces of rock-salt metal oxides remains a challenge. It is almost impossible to cleave the bulk oxide single crystals in the (111) direction and it is often problematic to prepare a stoichiometric and structurally smooth, well-ordered polar oxide surfaces with low defect densities. From a theoretical perspective, it has been shown that to obtain surface stability, the polar surfaces go through different possible processes [9] such as adsorption of contaminations, hydroxylation, reconstructions, faceting, modification of surface electronic structure and charged surface nano-defects. Hassel *et al.* [10] have grown epitaxial CoO(111) film on Co(0001) which is terminated by hydroxyl groups. A grazing incident X-ray diffraction study [11] describes the stabilization of CoO(111) surface by a 50 Å thick spinel Co_3O_4 overlayer on top of the polar surface. We have grown polar CoO(111) surface of various thickness on Ag(111) substrate and study the surface structural properties by LEED and characterize the core and valence band electronic structures using XPS and ARPES techniques, respectively. For the growth of polar CoO(111) on Ag(111), similar growth procedure has been followed as CoO(001) on Ag(001).

Electronic structure of transition metal monoxides like NiO, CoO grabs more attention after the discovery of the cuprate superconductor where the electronic correlations were also found to be very important [12]. There are several exciting aspects of the electronic structure of NiO, CoO such as electron correlation effects, antiferromagnetic (AF) order and translational invariance boosted researchers to look into the matter. The electron correlation causes the breakdown of the one-electron picture of these materials which led the famous Mott-Hubbard picture of insulators [13]. The AF order in these oxides also an important correlation need to be included in the band structure calculation [14]. In the Mott-Hubbard picture, due to the strong Coulomb interaction between the $3d$ electrons leads to an energy gap of several eV between the filled and empty states in the $3d$ band. A combination of Becke's three-parameter exchange functional and the Lee-Yang-Parr correlation functional (B3LYP) calculations [15] predicts the insulating character of CoO correctly in the antiferromagnetically ordered phase with a gap of 3.5 eV. Although this gap is larger than the gap of 2.5 eV as estimated by the combined study of XPS, bremsstrahlung isochromat spectroscopy (BIS), and X-ray-absorption spectroscopy (XAS) [16]. On the other hand, the bulk magnetism of binary (NiO, CoO, MnO) or complex oxides (Cr_2O_3, Mn_3O_4, $BaTiO_3$, *etc.*) are well understood, however, their surface magnetic properties even for the simple binary oxides in the reduced dimension are poorly explored. The possible reason could be the lack of availability of high-quality oxide surfaces to obtain reproducible results and difficulties in the electron spectroscopic measurements due to the insulating nature of most of the bulk oxides. Another issue is that the cleaved surface of oxides single crystals are often with poor crystalline quality consists of terraces. Generally, by the growth of ultrathin film, we can overcome these issues as well as we can expect the new electronic and magnetic properties of the film due to confinement in a thin layer.

The bulk antiferromagnetic properties of MnO, FeO, CoO, NiO were studied using magnetic neutron diffraction, X-ray absorption spectroscopy(XAS), magnetic X-ray dichroism (MXD) *etc.* techniques [17–19]. However, there are very few techniques (SP-STM, XMLD-PEEM, *etc.*) [20–22] available to probe the antiferromagnetism of these oxides in the ultrathin film regime. Long time back, Palmberg *et al.* [23] had first used LEED as a technique to detect surface antiferromagnetism of NiO(100). They have observed half-order spot with a (2×1) translation symmetry produced by exchange scattered low energy electrons below the Néel temperature ensures the presence of antiferromagnetic ordering in the crystal. They have also mentioned, as exchange interaction is very weak relative to Coulomb interactions, the intensity of these spots will be very small (2-6% of integer spot). In recent times, our group is using this technique extensively for different antiferromagnetic systems like NiO [22, 24], MnO [6] thin films, flat monolayer Cr film [25, 26], *etc.*, as a probe of surface antiferromagnetism. It is not only the additional technique for probing antiferromagnetic ordering but also the most direct means for studying the role of exchange in electron scattering. The half-order magnetic spots are detectable even in the ultra-thin submonolayer regime as LEED is a surface sensitive technique. The intensities of the half-order magnetic spots produced by the interaction with incident beam to the spin system are dependent on the spin ordering of the film. The measurement of the temperature dependence of the magnetic half-order spot intensities will give rise to the various information about the surface spin ordering, in-plane and out-of-plane exchange parameters [27] as well as the Néel temperature of the surface/ultrathin films [26, 27]. By fitting the experimental temperature dependence of the square root of half-order intensity variation data with the universal power law of the sublattice magnetization $M_S(T) \sim (1-T/T_N)^\beta$ near T_N, we can get the information about the critical exponent of the magnetization (β) [28]. We probe the surface antiferromagnetic ordering of the ultrathin CoO(001) film using LEED where we observed the evidence of the antiferromagnetism even in the ultrathin film

(0.2 ML) region. Evolution of the surface antiferromagnetic Néel temperature is studied with film coverage as well as on different substrates. In our experiment, the observation of higher Néel temperature relative to its bulk value even in the case of 2 ML CoO on Ag(001) cannot be explained only by considering the superexchange interactions, even though the bulk antiferromagnetism is well understood in terms of the superexchange interactions. We have introduced image charge screening effect [29] along with the superexchange interaction and finite size effects to explain the observed Nèel temperature variation. Moreover, the evidence of short-range magnetic correlations above the Néel temperature has also been observed in our valence band photoemission study.

The physical properties of the correlated oxide systems are determined by a few fundamental quantities. The on-site Coulomb interaction (U) is one of the most important quantities, related to the correlated motion of the electrons between the open transition metal (TM) $3d$ shell and the corresponding multiplet structure. The charge transfer energy (Δ) is another important quantity defined as the energy required to transfer an electron from the O $2p$ to the TM $3d$ orbitals [30]. The values of U and Δ relative to the bandwidth defines the nature, and magnitude of the conductivity gap. Modification of these values can give rise to remarkable changes in the properties of these materials, like changes in the magnitude of the conductivity gap and strength of the various exchange and superexchange interactions [31]. In general, the variation in the strength of these exchange interactions leads to changes in the transition temperatures of various phase transition phenomena. The most convenient way to change these basic electronic structure parameters U and Δ is by growing a few layers of oxide on a metallic substrate or as an oxide/metal multilayers [32–34]. MgO/Ag(001) is an important model system to study the metal-oxides interfaces as they have a small lattice mismatch and grows in a layer-by-layer fashion up to several monolayers (MLs) [35]. Despite their extensive use, understanding of the electronic structure and properties of MgO is still far from satisfactory as the use of electron spectroscopic techniques are hindered due to the charging effects for its insulating nature. Though there are several structural studies performed on this system in the literature, a detailed investigation of the interface and coverage-dependent electronic structure are still limited [36–38]. Altieri *et al.* [33] have demonstrated that the Coulomb (U) and charge transfer (Δ) energies in MgO layers deposited on highly polarizable Ag(001) substrate are reduced significantly from their bulk values. This efficient image potential screening provides a new way to alter different properties and transition temperatures of correlated oxide thin films [29].

The effects of an underlying substrate on the magnetic ordering have been investigated by introducing a spacer MgO layer between CoO and Ag(001). The growth of CoO on MgO(001) results in the changes in lattice strain and more importantly the effects of image charge screening in the presence of less polarizable MgO substrate. Apart from the finite size, strength of superexchange interaction also depends on the interfacial lattice strain and on-site Coulomb (U) and charge transfer (Δ) energies. The strength of the magnetic exchange interaction is strongly related to the magnetic transition temperature. So the antiferromagnetic transition temperature (T_N) of CoO film can be modified by introducing a new substrate. We have observed that Nèel temperature of 2 ML CoO deposited on 10 ML MgO/Ag(001) is found to be $\sim$25 K lower than that of on the Ag(001) substrate. Though at the higher CoO coverage the Nèel temperature saturates at the same value in the near absence of finite size and image charge screening effects. A rough estimation of average antiferromagnetic domain size can be carried out from the FWHM of the half-order LEED spot intensity profiles. The observed domain size of CoO for different films and MgO substrate thickness are in the order of 4-7 nm. The sublattice magnetization curve near surface Nèel temperature shows 3D Ising/Heisenberg behavior ($\beta = 0.33$) at lower film coverage whereas a typical mean field behavior was observed at higher coverage with a critical exponent $\beta = 0.49$.

The exchange scattered half-order magnetic LEED spot describes the surface magnetism of NiO, MnO, CoO, flat monolayer Cr film quite well. After successful investigation of CoO surface magnetism, we have undertaken FeO as another antiferromagnetic model system. Wustite is a stoichiometric iron oxide, and it is unstable under ambient conditions. Therefore, having a stoichiometric FeO is very difficult even in ultrahigh vacuum and often indicated by the notation $Fe_{1-\delta}O$ with $0.04 < \delta < 0.12$ [39]. It has rocksalt structure consists of only Fe^{2+} ions with a lattice parameter 4.33 Å. Bulk FeO exhibits antiferromagnetism below the Nèel temperature of 198 K, with the Fe^{2+} spin arrangement parallel to the (111) planes and antiparallel to the adjacent planes similar to CoO. However, the magnetic axis of FeO is perpendicular to (111) plane unlike the other transition metal oxides [17]. The surface magnetism of FeO is poorly explored due to the lack of a well-ordered stoichiometric surface. We have grown $Fe_{1-\delta}O$ on Ag(001) and MgO/Ag(001) by reactive evaporation and characterized its surface geometric and electronic structure using LEED and photoemission techniques. It is quite challenging to prepare (p×1) FeO(001) surface due to the presence of Fe^{3+} cation defects. Even after preparing (p×1) $Fe_{1-\delta}O$ surface on MgO/Ag(001) the exchange scattered half-order LEED spots have not been observed well below the Nèel temperature. The possible reasons could be the different spin orientation or the presence of Fe^{3+} cation defects in the film which prevents the formation of magnetic half-order spots. This is consistent with the absence of {111} magnetic superstructure peak in neutron diffraction experiment [17].

The thin layer of ferromagnetic Co is a promising candidate for its potential uses such as magnetic sensor in the magnetic storage technology [40], magneto-optical applications [41, 42], *etc.* due to its enhanced magnetic moments at the surface relative to the bulk moments. However, to utilize these properties, one has to better understanding of the crystalline structure of the film and the interfaces. Growths of ultrathin Co film on several closed pack polar substrates are controversially described in the literature [43–45]. The pulsed laser deposition study [46] of Co/Cu(111) system describes the layer-by-layer face-centered cubic (fcc) growth of Co up to 6 ML thickness, above this critical thickness, growth exhibits a structural phase transition from fcc to more energetically favorable hexagonal close-packed (hcp) structure. We have shown the incommensurate 3D island growth of Co thin film on Ag(111) and the coverage-dependent evolution of surface geometric and electronic structure using LEED and XPS studies, respectively. Coverage-dependent valence band electronic structure was probed using ARPES about the $\overline{\Gamma}$ point of the surface Brillouin zone (SBZ) of Co(0001) film.

List of Figures

List of Tables

1

Background and present study

1.1 Introduction

The diverse properties of nanostructured magnetic materials have grabbed the attention of the scientific community for both basic sciences as well as for technological applications since many decades [47–49]. Development of smaller and portable devices with a higher speed of the integrated circuits, catalytic materials, sensor elements, data storage devices, energy storage materials, etc. requires advanced materials and processing techniques [50]. Surfaces, interfaces, thin films, and nanostructures often show fundamentally different structural, electronic, magnetic, and other properties compared to their bulk counterparts. Hence, the preparation and characterization of materials in reduced dimensions are crucial to use them for technological applications. Furthermore, to obtain detailed information about the intrinsic properties of solid surfaces, all the investigation has to be performed in clean surface conditions, i.e., under ultrahigh vacuum (UHV) conditions on a freshly prepared clean surface. In general, thin films are preferred in technological applications over bulk materials due to their reliability, performance, compactness and moreover, due to their exciting properties/characteristics associated with reduced dimensionality which are absent in bulk. The electronic and magnetic properties of thin films not only depends on the geometric structures but also on the growth processes, substrates on which the film is deposited and also on the thickness of the films [47, 51]. Thin films can be defined as solid material extended up to infinity in two directions (x-y) while limited in other direction (z) to a finite thickness. The thickness of the thin films can be from a few Angstroms to more than 10,000 Å, depending on the nature of studies. In general, films having a thickness of few Angstroms to 100 Å are known as ultrathin films, though a precise definition of ultrathin film is difficult. Generally, the film thickness is below some characteristics length scale of the material such as the mean free path of electrons, spin diffusion length, magnetic domain wall width etc., so that new phenomena starts to occur. In this thesis, different thicknesses of late transition metal and metal oxides are grown on metallic as well as on metal supported oxide surfaces to study their surface electronic and magnetic properties. Transition metal oxides manifestly the main areas of interest because of the presence of strong electron-electron correlations, and the effects of it on the electronic structure and magnetism of ultrathin oxide films in close proximity to metallic/oxide substrates. Moreover, it is well-known that the electronic and magnetic properties of low dimensional systems are inseparably connected to the surface structure and are significantly influenced by the different surface induced effects such as change in electronic state occupancy, reduced coordination number of surface atoms, change in magnetic exchange interactions, translational symmetry breaking along out-of-plane directions, etc. Any change in electronic states occupation at the surface leads to the change in the surface magnetic moment as well as changes in the surface electronic structure. Reduced surface atomic coordination results in band narrowing, leading to further changes in magnetic moments of the surface atoms. From the microscopic point of view, one can expect these moments to increase at the surface which has dimensionality somewhere between bulk, monolayer, and isolated atoms as the surface atoms have an uncompensated spin. From the statistical mechanics perspective, the average moment of a magnetic surface at nonzero temperature is expected to decrease relative to that of the bulk. The loss of nearest neighbor in a magnetic surface implies a weakening of the exchange interaction, i.e., the stronger decrease of magnetic order parameter with temperature, moreover, a changed critical behavior if compared to that of the bulk. The translational symmetry breaking along the out-of-plane direction of the surface causes a less quenching of the orbital moment at the surface than in the bulk sample volume. As a consequence, the spin-orbit coupling becomes significant, leading to a large surface magnetic anisotropy that can control the magnetocrystalline anisotropy by orienting the easy magnetization axis along the surface normal of the ultrathin ferromagnetic films.

The intrinsic spin of electron governs the magnetic and other electron correlation phenomena in condensed matter physics. There are several experimental techniques to probe the collective behavior of spins in solids and interaction of spin with other degrees of freedom. Different experimental techniques such as X-ray magnetic scattering and neutron scattering are highly sensitive to the magnetic ordering phenomena and spin structure of the solids in real space. The presence of magnetic order is also expected to affect the electronic structure of the strongly correlated system. Angle-resolved photoemission spectroscopy (ARPES) offers unique information about different magnetic systems through their electronic band dispersions. It measures the energy and momentum of different electronic states and is also sensitive to the magnetic order of the system. In this thesis, ARPES has been extensively used to probe the valence band dispersion at the surfaces as well as the effects of magnetic ordering on the valence band structure of different antiferromagnetic correlated oxide surfaces.

1.2 Correlated oxides: Electronic structure and magnetism

The high degree of correlation between the electronic, magnetic, chemical, structural and morphologic properties makes the preparation and characterization of high-quality well-standardized samples crucial for any study involving low-dimensional systems. In this regards, antiferromagnetic (AFM) transition-metal (TM) monoxides are often preferred for several reasons. First, the high-quality films of these oxides can be grown easily on different substrates, and they have high chemical and mechanical stability. Second, their AFM ordering temperatures (Nèel temperature T_N) are relatively high; for example, bulk NiO and CoO have T_N = 523 K and 291 K, respectively. Another important aspect of TM oxides is their insulating nature resulting from strong inter and intra-atomic electronic correlations. The electron correlation causes the breakdown of the one-electron picture of these oxides which led the famous Mott-Hubbard picture of insulators [13]. Although it has been generally thought that electron-electron correlation effects are of central importance in explaining the electronic structure of these materials, there has been controversy concerning not only the magnitude of the Coulomb interaction but also the nature of insulating gap. Later on, it was recognized that the gap could also be the charge-transfer type. The charge transfer energy (Δ) is defined as the energy required to transfer an electron from ligand ion to the TM ion. According to the relative amplitude of the four parameters, namely, the *d*-*d* Mott-Hubbard repulsion (U), the ligand-metal charge transfer energy (Δ), the TM 3*d* bandwidth (w), and the ligand 2*p* bandwidth (W), the 3*d* TM oxides can be classified within a phase diagram is called the Zaanen-Sawatzky-Allen diagram [52]. In ZSA diagram, the charge-transfer (CT) insulators, Mott-Hubbard insulators are properly classified. Roughly, the early TM monoxides, TiO and VO, fall into the Mott-Hubbard regime while MnO, FeO, CoO, and NiO are antiferromagnetic insulators in the intermediate regime and CuO is an antiferromagnetic charge transfer semiconductor. Electronic band structure of TM oxides is controversially described in several theoretical and experimental studies in the literature [14, 53, 54]. The strong electron correlations and the inclusion of AF order in the theoretical calculations make the investigation even more challenging [55]. The persistence of short-range AF order above the Nèel temperature provides identical ARPES spectra for both antiferromagnetic and paramagnetic phases as observed in general [56, 57]. The magnetic properties of TM oxides are generally governed by the short-range superexchange interaction mediated *via* the oxygen bonds. Due to their insulating nature, itinerant magnetism associated with conduction electrons and dipole-dipole long-range magnetic interaction can be neglected in many cases. Therefore, from the magnetic perspective, TM oxides can be described as the Heisenberg or Ising system as ensembles of well-localized magnetic moments with near-neighbor interactions. Furthermore, TM oxides serve as a model system for the AFM parent compounds after the discovery of high T_c cuprates. Here, the interplay between charge and magnetic ordering is described by Anderson's superexchange theory, which is also described the magnetic properties of TM oxides such as NiO and CoO.

1.3 Oxide-metal interface: Image charge screening

The physical properties of TM oxides are dominated by the strong electron correlations where the single particle picture breaks down as the electron-electron interactions are larger than the one-electron bandwidth [13, 58, 59]. The on-site Coulomb interaction U, related to the correlated motion of the electrons between the open transition metal (TM) $3d$ shell and the corresponding multiplet structures. The charge transfer energy Δ, defined as the energy required to transfer an electron from ligand O $2p$ to TM $3d$, is the most fundamental quantities need to be addressed to understand the electronic structure of TM oxides properly. The value of these parameters relative to the bandwidth defines the physical properties of these oxides such as magnetism, nature, and magnitude of the conductivity gap, etc. A possible way to modify the electronic and structural properties of TM oxides is to change the values of these parameters by any means. The most convenient way to change U and Δ is to grow a few layers of oxide thin films on a metallic substrate or as an oxide/metal multilayer. The reduction of U and Δ values at the insulating oxides/metal interface can be explained by the classical image charge concept [33]. Fig. 1.1 shows the combined electron removal and addition process for a thin film on a metal substrate, showing an open shell (Mott-Hubbard) system for which U = E_I - E_A, where E_I and E_A are ionization potential and electron affinity, respectively. During this process, opposite image charges seem to appear in the metal, so that E_I is reduced and E_A is increased each by the image charge energy E_{image}. This results in the reduction of U by $2E_{image}$. We expect that Δ will also be similarly reduced depending on the change in the Madelung potential. In order to avoid the complexity of correlation effects in $3d$ TM oxides, MgO was chosen due to its closed-shell electronic structure over TM oxides. Moreover, MgO has a similar crystal structure, and lattice parameter to some TM oxides may serve as a model system to investigate the change in basic electronic structure parameters. Further, MgO is used as a substrate for the growth of many TM oxide films and will be important to understand the substrate electronic structure. Most importantly, the reduction of the underlying virtual charge excitation energies of insulating oxides on proximity to the metal substrates can be amplified strength of different exchange and superexchange interactions and thereby the related magnetic transition temperature can be substantially amplified. Extended Anderson expression [52, 60] of superexchange coupling constant $J = -\frac{2t^4}{\Delta^2}(\frac{1}{\Delta} + \frac{1}{U})$, described the dependence of charge excitation energies to the superexchange interaction, where

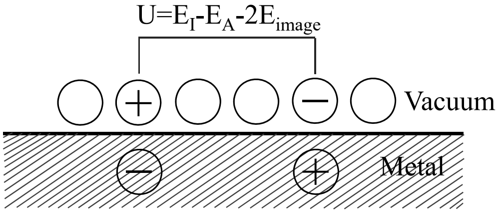

Figure 1.1: Schematic representation of image charge effect for a thin film close to a metal surface, defining on-site Coulomb potential U for an open-shell system. The figure has been adopted from the Ref. [33] and redrawn.

t is the anion $2p$-cation $3d$ transfer integral, Δ is the $2p$-$3d$ charge transfer energy, and U is the on-site $3d$ Coulomb potential. The efficient image charge screening is not only limited to the change in magnetic transition temperature but also exhibit exciting changes in structural and electronic properties, which will be discussed in the relevant chapters of this thesis.

1.4 Magnetism in low dimension

Reduced dimensionality affects the ground state magnetism, resulting in an enhanced magnetic moment and density of states (DOS) near the Fermi level, D(E$_F$). The ground state magnetic properties of a nanostructured low dimensional system can be modified by varying the DOS at the Fermi level. The lower atomic coordination at the surface or in the monolayer films can lead to a reduced overlap of the d electron wave functions and hence a reduction in bandwidth. At the surface of $3d$ metals, the $3d$ bands are narrower, and the states are more localized than the bulk ones. The enhanced D(E$_F$) with the reduced overlap and relatively narrow bands can lead to an enhanced magnetic moment at the surface [see Fig. 1.2]. The enhancement of the magnetic moment is related to the increase in the average exchange splitting ΔE_{ex}. Afterward, it was realized that not only the spin moment but also the orbital magnetic moment could be strongly enhanced with reduced dimensions such as in the case of thin films and surfaces. Since the local moments may be enhanced substantially at the surface/interface, materials with unknown phases, crystal structure, and magnetic anisotropy are to be expected. Finite size effects in low dimensions for both ferromagnetic (FM) and antiferromagnetic (AFM) systems reflect a deviation from bulk properties due to the reduced sample dimensions. Then, the 'so-called' intrinsic effects occur in material systems for which at least one sample dimension is comparable with the intrinsic correlation length scale of the property being considered. Strongly correlated systems like AFM oxides are characterized

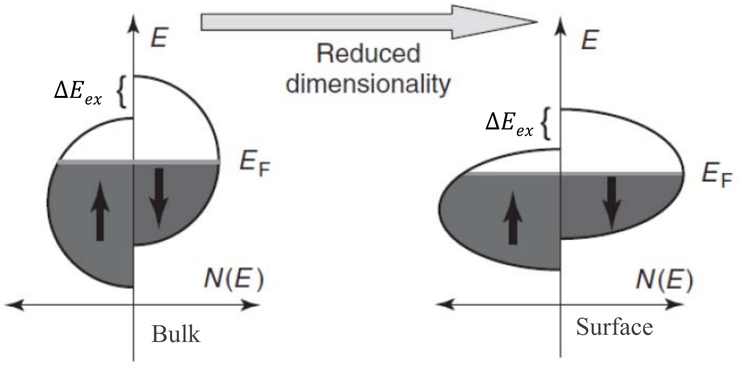

Figure 1.2: Schematic representation of band narrowing and resulting enhanced magnetic moment at the reduced dimension. The figure is adopted from Ref. [61].

by very short correlation lengths, so, intrinsic finite size effects can be observed only in ultrathin films. Further, surface related finite size effects might be caused by the competition between the properties of atoms in the bulk of a sample and those at the surface, possibly originating from the reduced coordination number. For example, surface spins often possess higher magnetocrystalline anisotropy than the ones at the core of the bulk sample due to the reduced symmetry. The environment of a film-substrate interface can also dramatically alter the properties of interface atoms through hybridization, strain, chemical inter-diffusion, etc., which may have significant effects on surface magnetism. The magnetic properties of AFM oxides arise as a consequence of the short-range superexchange interactions mediated *via* the oxygen bonds. So, by changing the in-plane surface lattice strain by means of varying film thickness or by choosing the substrate material with different lattice parameters, AFM superexchange strength and consequently the transition temperature (T_N) can be modified.

Antiferromagnets, unlike ferromagnets, do not exhibit a net magnetization and cannot be readily controlled by, or coupled to an external magnetic field. Thus, antiferromagnetic materials were not well respected from the practical point of view despite many scientific and technological interests. The field of antiferromagnetism become more attractive after the discovery of interlayer exchange coupling in 1986 and giant magnetoresistance (GMR) in 1988-1989 as it has been widely used in magnetic recording, storage, and sensor devices. There are several techniques available for investigating the surface magnetism of ferromagnetic materials such as magneto-optical Kerr effect (MOKE), magnetic force microscopy (MFM), X-ray magnetic circular dichroism (XMCD), spin-polarized scanning tunneling microscopy (SP-STM), spin-polarized photoelectron spectroscopy (SP-PES), etc. However, progress to the field of AFM thin films was partly hindered as limited experimental techniques were available to study surface AFM properties. Though there are a few techniques available for studying antiferromagnetism such as superconducting quantum interface device (SQUID), vibrating sample magnetometer (VSM), etc., they could not be used effectively to study surface/thin film AFM as these techniques are usually bulk sensitive. Neutron diffraction is the most powerful technique to obtain valuable information about the AFM order, but again, they are bulk sensitive. There are a few techniques available for probing surface AFM in the last few decades such as spin-polarized scanning tunneling microscopy (SP-STM) and magnetic exchange microscopy (MExM) which are primarily used for imaging magnetic domains. But these are very specialized techniques and have not been widely used, especially for the study of AFM materials. Nowadays, with the development of ultra-bright synchrotron sources, the X-ray Magnetic Linear Dichroism (XMLD) is a widely used technique for the study of surface antiferromagnetism because it is elemental sensitive and can study surface and buried interfaces.

Thus in general, antiferromagnetism of surface and interfaces has been poorly explored due to the unavailability of suitable laboratory experimental probes. In this thesis, we have used the exchange scattered spots of low energy electron diffraction (LEED) as a method to probe the top layer antiferromagnetism. It is the most direct tool for probing surface AFM and also very sensitive even for sub-monolayer film coverage. This LEED-based technique has been widely used in this thesis to study the surface AFM of CoO ultrathin films were grown on Ag(001), and MgO/Ag(001) substrates. The estimation of antiferromagnetic ordering temperature (T_N) and its variations with film coverage and substrate effects has been studied rigorously. The surface electronic structure and the effects of antiferromagnetic ordering on the electronic structure has been discussed in detail using XPS and ARPES in the respective chapters. In the following subsections, I present a brief overview of the aforementioned antiferromagnetic systems.

1.4.1 Surface antiferromagnetism: CoO/Ag(001)

The bulk CoO has a rock-salt structure with a lattice parameter of 4.26 Å is a well studied antiferromagnet with a bulk Néel temperature (T_N) of 291 K. Even though bulk magnetism of CoO is well understood, the surface magnetism of CoO is poorly explored because of the unavailability of surface sensitive techniques as well as the lack of well-ordered CoO surface. Palmberg *et al.* [23] have first observed the antiferromagnetism of NiO single crystal making use of the exchange scattering in the LEED experiment. The appearance of additional magnetic half-order spots below the Néel temperature due to the exchange scattering of the incoming electron to the atomic electrons by the surface antiferromagnetic lattice has been extensively used in the present thesis to probe the antiferromagnetic ordering of CoO(001) ultrathin films. Different coverages of CoO films were grown on Ag(001), and the variation of Nèel temperature with CoO film coverage has been investigated using temperature dependent half-order spot intensity. The detailed electronic structure in both the AFM and PM phases of CoO have also been investigated, and it is found to be in good agreement with the available theoretical studies.

1.4.2 Antiferromagnetism and Image charge screening: CoO/MgO(001)

The reduction of magnetic transition temperatures is well understood in terms of finite size scaling for ferromagnetic materials in low dimensions [62–64]. However, the observations of enhanced Nèel temperature of metal supported antiferromagnetic oxides in reduced dimensions cannot be explained only considering the finite size effects [29, 65]. The growth of an insulating oxide on a strongly polarizable metallic substrate can cause a reduction of on-site Coulomb (U) and charge transfer energies (Δ) as ascribed by image charge screening [33]. As a consequence, the relevant superexchange interactions, and thus the related antiferromagnetic transition temperature can be substantially amplified. To explore the effects of image charge screening, CoO was grown on Ag(001) supported MgO(001) surface in addition to bare Ag(001) and the corresponding Nèel temperatures were estimated using half-order LEED spots as mentioned above. Enhancement of CoO/Ag(001) Nèel temperature over the bulk values has been explained by the underlying virtual charge excitations due to the image charge screening. After the introduction of less polarizable MgO film of different thickness as a spacer layer between CoO and Ag(001), Nèel temperature reduced significantly relative to that of the bare Ag(001) substrate. Apart from the image charge screening, conventional methods like high pressure, compressive lattice strain can also reduce the interatomic spacing and thus to enhance superexchange interactions and the T_N in many transition metal oxides [66–68]. By introducing MgO as a substrate, lattice strain of CoO can reduce substantially as bulk CoO [4.26 Å], and MgO [4.21 Å] has smaller lattice misfit relative to the Ag(001) [4.08 Å]. However, it has been experimentally observed that for CoO film on MgO, uniaxial lattice strain up to 2% has negligible effects on T_N [69].

Investigation of antiferromagnetic transition temperature (T_N) of CoO(001) and its variation with film coverage and substrate has been performed using exchange scattered low energy electrons ascribed as magnetic half-order LEED spots. Further, a rough estimation of average antiferromagnetic domain sizes can be performed from the width/sharpness of the half-order spots. The evolution of average domain size with film coverage and substrates used can be studied using the surface sensitivity of LEED. Finally, the decay of antiferromagnetic long-range order of CoO film in the critical region can be described in terms of the critical exponent, β, using the universal power law of spontaneous sublattice magnetization given by $M(T) = M(0)(1-T/T_N)^{\beta}$. The exchange scattered half-order LEED spot intensity is proportional to the square of the sublattice magnetization, can be used as the antiferromagnetic order parameter [70]. The value of the critical exponent (β) for different film coverages and substrate will provide more insight into the magnetic ordering of these films.

1.5 Overview of the thesis

This thesis is divided into eight chapters including this chapter on background study. A chapter-wise summary of the thesis with the important findings is given below:

Chapter 2 gives a general introduction to different aspects related to the preparation and characterization of the metal and oxide surfaces studied in this thesis. The cleaning procedure of the surface and the *in-situ* structural characterization using LEED has been discussed. The basics of LEED, photoemission and the theories behind the LEED and ARPES techniques, the different mode of ARPES data collection are also summarized. Few instrument developmental work in the laboratory such as preparation of homemade evaporators and rare-earth getter pump are also described in this chapter.

Chapter 3 has been devoted to the detailed growth and characterization of CoO ultrathin films on Ag(001) and Ag(111). The growths of CoO in different conditions were performed by varying different growth parameters such as substrate temperature, oxygen partial pressure, post-growth annealing conditions, etc. The modifications of structural and electronic properties of CoO films upon growth conditions were monitored using LEED and photoemission techniques, respectively. The well-ordered stoichiometric growth of CoO has been observed at 473 K substrate temperature and 1×10^{-6} mbar oxygen background pressure. The pseudomorphic growth in the initial few layers followed by the gradual strain relaxation close to the bulk lattice and the appearance of the mosaic structure was confirmed by the coverage dependent LEED study. Coverage dependent ARPES study reveals the presence of interfacial states up to 5 ML coverage, originating due to the hybridization between Ag 5*s* band and the Co 3*d* and O 2*p* states.

The polar CoO(111) surface grown on Ag(111) and the stabilization processes were investigated using the surface structures appeared in LEED. Evolution of the faceted and multi-domain surface structures with incident beam energy and film coverage has been investigated. Although there are many processes involved in stabilizing the polar surface, for CoO(111) we find that it is stabilized by the formation of stripe-like faceted structure in the higher film coverages. Redistribution of the electronic density of states also realized from the photoemission spectra of polar CoO(111).

Chapter 4 deals with the growth and coverage-dependent modifications of the electronic structure of MgO films in proximity to the Ag(001) substrate. The appearance of the mosaic structure in LEED has been explained by the formation of misfit dislocations network at the oxide-metal interface. The core level XPS peak shift with film coverage illustrates the change in on-site Coulomb (U) and charge transfer (Δ) energies of MgO layers deposited on highly polarizable Ag(001) substrate. For lower MgO coverage, the presence of O 2*p*-Ag 5*sp* hybridized bands near the Fermi level reduced the MgO bulk band gap substantially as a result of the finite size effects in close proximity to the metallic substrate. The effects of image charge screening have also been reflected in the valence band structure as the bands were shifting towards higher binding energies with increasing coverage while keeping the valence band maxima fixed at the same binding energy. The experimental band dispersions are in good agreement with the available theoretical bulk band dispersions for the 10 ML film, however, a rigorous calculation is necessary to understand the monolayer MgO band structure properly.

Chapter 5 deals with the electronic structure and surface magnetism of CoO film grown on Ag(001). The detailed coverage dependent core and valence band electronic structure has been investigated using XPS and ARPES, respectively. At 20 ML coverage, the band dispersion is almost bulk-like and quite similar to the theoretical bulk band structure. LEED has been employed as a technique for probing surface antiferromagnetism of CoO(001) film grown on Ag(001). The antiferromagnetic ordering temperature has been estimated from the temperature dependence of the half-order LEED spot intensity. Variation of the surface Nèel temperature with film coverage and also the enhanced T_N over bulk value has been discussed using finite size, in-plane lattice strain, image charge screening effects etc. The effect of antiferromagnetic ordering in the electronic structure has been illustrated using the ARPES spectra of CoO(001) for both AFM and PM phases.

Chapter 6 deals with the effects of underlying MgO substrate on the surface antiferromagnetic ordering of CoO(001) films. The variations of Nèel temperature with film and substrate coverage were explained using the combined effects of finite size, in-plane lattice strain, and image charge screening. A rough estimation of the average antiferromagnetic domain size carried out from the width of the Lorentzian fitted half-order intensity profile. The decay of long-range antiferromagnetic order in the critical region has been described using the universal power law of spontaneous sublattice magnetization. The value of critical exponent (β) suggests a 3D Ising/Heisenberg behavior in low film coverage, however, the mean-field behavior is observed in the higher film coverage. The temperature dependent ARPES study reveals the evidence of short-range antiferromagnetic ordering above the Nèel temperature as the valence band electronic structure is quite similar in both PM and AFM phase.

Chapter 7 is devoted to the growth and characterization of Fe_xO film with the aim to investigate the surface antiferromagnetism. The growth of Fe_xO film on Ag(001) has been performed at different growth and post-growth treatment conditions to obtain the well-ordered Fe_xO film with minimum Fe^{2+} deficiency. The estimated stoichiometry of the optimum sample is found to be $Fe_{0.84}O$. Further, Fe_xO was grown on 5 ML MgO/Ag(001) to investigate the effects of MgO spacer layers on the growth of Fe_xO overlayers. The coverage dependent LEED and XPS study show the well-ordered p(1×1) pattern and improved stoichiometry with enhanced Fe^{2+} shake-up satellite intensity, respectively. Temperature-dependent ARPES results show no significant changes in the band dispersion except the small band-edge shift to the higher binding energy at the low temperatures indicating the paramagnetic to antiferromagnetic transition.

Chapter 8 describes the growth of metallic Co layers on Ag(111) using LEED, XPS, and ARPES techniques. Incommensurate well-ordered growth was observed for high coverages followed by the formation of 6-fold Moiré pattern for the lower film coverages. A systematic coverage dependent XPS study confirms the well-ordered growth without any inter-diffusion or surface alloying between the film and substrate. Valence band electronic structure of Co film was probed by ARPES, and the magnetic exchange splitting (0.7 eV) of Co $3d$ bands were observed at $\overline{\Gamma}$ point.

2

Experimental techniques and methods

2.1 Introduction

In this chapter, I will discuss the different experimental techniques which have been employed to perform the experiments presented in this thesis. In this thesis, I will mainly focus on the growth, electronic structure and surface antiferromagnetism of late transition metal and metal oxides ultrathin films. In order to study the electronic and magnetic structure of solid surfaces, the surface must be atomically clean requiring ultrahigh vacuum (UHV) condition during the experiments. Otherwise, the surface will get contaminated by the adsorption of residual gas molecules of atmosphere and the real surface properties will lost. The other advantages of UHV condition are that the cleanness of surface can be maintained for long enough to perform experiment on them and low energy electron and ion based experiments can be performed without undue interference from gas phase scattering. After obtaining the desired UHV condition, thin film can be grown *in situ* on a suitable substrate in the preparation chamber. To do the structural characterization of the grown film, Low Energy Electron Diffraction (LEED) technique has been employed on the sample surface which provides the surface cleanness, crystalline quality and the surface symmetry as well as the different crystallographic symmetry directions can be obtained, necessary for performing the Angle-Resolved Photoemission Spectroscopic (ARPES) measurements.

The detailed elemental analysis of the grown sample and tracing their change of chemical states can be performed using X-ray Photoemission Spectroscopy (XPS). However, for investigating surface electronic valence band structure with high energy and momentum resolution, one has to perform ARPES measurements using suitable ultra-violet photon sources. In photoemission experiments, the most fundamental task is to measure the kinetic energy of emitted electrons, for which the mostly used hemispherical type electron analyzers which will be discussed in this chapter. In addition to the kinetic energy, the precise measurements of the takeoff angle of the photoelectrons from the sample surface can be measured simultaneously using 2D hemispherical analyzer as well. In our laboratory, the photoemission experiments can be performed using He I_α (21.2 eV), He II_α (40.8 eV) and Al K_α (1486.6 eV) photon sources. The synchrotron radiation can be used to perform the photoemission experiments with tunable photon energy available from dedicated synchrotron facilities. It's most important advantages are tunability of photon energy and polarisation of light which can be used for further detailed surface electronic and magnetic structure studies.

In this thesis, the LEED technique has been extended to study the surface antiferromagnetism of the ultrathin films. The coherent magnetic exchange scattering of the low energy electrons from an antiferromagnetic surface spin arrangement produces half-integer order (half-order) magnetic spot in addition to the Coulomb scattered integer-order structural LEED spots [23]. The intensity variation of magnetic half-order LEED spots with temperature has been used to estimate the surface Néel temperature of the sample [23]. The effect of film coverage and the underlying substrate on the surface Néel temperature may also be investigated using this technique. Therefore, we demonstrate that LEED is an essential tool for preliminary surface magnetic studies of single crystalline antiferromagnetic solid surfaces.

2.2 Growth and epitaxy

The modern word ’epitaxy’ comes from the two ancient Greek words, ’epi’ means placed or resting upon and ’taxis’ means arrangement which refers to extended single crystal film formations on top of a crystalline substrate. There are mainly two types of epitaxy; one is the homoepitaxy where film and substrate are the same material while the other one is heteroepitaxy, where film and substrate are composed of different materials. In this thesis, I will emphasis on heteroepitaxial growth of different system like CoO/Ag(001), MgO/Ag(001), CoO/MgO(001), etc. In heteroepitaxy, the lattice constants are necessarily unmatched, and lattice strain develops in the film substrate interface which causes the interfacial defects. The strained growth of film would leads to changes in the electronic, optical, thermal and mechanical properties of the films. Small lattice mismatch between overlayer material and substrate is universally desired for the growth of the well-ordered epitaxial film.

2.2.1 Pseudomorphic and non-pseudomorphic growth

In heteroepitaxy, the lattice parameter of film and substrate differs substantially, the film material may strain to accommodate the substrate lattice structure, then this type of strained epitaxy is called pseudomorphic growth. Pseudomorphic growth generally prevails during the early stages of film formation irrespective of crystal structure or lattice mismatch. It usually occurs between the film-substrate pairs composed of dissimilar materials having the same crystal structure. If the strain accommodation is not possible between film and substrate, that means the film grows with different lattice parameter than the substrate, leads to a non-pseudomorphic growth. For small lattice mismatch, dislocation defects at the interface may be led to the relax-epitaxy and the film relax to its original lattice structure above the interface, whereas higher mismatch may lead to the formation of faceted structures. Such deviations from normal ‘layer-by-layer growth’ would lead to a change in optical,

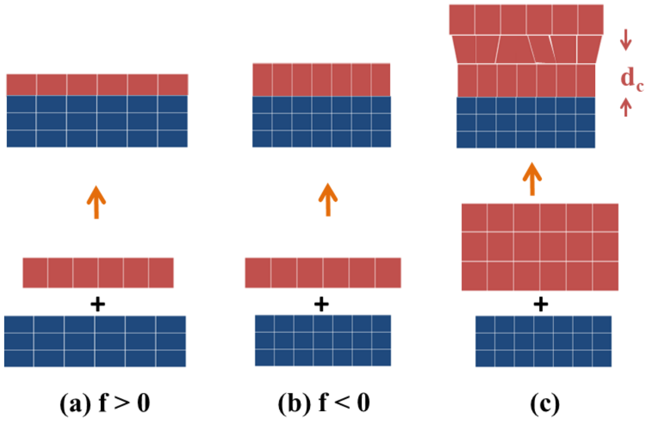

Figure 2.1: (a) In-plane tensile and out-of-plane compressive strain (b) In-plane compressive and out-of-plane tensile strain (c) Lattice parameter relaxation at a critical thickness d$_c$.

thermal, mechanical, electronic and surface magnetic properties of the system. In most cases, the interfacial strain relaxes with the increase of the film thickness, enabling and stabilizing the layered growth. The lattice misfit is defined as

$$f = [a(s) - a(f)]/a(f) \tag{2.1}$$

where a(s) and a(f) refer to the unstrained lattice parameters of the substrate and the film, respectively in their bulk structure. In Fig. 2.1, pseudomorphic growth under a different type of strain represented schematically. If the misfit f $>$ 0 (f $<$ 0), the film undergoes a tensile (compressive) strain in the in-plane direction and a compressive (tensile) strain in the out-of-plane directions. After exceeding the critical thickness d$_c$, the film will relax to its bulk parameters, accompanied by the formation of lattice defects.

For example, in our case, Ag(001) has a lattice parameter of 4.09 Å while bulk CoO(001) has a lattice constant of 4.26 Å. The lattice misfit between these two materials is about 4%, while the lattice misfit between Ag(001) and MgO(001) is about 2.8 %. Thus in principle, both CoO and MgO films can be grown pseudomorpically on Ag(001) in layer-by-layer fashion. Above a critical thickness d_c [which is about 10 ML for MgO(001)/Ag(001) system] the interfacial strain relaxes *via* the creation of misfit dislocations, and the film shows a lattice parameter close to the bulk value. The details will be discussed at the proper context in the different chapters of this thesis.

2.2.2 Different parameters of Molecular Beam Epitaxy (MBE)

'Molecular Beam Epitaxy' is a method where epitaxial metal and metal oxide films are grown on single crystal substrate in layer-by-layer fashion which involves highly controlled evaporation under UHV condition. A good lattice matching is one essential but not sufficient parameter for epitaxial growth. The miscibility gap of the film and substrate material is another vital parameter for MBE growth. If the deposited material is easily dissolved within the substrate forming intermetallic alloy, the probability of forming epitaxial layer is less. Similarly, there should not be any chemical reactivity between these two materials. Another critical parameter is the surface energy of these two materials, which determines whether the deposited material will wet the substrate forming a smooth film or discrete islands. For reactive deposition of oxide films, e.g., the case of CoO where Co is evaporated on Ag(001) in oxygen environment, the oxygen pressure plays a vital role in determining the surface quality as well as the stoichiometry of the deposited film. The temperature of the substrate during growth is another crucial parameter as it controls the mobility of adatoms on the substrate surface. This determines how much substrate surface will be covered by the deposited material. Therefore it is a mandatory part of MBE, to optimize all essential parameters for growth to obtain the best quality epitaxial film. After the deposition, different post-growth treatments can be made to improve the crystalline quality of the epitaxial film.

2.3 Deposition of epitaxial films

The study of surface electronic structure and magnetism requires atomically clean solid surfaces. Since the electronic as well as magnetic structure depends on the film thickness and the studies involving their band dispersion requires atomically uniform and flat films. This demands the highly polished single crystals or cleaved surfaces with large terrace width and low step density. Moreover, clean conditions also imply an *in situ* sample preparation and experimental environment. In order to prepare a good quality smooth substrate surface, a sputter gun is generally used for surface cleaning by Ar^+ ions bombardment, and a heating arrangement to anneal the crystal. The Ar^+ ions bombarded at 0.6-1.2 KeV and 1×10^{-6} mbar pressure are used to clean the surface by removing impurity layers and clusters. It is necessary to anneal the surface to provide mobility to the atoms to recover the thermodynamic stability of the crystal structure. Annealing can be done at different temperatures depending upon the sample and the final structure required. In some cases, when a thermodynamically stable surface is not desired, the sample is quenched from a certain temperature to freeze the stable structure at that temperature. The annealing can be done in several ways, depending on the available setup and desired temperature range: direct Joule heating by passing some current through the sample, radiation heating from a filament near the sample, and electron bombardment by accelerating electrons coming out of a filament onto the back of the sample. The annealing temperature is usually measured using K-type thermocouple attached in the manipulator, in contact with the sample holder. The cooling of the sample can be done, when required, by contact of a sapphire ball on a copper block containing a liquid nitrogen capillary circuit. In this thesis, I have mainly used Ag(001) and Ag(111) as substrates where a couple of sputter-anneal cycles were sufficient enough to prepare a well-ordered surface. The silver crystals were mounted on a particular type of sample holder which were transferred to the preparation chamber through the load-lock chamber.

In the preparation chamber, the substrates were cleaned by Ar^+ ions sputtering (600 eV, 1 μA) for 20 min followed by annealing at 823 K for 30 min. The sputter-anneal cycle repeated for 3-4 times, until a sharp $p(1 \times 1)$ low energy electron diffraction (LEED) pattern has been observed. All the materials in this thesis were evaporated from the water-cooled electron-beam evaporator, resistive heating Knudsen cell and homemade resistive evaporator. The standard thickness calibration was performed by a water-cooled quartz crystal thickness monitor mounted on a linear transfer drive.

2.4 Surface reciprocal lattices

The concepts of lattice and reciprocal lattice on surfaces are very similar to the three-dimensional bulk crystal. The possible 14 Bravais lattices of the bulk are reduced to 5 two-dimensional surface Bravais lattices (square, rectangular, hexagonal, centered rectangular, oblique) which are shown in Fig. 2.2. The two-dimensional lattice is a combination of one of the Bravais lattices and a basis. Since a surface is not truly two dimensional, the basis atoms are not necessarily in one plane. Once the basis is assigned, the two-dimensional point group of the lattice can be found out. The point group will be some subgroup of the highest possible symmetry compatible

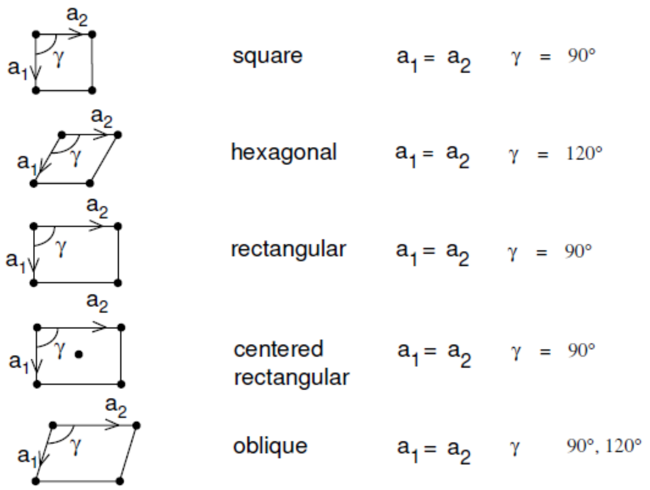

Figure 2.2: (a) Two dimensional Bravais lattice. The figure is taken from the Ref. [71].

with the Bravais lattice under consideration. The final symmetry of the lattice, the space group is formed by a combination of the translation symmetry group (i.e., the Bravais lattice) and the point group. Similar to three-dimensional case, this combination can lead to entirely new symmetry elements which are glide-lines in the two dimensional case. In total, there are 17 different space groups available in two dimension. The reciprocal basis vectors of the surface are defined in the same way as that of the three-dimensional crystal

$$\vec{g_1} = \frac{2\pi(\vec{a_2} \times \vec{n})}{|\vec{a_1} \times \vec{a_2}|}, \vec{g_2} = \frac{2\pi(\vec{a_2} \times \vec{n})}{|\vec{a_1} \times \vec{a_2}|} \tag{2.2}$$

which suggests that,

$$\vec{a_i}\vec{g_j} = 2\pi\delta_{ij} \tag{2.3}$$

and

$$|\vec{g_i}| = \frac{2\pi}{a_i sin\angle(\vec{a_i}, \vec{a_j})}, i, j = 1, 2. \tag{2.4}$$

2.5 Low Energy Electron Diffraction (LEED)

Low energy electrons are being used in surface science as similar to X-rays for the bulk. There are two well-known reasons for which electrons are preferred over X-rays. Firstly, the inelastic mean free path of electrons in solids are small; therefore any technique using such electrons is rather surface sensitive. Secondly, the de Broglie wavelength of electron $\lambda = h/p$ is comparable with the typical interlayer distance in crystals, and thus diffraction phenomena are to be expected from the crystal surface. However, to determine the qualitative surface structure using electrons instead of X-rays leads to some difficulties such as the electrons interact with the solid much more strongly relative to X-rays. As a result, electron wave refracts at the crystal-vacuum interface, and even worse, it leads to a high degree of multiple scattering which contributes to the inelastic background of the diffraction pattern. As we shall see below, there are two major ways to utilize LEED technique for surface studies. The first way is to extract some information from the pure inspection of the surface diffraction pattern. It gives direct and immediate qualitative information about surface order and crystalline quality. The analysis of spot positions yields information on the size, symmetry, and rotational alignment of the adsorbate unit cell relative to the substrate unit cell. The second way is the quantitative structure determination which is more difficult. Here the intensities of the different diffracted beam have to be recorded as a function of incident electron beam energy to generate so-called I-V curve and compare them with sophisticated multiple scattering calculations for a model system. This model system has to be tuned until there is a good agreement between calculated and measured I-V curve is achieved. Despite this complicated procedure, LEED is the most powerful tool for quantitative surface structure determination of solids. Although experiments presented in this thesis, LEED is mainly used to check the surface order, symmetry and to extract information about overlayer and adsorbate structures.

2.5.1 Theory

The high surface sensitivity of LEED is due to the strong interaction between low energy electrons and solids. Upon penetrating the crystal, primary electrons will lose kinetic energy due to inelastic scattering processes such as plasmon and phonon excitations as well as electron-electron interactions. In cases where the detailed nature of the inelastic processes is unimportant, they are commonly treated by assuming an exponential decay of the primary electron beam intensity, I_0, in the direction of propagation:

$$I(d) = I_0 e^{-d/\lambda(E)} \tag{2.5}$$

Where ‘d’ is the penetration depth and λ(E) indicates the inelastic mean free path (IMFP), defined as the path an electron can travel till its intensity has reduced to 1/e times to its initial intensity. While the inelastic scattering phenomena and consequently the mean free path of electron depend mostly on the energy, it is almost independent of the material [see Fig. 2.3]. The mean free path of electron turns out to be minimum (5-10 Å) in the energy range of 20 - 200 eV. This effective attenuation suggests that the electron beam probes only a few atomic layers and as a result, the contribution of deeper atoms to the diffraction gradually decreases. To obtain the additional quantitative information concerning the surface, namely atomic coordination defining bond length, bond angles, adsorption sites, etc. it is essential to study the beam intensities. In order to correlate the beam intensities and atomic positions, we must know the basic electronic scattering dynamics and the characteristics of electron diffraction at LEED energies.

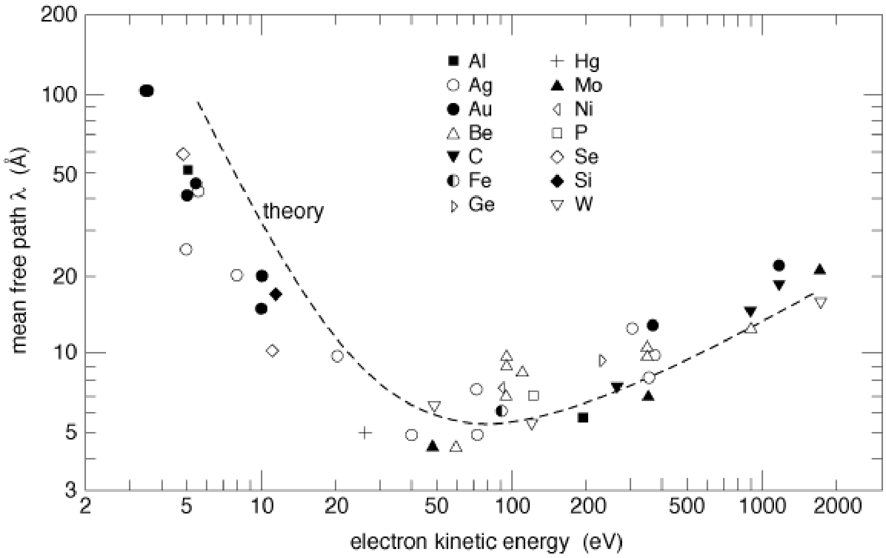

Figure 2.3: Universal curve of mean free path (IMFP) for the inelastic scattering of electrons in a solid [72]. The figure is taken from the Ref. [71].

2.5.1.1 Kinematic theory: Single scattering

Kinematic diffraction is defined as the phenomena where electrons impinging on a crystal surface are diffracted elastically only once by that surface. In the theory, the electron beam is represented as a plane wave with the de Broglie wavelength of electron.

$$\lambda = \frac{h}{\sqrt{2mE}} \tag{2.6}$$

Let us consider a monoenergetic electron beam impinging on a surface. The beam is represented by a plane wave [73] which is described by,

$$A_i = A_0 \exp\left(i\vec{k_0}.\vec{r}\right) \tag{2.7}$$

where A$_i$ is the amplitude of the incident wave, A$_0$ is a constant, $\vec{k_0}$ is the incident wave vector, and $\vec{r}$ is a position vector. If multiple scattering is neglected, the amplitude of a diffracted beam is represented by:

$$A_s = A_0\Big[\sum_n \alpha f_n(\vec{s}) \exp\left(i\vec{s}.\vec{r_n}\right)\Big] \exp\left(i\vec{k_{out}}.\vec{r}\right) \tag{2.8}$$

where f$_n(\vec{s})$ is the atomic scattering factor for the nth atom located at position $\vec{r_n}$, $\vec{s}$ = $\vec{k_{out}}$ - $\vec{k_0}$ is the momentum transfer, and $\vec{k_{out}}$ is the wave vector of the scattered wave (α is a constant). However, the kinematic theory, which is based on single scattering phenomena, is inadequate. In real electron diffraction experiments, the electron pass through multiple scattering and therefore a detailed idea of surface structure cannot be obtained from the kinematic model of LEED.

2.5.1.2 Dynamical theory: Multiple scattering

Dynamical theory, based on multiple scattering picture, has had its most profound impact in the area of surface structure determination, and, consequently, LEED has been used to determine a large number of surface structures for a wide variety of materials. The energy dependence of the beam intensities can theoretically be calculated for a proposed structure and its comparison with experimental LEED I-V data gives an idea about the detailed structure of the material [73].

2.5.2 LEED: Instrumental configurations

The operating principle of a standard LEED setup is schematically illustrated in Fig. 2.4. In a typical LEED experiment, monochromatic electrons (generally within 20-200 eV) are accelerated from an electron gun and focused with a lens system, which falls normally on the sample surface. The electron gun for LEED has been designed in such a way that minimum light from the electron gun cathode will come out in the UHV chamber. Generally, a thoriated tungsten filament has been used as cathode, which is heated and therefore emits electrons. These electrons are accelerated by a variable voltage and focused on the sample surface, where they are diffracted and traverse in the vacuum toward the fluorescent screen. The Wehnelt cylinder in the lens system acts as an electrostatic aperture between the cathode and the anode. It is on the same or on negative potential with respect to the cathode and regulates

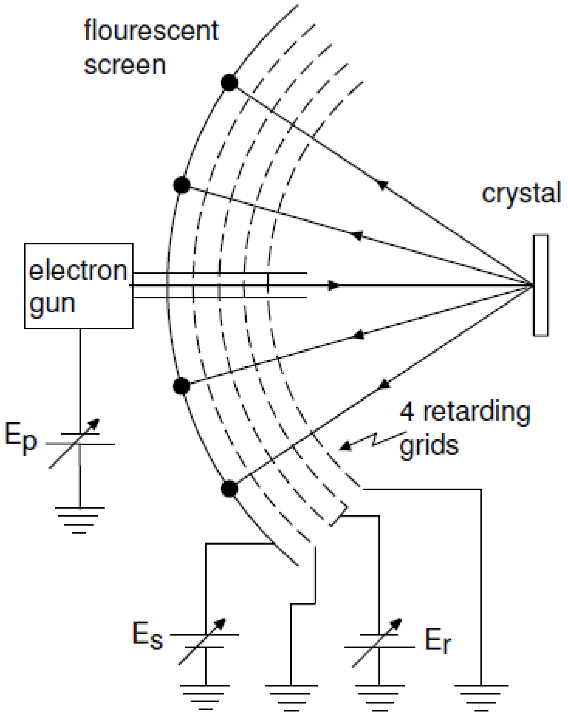

Figure 2.4: Schematic of a typical 4-grid LEED setup [71].

the penetration of the anode potential into the direction of the cathode. An increase of the Wehnelt voltage leads to a narrowing of the electron beam and the sharpness of the diffraction spots can be improved. In order to obtain a sharp focus over a broad range of energies, the lens voltages have to be varied as a function of energy. The secondary electrons and electrons which are inelastically scattered by the sample surface can be kept away from the fluorescent screen by applying a negative voltage to the suppressor grids. A set of four gold coated molybdenum grids at different places in front of the fluorescent screen serves as energy filter. These grids prevent access of low energy secondary electrons to the detection area, where the diffraction pattern of the Bragg's diffraction spots can be observed. The first grid from the sample side is at ground potential to ensure a field-free region between the sample and the first grid. The next two grids are set at the so-called retarding voltage to minimize the contribution from inelastically backscattered electrons. This voltage is slightly lower relative to the kinetic energy of the electrons produced by the gun. Two grids have been used at the same retarding voltage, so that it repels almost all the inelastically scattered electrons. The elastically scattered electrons pass through the next grid, which is set to the ground potential again and are then accelerated toward the fluorescent screen that is generally set to a high positive voltage between 4 to 5 kV. This results in the screen to glow with intensity at every point on the screen is proportional to the incident electron flux which produces a visual map of the electron diffraction pattern. Thus, the elastically backscattered electrons give rise to the diffraction spots that are imaged on a phosphorous screen yielding reciprocal lattice of the surface. Behind the screen, there is a transparent window so that the LEED pattern can be directly observed or recorded with a Peltier cooled charge-coupled device (CCD) camera which is interfaced with a computer in order to acquire frames of diffraction patterns with different exposure, acquisition time and gain parameters. The typical beam sizes are of the order of $\sim$1 mm^2, and has a coherence length of several hundreds of Angstroms. Apart from well-ordered surface, LEED experiments also require UHV and extremely clean surface (free from any surface contamination). For this reason, surface preparation is generally performed *in situ* by sputtering and annealing or by other methods like flashing, cleaving *etc.* We can directly map the surface reciprocal space with LEED. It is interesting to know that, not only the bulk termination of the crystal structure but any surface reconstruction like atomic step arrays or adsorbate induced structures can be studied using LEED.

2.5.3 Ewald's construction

LEED provides a two-dimensional diffraction pattern due to the interference of backscattered electron from a well-ordered surface. The resulting diffraction pattern is a two-dimensional reciprocal space representation of the surface unit cell periodicity. Any two-dimensional surface can be considered as a member of three-dimensional crystal where in the third dimension (z-direction), the real-space periodicity is infinite which means that in reciprocal space the lattice points have to be infinitely close to each other. This leads to reciprocal lattice rods instead of points. As a result, an arrangement of net points which is periodic in two dimensions may be considered as an ensemble of parallel rods of scatterers with directions [hk] and mutual distances d_{hk}. In this case, interference maxima are to be expected in directions given by:

$$n\lambda = d_{hk}(\sin\phi - \sin\phi_\circ) \tag{2.9}$$

where $\phi_\circ$ is the incident angle of the impinging electrons and ϕ that of the backscattered electrons. Intensity maxima appear at points which satisfy the two dimensional Laue condition. These can be explained using Ewald's construction [see Fig. 2.5]. The radius of the Ewald's sphere represents the wave vector of the incident electron beam, and diffracted beams appear wherever a reciprocal lattice rod intersects the Ewald's sphere. The diffracted pattern thus reflects the symmetry of the surface unit mesh, and the separation between the reflexes is inversely proportional to the interatomic distance. As the incident energy is increased, so the sphere radius will also increase. Consequently, the number of diffraction beams increases and the angle between each diffraction beam decreases. The diffraction pattern will appear to condense towards the specular beam. In order to determine the structure factor, *i.e.*, the number and positions of atoms within the unit mesh, spot intensities must be analyzed. It is experimentally simple to change the incident electron energy in LEED by changing the electron accelerating voltage V, and so to obtain a record of the intensity of a particular spot as a function of voltage V. In this way, for any particular LEED spot, an intensity-voltage profile is conveniently obtained, the so-called LEED I-V spectrum.

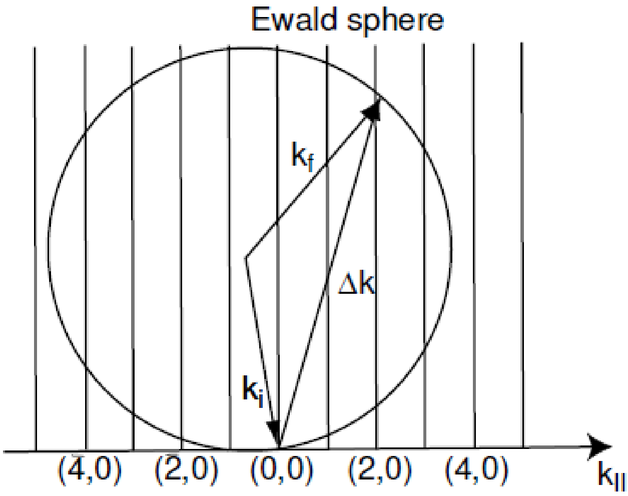

Figure 2.5: Ewald's sphere construction in surface. The incident plane wave falling on the crystal with a wave vector $\vec{k_i}$ and get diffracted with a wave vector $\vec{k_f}$, where, $\vec{\Delta k} = \vec{k_f} - \vec{k_i}$ [71].

2.5.4 Overlayer notation

The phenomena of surface reconstruction and ordered surfaces make it necessary to have a nomenclature to describe the periodicity and symmetry of the surface with respect to that of the bulk. So, any overlayer surface formed on a substrate can be expressed in terms of substrate lattice vectors to establish a relation between them. In this case, the overlayer lattice vectors $\vec{b_1}$ and $\vec{b_2}$ can be expressed in terms of the substrate lattice vectors, $\vec{a_1}$ and $\vec{a_2}$. The mostly used nomenclature of surface structures was proposed by Wood [74]. The surface structure is given by

$$N\left(\frac{b_1}{a_1} \times \frac{b_2}{a_2}\right) R\theta \tag{2.10}$$

where N ='p' or 'c' for primitive or centered cells, respectively, and θ is the angle by which the surface vectors have to be rotated with respect to those of the bulk [see Fig. 2.6]. If the lengths $|\vec{b_1}| = m|\vec{a_1}|$ and $|\vec{b_2}| = n|\vec{a_2}|$ and the basis vectors $\vec{a_1}$ and $\vec{a_2}$ are parallel to the vectors $\vec{b_1}$ and $\vec{b_2}$, respectively, then the overlayer can be termed as $p(m \times n)$ where p denotes that overlayer cell is primitive. But, if the overlayer lattice is rotated by angle θ with respect to substrate while overlayer lattice vectors subtending the same angle as that of substrate, the overlayer may be termed as $(m \times n)\mathrm{R}\theta°$. The Woods nomenclature has the advantage of simplicity. However, it can not describe all surface structures because the rotation angle might not be the same for both vectors. Some examples for the application of the Woods nomenclature are given in Fig. 2.7. Note that despite its lack of generality the Woods nomenclature is still useful because many structures can be described by it. A more general description of the surface structure is the so-called matrix notation, where

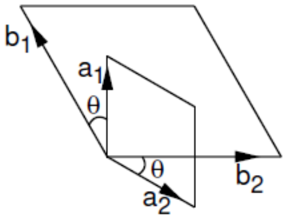

Figure 2.6: The Wood notation for surface lattices [71].

one writes,

$$\begin{aligned} \vec{b_1} &= m_{11}\vec{a_1} + m_{12}\vec{a_2} \\ \vec{b_2} &= m_{21}\vec{a_1} + m_{22}\vec{a_2} \end{aligned} \tag{2.11}$$

This equation can be expressed in matrix notation as follows

$$\begin{bmatrix} \vec{b_1} \\ \vec{b_2} \end{bmatrix} = \begin{bmatrix} m_{11} & m_{12} \\ m_{21} & m_{22} \end{bmatrix} \begin{bmatrix} \vec{a_1} \\ \vec{a_2} \end{bmatrix} \tag{2.12}$$

The matrix which relates the substrate and overlayer lattice vectors are defined as M,

$$M = \begin{bmatrix} m_{11} & m_{12} \\ m_{21} & m_{22} \end{bmatrix} \tag{2.13}$$

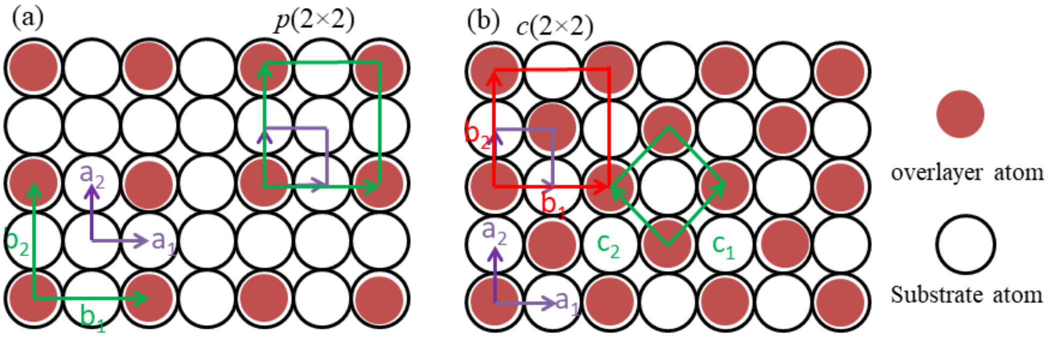

Figure 2.7: Overlayer superstructure a) $p(2\times2)$ on square symmetry substrate [ex. fcc(001)] where the $p(2\times2)$ primitive unit cell is denoted by green box. (b) $c(2\times2)$, where the unit cells (non-primitive and primitive) are shown by the red and green boxes, respectively, and the structure corresponding to the primitive unit cell is defined as $(\sqrt{2}\times\sqrt{2})$R 45°.

Here, we will show a few overlayer structures and their matrix form. Let us consider a substrate surface atomic arrangement having lattice vector $\vec{a_1}$ and $\vec{a_2}$ as shown in Fig. 2.7, where the brown circles are the overlayer atoms. Now the lattice vector of the overlayer are chosen as $\vec{b_1}$ and $\vec{b_2}$ and both are in the same direction as substrate lattice vectors, but twice in length. According to Woods notation it is defined as $p(2{\times}2)$ structure, denoted by green box. Unit cell of the overlayers and the substrate are shown in Fig. 2.7(a). In matrix formalism,

$$M = \begin{bmatrix} 2 & 0 \\ 0 & 2 \end{bmatrix} \tag{2.14}$$

for $p(2{\times}2)$ structure. If there is a center atom in every overlayer unit cell of $p(2{\times}2)$ structure then that structure is defined as a $c(2{\times}2)$ structure [see Fig. 2.7(b)]. The $c(2{\times}2)$ unit cell is indicated by the red box. On the other hand, if we consider $\vec{c_1}$ and $\vec{c_2}$ as the lattice vectors of overlayer then it is evident form Fig. 2.7(b) that both the overlayer vectors are $\sqrt{2}$ times in length compared to substrate and rotated by 45° so the same pattern can also be called $(\sqrt{2} \times \sqrt{2})$R 45°. This $(\sqrt{2} \times \sqrt{2})$R 45° unit cell is shown by the small green box. For the $c(2{\times}2)$ structure,

$$M = \begin{bmatrix} 1 & 1 \\ -1 & 1 \end{bmatrix} \tag{2.15}$$

2.6 Photoemission spectroscopy

Photoemission spectroscopy (PES) is an efficient experimental technique widely used in the study of electronic structure of solids, surfaces, electron spectroscopy for chemical analysis (ESCA), and catalytic studies *etc.* [75–79]. In photoemission experiment, an electron is emitted from occupied electronic level of the solid after being exposed to sufficiently energetic photon beam whose energy is analyzed by the electron energy analyzer. The phenomena of photoemission was first observed by Hertz [80] in 1887 and later explained by Einstein [81] in 1905 by invoking the concept of quantum nature of light. However, it took a long time for photoelectric effect to get established as a technique to investigate the states of an electron inside a solid. Kai Siegbahn [82, 83] was awarded the Nobel Prize in Physics in 1981 for the development of electron spectroscopy. In photoemission experiment, the kinetic energy of the emitted photoelectrons usually varies from few eV to few hundred eV, depending on the incident photon energy. The surface sensitivity of the technique depends on the electron mean free path of the typical photoelectron in solid ranges from 5-30 Å [72] as shown in Fig. 2.3. The photon energy can be varied using different sources such as gas discharge lamp, X-ray gun or a synchrotron radiation source. Depending on the incoming photon energy, photoemission technique can be classified as follows: in ultraviolet regime (5 to 100 eV, UPS), soft x-ray regime (100 to 1000 eV, SXPS), x-ray regime (>1000 eV, XPS) or in the hard x-ray regime (>3000 eV, HAXPS). The emitted photoelectrons are analyzed with respect to their kinetic energy E_{kin} and momentum k in electrostatic analyzer. In this simple picture, photoemission spectroscopy (PES) measures the electronic states of the sample under consideration. From the momentum and energy distribution of the photoelectron, and with some reasonable assumptions, one can determine the electron dispersion curves $E(k)$ in the solid. Using XPS, one can observe the photoionization of core levels where energies depend on the chemical state of the sample. Therefore, the photoelectron spectroscopy of core levels can often be used for chemical analysis. Whereas using ultra-violet photoemission spectroscopy, one can have an idea about the valence bands electronic structures of the sample. Photoemission spectroscopy measures the density of states (DOS) of the sample under consideration, and thus the photoemission intensity is directly proportional to DOS of the sample. There are several techniques to study the electronic structure of solids, but most of them are indirect and integrated techniques, such as the optical experiments to study the absorption and dielectric constant, or the resistivity measurements. Here the quantum numbers of individual electrons are not sampled. PES can directly measure the DOS, but it is still integrating in angle and therefore information about the

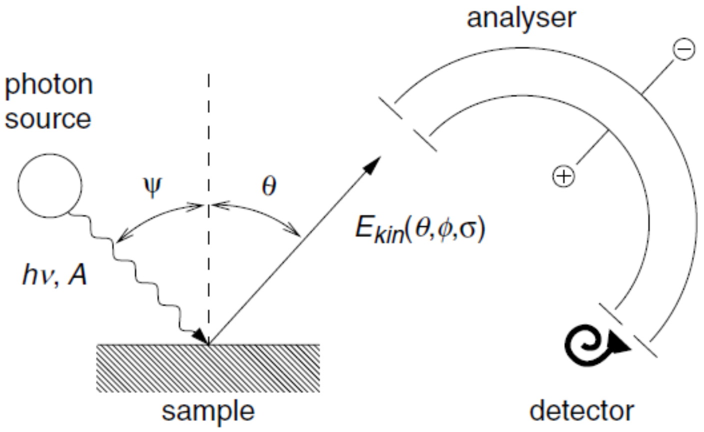

Figure 2.8: Basic principle of a modern photoemission spectrometer. The figure is taken from the Ref. [79].

electron momentum is lost. In order to obtain the full set of electronic quantum numbers (except spin), one has to turn to ARPES (details in next section).

The parameters need to be measured in photoemission are kinetic energy E_{kin} of photoelectron and its angle to the surface normal as shown in Fig. 2.8. Knowing the energy of the photon ($h\nu$) and the work function of the sample surface ($\Phi_\circ$) one can estimate the binding energy E_B of the electron in sample from the following equation

$$E_{kin} = h\nu - \Phi_\circ - E_B. \tag{2.16}$$

Fig. 2.9 shows how energy level diagram and the energy distribution of photo emitted electron relate to each other. The Fermi energy E_F is the top of the valence band and has a separation $\Phi_\circ$ from the vacuum level E_{vac}.

2.6.1 Theory

The interpretation of photoemission spectra in solids using so-called three-step model, developed by Berglund and Spicer [84] is extremely useful. According to this model, photoemission process is broken up into three distinct and independent steps: In

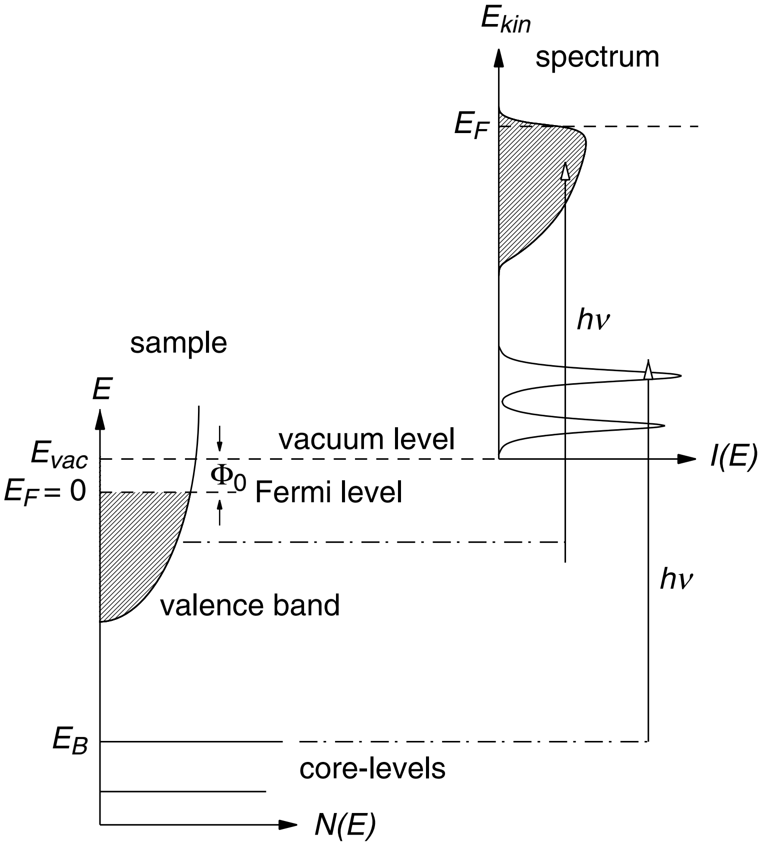

Figure 2.9: Schematic view of the photoemission process in the single particle-picture, depicting relation between energy levels in solid and the electron energy distribution produced by photon of energy $h\nu$ [78, 79].

the initial step photoionization takes place and an electron is excited into a crystal final state. In the second step this excited electron travel through the sample to the surface. Finally, in the third step the photoelectron escapes from the solid into the vacuum where it is detected.

For a given kinetic energy E_{kin}, the momentum parallel to the surface on the crystal $\mathbf{k}_{||}$ is determined by the emission angle of the photoelectron. The geometry of an ARPES experiment is schematically shown in Fig. 2.8. Usually one fixes a surface axis to the emission azimuthal direction obtaining the simplified form of eq. (2.23). Since translation symmetry along the surface is still present in the vacuum-solid interface, parallel momentum conservation of the lattice gives $\mathbf{k}_{||} = \mathbf{k_f}_{||} + \mathbf{g}$. Where

$\mathbf{k_{f||}}$ is the parallel momentum of the final state inside the crystal and $\mathbf{g}$ is a reciprocal surface lattice vector. In addition, since the momentum of the photon is negligible for $h\nu < 10$ keV, translational symmetry in bulk again leads to momentum conservation in the lattice, *i.e.*, $\mathbf{k_f} = \mathbf{k_i} + \mathbf{G}$, $\mathbf{G}$ being a reciprocal bulk lattice vector, and $\mathbf{k_i}$ the initial state momentum. In the reduced zone scheme of the crystal, where all reciprocal lattice vectors are included, this expression simplifies to $\mathbf{k_f} = \mathbf{k_i}$, leading to the following relation:

$$\mathbf{k}_{||} = \mathbf{k_{f||}} + \mathbf{g} = \mathbf{k_{i||}} + \mathbf{g} \tag{2.17}$$

The determination of the momentum component perpendicular to the surface is unfortunately not so direct. The breaking of translational symmetry along this direction leads to a relaxation of $\mathbf{k}_\perp$ conservation, so that $\mathbf{k_{i\perp}}$ cannot be directly obtained. However, knowing the dispersion of the final state bands perpendicular to the surface, the initial state perpendicular momentum $\mathbf{k_{i\perp}}$ can be derived from energy conservation. As a first approach, we can suppose free-electron-like final state bands, shifted from the vacuum reference E_{vac} by the inner potential V_0. Then energy conservation leads to the following expression:

$$k_{f\perp} = \sqrt{\frac{2m}{\hbar^2}(E_{kin} + V_0) - k_{f||}^2} \tag{2.18}$$

Once we know $\mathbf{k_{f\perp}}$, $\mathbf{k_{i\perp}}$ is directly obtained from momentum conservation inside the crystal, *i.e.*, $\mathbf{k_{f\perp}} = \mathbf{k_{i\perp}} + \mathbf{G}$. A more precise derivation of Eq. (2.18) requires a better approximation to the real dispersion relation $E(k_{f\perp})$. For the photon energies used in this thesis, the approximation of free-electron-like final bands is valid except in energy gap regions, where free-electron behavior is no longer the case of final states.

The most general and widely used theoretical description of photoemission spectrum is based on using Fermi's Golden Rule [78] as a result of perturbation theory in first order. In this approach, the photocurrent j is the result of a photon induced excitation of a system from initial state $|i>$ into a final state $|f>$ resulting in a photoelectron with momentum k and kinetic energy E_{kin} and remaining $(N-1)$ electron system:

$$j(E_{kin}, k_{||}, h\nu) \propto \sum T_f |M_{fi}|^2 \delta(E_f - E_i - h\nu)\delta(k_f - k_i) \tag{2.19}$$

where T_f accounts for the transmission probability of the final Bloch state into the vacuum and $|M_{fi}|^2 = |<f|\delta H|i>|^2$ is the transition rate between two states inside the crystal. The δ-Dirac terms account for the energy and momentum conservations.

The perturbation operator δH describes the interaction of a (spin-less) electron in the system with the electromagnetic field **A**. For sufficiently low electromagnetic field the Hamiltonian of the system can be written as,

$$H = H_0 + \delta H = H_0 + \frac{e}{2mc}(\mathbf{A}\cdot\mathbf{p} + \mathbf{p}\cdot\mathbf{A}) \tag{2.20}$$

where $H_0 = (p^2/2m) + V$ is the unperturbed Hamiltonian, $\mathbf{p}$ is the momentum operator $\mathbf{p} = -\mathbf{i}\hbar\nabla$, m and c are mass of electron and speed of light respectively.

For photon energies below 1 keV (standard laboratory photon sources), **A** varies slowly in the mean free path scale of the electron. Further, δH can be approximated as,

$$\delta H \propto \frac{e}{2mc}\mathbf{A}\cdot\mathbf{p} \tag{2.21}$$

using the commutator relation $\mathbf{A}\cdot\mathbf{p} + \mathbf{p}\cdot\mathbf{A} = 2\mathbf{A}\cdot\mathbf{p} - \mathbf{i}\hbar(\nabla\cdot\mathbf{A})$ and the dipole approximation $\nabla\cdot\mathbf{A} = \mathbf{0}$, *i.e.*, **A** is constant over atomic dimensions compared to the wavelength of light used. In the ultra-violet photon energy range **A** can be taken as constant. By using the commutation relation between H_0 and $\mathbf{p}$, we can write the matrix element M_{fi} as $M_{fi} \propto \mathbf{A}\cdot <f|\nabla V|i>$, where V is the crystal potential.

According to this equation the origin of the photoemission intensity is the potential gradient.

2.6.2 Angle Resolved Photoemission Spectroscopy (ARPES)

Angle-Resolved Photoemission Spectroscopy (ARPES) is the simplest and most direct method to investigate the electronic band structure of surfaces and have been quite extensively used in the field of metal, semiconductor and oxide surfaces [75,85]. It has been quite successful in establishing the electronic structure of simple one-dimensional (1D), two-dimensional (2D) systems to more complex three-dimensional (3D) systems. There are many detailed reviews on this field are available in the literature [77, 78]. In the 2D crystalline surface, there is a periodicity in surface along the in-plane (x-y) direction but periodicity breaks along the out-of-plane (z) direction of surface. Apart from energy conservation, the momentum of out-going electrons is also conserved; however, only the parallel component is conserved while the perpendicular component is not conserved due to the translational symmetry breaking along the surface normal. For a given kinetic energy E_{kin} the parallel component of the electron crystal momentum $k_{||}$ is given by,

$$(k_{||x}, k_{||y}) = \sqrt{\frac{2mE_{kin}}{\hbar^2}} \cdot (\sin\theta\cos\phi, \sin\theta\sin\phi) \tag{2.22}$$

where $k_{||}$ is the out-going photoelectron parallel momentum, m is mass of the photoelectron and θ and ϕ are polar and azimuthal emission angles, respectively. The geometry of an ARPES experiment is schematically shown in Fig. 2.8. Usually one fixes a surface axis to the emission azimuthal direction obtaining the simplified form:

$$k_{||} = \sqrt{\frac{2mE_{kin}}{\hbar^2}} \sin\theta. \tag{2.23}$$

From the kinetic energy and angular distribution of the emitted electrons, the energy *vs.* momentum mapping of the crystal (band dispersion) can be determined using the Eqs. 2.16 and 2.23. This technique of “band mapping” is a powerful probe of electronic structure of the crystalline materials. The density functional band structure calculations are also important to investigate electronic structure of solids. The angle-resolved band dispersion measurement can be compared directly with the calculated band structure, which enhances the understanding of the experimentally observed electronic structure of the solids.

2.6.3 X-ray Photoemission Spectroscopy (XPS)

Apart from using photons with energies in the ultraviolet range as described above, it is also possible to perform photoelectron spectroscopy with higher excitation energies in the X-ray regime. The X-ray photon has energy high enough (e.g. 1486.7 eV for Al K_α) to excite electrons from core levels which is usually referred to as XPS or core level photoemission spectroscopy. The simplest application of XPS is the determination of the chemical composition of the investigated sample known as electron spectroscopy for chemical analysis (ESCA), as the binding energies are characteristic for the elements in the periodic table. Still more information can be obtained by taking energy shifts and line shapes into account and analyzing them carefully. The exact peak positions may be capable of indicating the chemical state of the component elements of the sample. Moreover, the change in binding energy between two different chemical state of the same element *i.e.*, *chemical shift* can also provide the chemical state of the element in the compound more precisely. From line shapes it is possible to draw conclusions about detailed electronic structure parameters, interactions and even about valence band properties because valence band electrons are generally involved in relaxation processes that follow the core electron excitation. An asymmetry in core level peak indicates for example the metallic behavior of the respective sample [86]. A detailed description for other many-body effects arise from the participation of more than one electron during the photoemission process can be found in Ref. [87].

2.7 ARPES facility at SINP

In this section, I will describe the ARPES facility [88] that has been established at SINP for detailed surface electronic structure characterization of crystalline materials. This state-of-the-art facility provides high energy and angular resolutions for modern day ARPES measurements and allows different advanced measurements such as band structure mapping, Fermi surface mapping and photoelectron diffraction *etc.*

The ARPES spectrometer was designed at SINP and custom fabricated by PREVAC Sp. z o.o., Poland, integrating different brands of components. The schematic diagram and photograph of the ARPES spectrometer is shown in Fig. 2.10 and 2.11 respectively. The ARPES system consist of three different chambers namely, Load-lock, Preparation and Analysis chambers with easy transfer mechanism of samples between the chambers. The description of each chamber with its components will provide a general idea about the system.

2.7.1 Load lock

The load-lock or fast entry chamber is to put the sample from ambient pressure to high vacuum ($< 5\times10^{-8}$ mbar) where the samples can be left for initial degas. This is facilitated with a halogen lamp which can be used to heat samples up to 200°C. A vacuum suitcase can be readily attached to the load-lock to transfer the sample to other UHV systems.

2.7.2 Preparation chamber

In addition to the standard surface preparation requirements, the preparation chamber is also equipped with several evaporators, Ag^+ ion gun, quartz crystal thickness

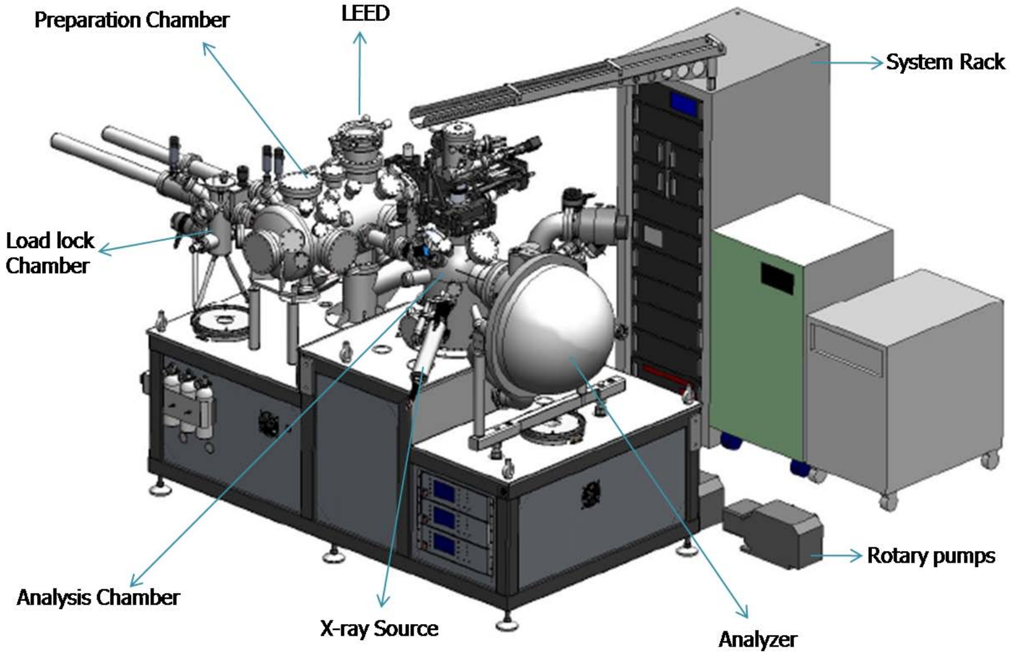

Figure 2.10: The schematic diagram showing different chambers and components of the ARPES system at SINP.

monitor, sample heating arrangement, molecular oxygen supply, to perform growth of metal and metal oxide ultrathin film and multilayers. The base pressure of the preparation chamber is better than 2×10^{-10} mbar which is achieved by 1000 litre/sec Turbo Molecular Pump (TMP) (Leybold Vacuum GmbH) cascaded with another TMP of capacity 70 litre/sec backed by a rotary pump, and is also pumped by an ion pump with a capacity of 300 litre/sec. This chamber consists of a Titanium Sublimation Pump (TSP) and a Getter pump as well. Some of the important components of the preparation chamber are described below.

a. 4-axis Sample Manipulator: For the sample manipulation, the preparation chamber is equipped with a 4-axis (X, Y, Z, polar rotation (θ)) manipulator with heating and liquid nitrogen cooling arrangement. In this manipulator sample can heated up to 1200°C in the continuous mode and 2000°C in the flash mode and cool down the sample up to -170°C using liquid nitrogen. The sample temperature is

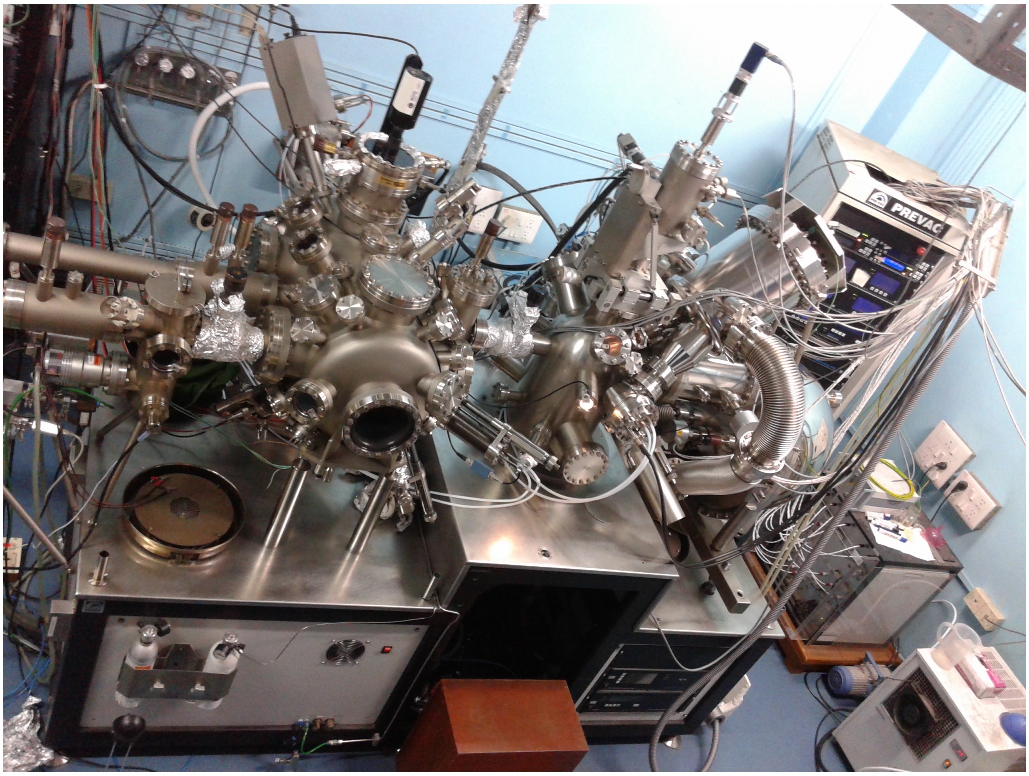

Figure 2.11: SINP-ARPES spectrometer including the monochromatic X-ray source.

measured by K and C type thermocouples depending on the desired temperature range. The motion along Z-axis as well as polar rotation of the manipulator is motorized and controlled by computer to make precise movements for sample transfers and growing films of different thickness on the same substrate at different locations with the help of a mask.

b. Sputtering gun: Ar^+ ion sputter gun is used to clean the top surface of the sample. The energy of Ar^+ ions produced from the sputter gun can be controlled (200-5000 eV) depending on the requirement. Usually after sputtering, one needs to anneal the sample so that the surface atoms can re-order and take their equilibrium positions.

c. UHV cleaver: The preparation chamber is also equipped with a UHV cleaver and can be used to cleave insulating and semiconducting crystals *in situ*. Using the same crystal, multiple cleaves can be made and samples can be heated up to 600°C.

d. Parking chamber: The parking chamber can store up to 6 samples at a time. We can avoid surface contamination of crystals by storing them in-situ and helps to speed up the surface preparation process.

e. Evaporator: For the growth of ultrathin metal films, we use a water-cooled electron-beam evaporator. Here, the metal rod/ingot in crucible is evaporated by electron beam bombardment heating. The flux of the ions ejected from the evaporator is monitored and the rate of evaporation is calibrated. The preparation chamber also equipped with a Knudsen cell that can heat up the evaporating materials to reach higher temperature as 2173 K. It consists of some homemade resistive heating as well as electron-beam evaporators.

f. Quartz microbalance: The rate of evaporation of metals at the sample position can be monitored by the water cooled quartz microbalance. The shift in the resonant frequency of the quartz crystal due to the excess material deposited on the crystal is calibrated to the rate of deposition. The microbalance is mounted on a Z-shift which enables its linear motion. The calibration of the evaporation rate is performed after placing the quartz crystal at the growth position.

g. Low energy electron diffraction (LEED): LEED is the standard technique to study the surface crystalline order. The surface cleanliness, crystal orientation at the surface and crystalline order can be deduced from the LEED pattern in a quantitative way. We have a LEED system from OCI vacuum Microengineering, Inc. Canada with a 12-bit CCD camera for LEED image collection. The details of the LEED has already been discussed earlier in this chapter.

h. Sample holders: Two different types of sample holders are used for all the experiments mentioned in this thesis. The first one, PTS 1000, is capable of resistive heating the sample slowly upto 1000^0C. Here, the Ag(001) single crystal sample is heated by a heating coil mounted at the bottom of the sample holder. The second one, PTS 1200, can heat the sample upto 1200^0C. This sample holder is composed of electron beam heating and therefore can heat up the sample with comparatively faster ramp. The crystal is grounded in both sample holders and the temperature is measured by a K-type thermocouple. Perfect mounting of the single crystal on the sample holder is essential for ARPES measurements. The flatness of the crystal is checked by a laser beam reflection from the sample top surface. The crystalline symmetry direction of the sample is determined by LEED measurements.

2.7.3 Analysis chamber

The analysis chamber is dedicated for performing the photoemission experiments. The base pressure of this chamber is better than 8×10^{-11} mbar which is achieved by a 600 litre/sec TMP cascaded with 70 litre/sec TMP and a rotary pump. The chamber is also pumped by a titanium sublimation pump (TSP) integrated with a liquid nitrogen cryo shroud. As the ARPES measurements are very sensitive to the stray magnetic field around the sample region, the analysis chamber is made out of mu-metal so that on the sample region we have less than 0.5 micro Tesla field. The analysis chamber is equipped with the following components.

a. 5-axis Sample Manipulator: For the sample movement in analysis chamber, we have another 5-axis manipulator (X,Y,Z translation and θ, ϕ rotation) with heating and cooling facilities as described before. The polar θ as well as azimuthal ϕ rotation of the manipulator is computer controlled so that ARPES spectra can be collected at different polar and azimuthal angles in an automated way.

b. Monochromatic X-ray source: The analysis chamber is equipped with a single-anode monochromatic x-ray source (Model: MX 650, from VG-Scienta) for performing XPS and Photoelectron Diffraction measurements. The Scienta MX 650 X-ray source produces high intensity monochromatic Al K_α radiation. It contains an aluminium anode and a quartz crystal monochromator. It yields an excitation energy of 1486.6 eV in a narrow band of 0.4 eV.

c. Monochromatized High Intensity UV lamp: For the high-resolution ARPES measurements, it is required to have a high intensity UV lamp which is monochromatized to remove the higher order satellites of the radiations. In the analysis chamber, we are equipped with such a high-intensity lamp (VG Scienta VUV5000) which is a microwave driven Electron Cyclotron Resonance (ECR) based He lamp and is coupled with VUV5040 monochromator. The exit stage of the monochromator can house different diameter capillaries to have a reduced spot size on the sample as the angular resolution of the ARPES critically depends on the photon beam spot size. This capillary also restricts the flow of the Helium into the experimental chamber and thus maintaining a good vacuum during experiments. We use a capillary of inner diameter 0.8 mm and obtain a spot size of $\sim$1.2 mm of the photon beam at the sample position. Moreover, it helps to maintain the chamber pressure to the base pressure even during the ARPES experiments. For the ease of operation, the whole UV lamp is mounted on a special manipulator so that the lamp can be inserted very close to the sample (about 10 mm) and can be retracted after the experiments. The UV lamp primarily gives He I_α (21.22 eV) and He II_α (40.81 eV) with energy resolution better than 1 meV. The whole assembly is pumped by various pumping stages to reduce the flow of helium into the analysis chamber.

d. Hemispherical Electron Analyzer: The heart of the ARPES experiment is to measure the kinetic energy of the outgoing electrons at different emission angles. In the analysis chamber, we have a 200 mm concentric hemispherical analyzer (VG Scienta R 4000-WAL) with wide-angle lens for high-resolution and fast ARPES measurements. This is the state-of-the-art 2D analyzer with Multi-channel Plate (MCP)-CCD detector which can map the emission angle of the electrons with their kinetic energy and obtain a direct dispersion images on the screen. The widest angular range possible is $\pm 15^\circ$ with an angular resolution $\sim 1^\circ$. There are other angular ranges $\pm 7^\circ$ and $\pm 3^\circ$ with angular resolutions $\sim 0.4^\circ$ and $\sim 0.1^\circ$, respectively. The energy and angular resolution have been tested at the laboratory with values

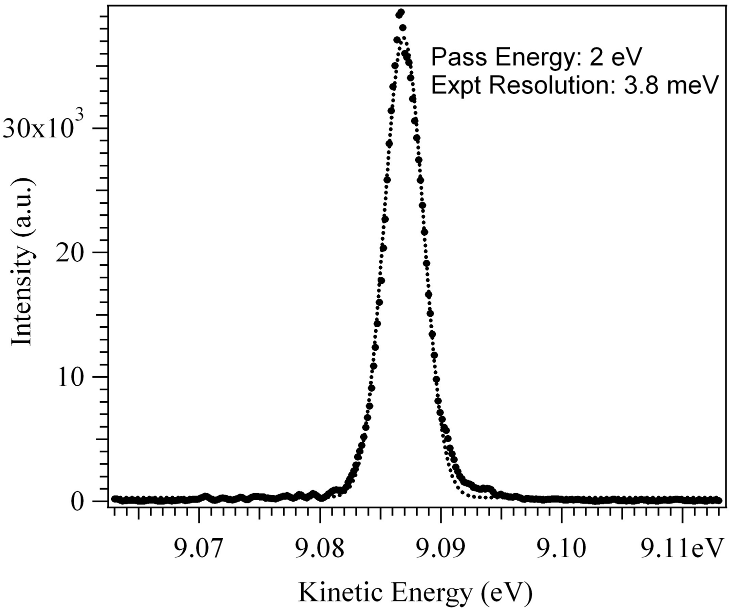

Figure 2.12: Experimental energy resolution measurement on Xe $5p_{3/2}$ [61].

matching near the specified values. The angular dispersions of the analyzer have been tested with a special angular device mounted on the sample manipulator. The gas cell measurements on the 5 $p_{3/2}$ core level of Xenon (at binding energy ∼12.1 eV), gives the energy resolution matching to the expected performance of the analyzer as shown in Fig. 2.12. However, the experimental energy resolution on solid samples depends on the sample temperature.

2.7.4 Electron Energy Analyzer

In photoemission process, the most important part is measuring kinetic energy of the photoelectrons. The photoelectrons drifting in the vacuum are pulled toward and focused into the energy analyzer by an electric field created by an electrostatic lens. Though energy analyzers come in different configurations, the most common type is the Concentric Hemispherical Analyzer (CHA) [89]. A CHA consists of two hemispheres of radius R_1 and R_2 [Fig. 2.13] of slightly different sizes having the same center point. A voltage is placed across the two hemispheres such that the inner one is positively charged relative to the outer one, hence creating a radial electric field. The electrostatic lens directs the photoelectrons into the space between the two hemispheres. Subsequently, all the photoelectrons will experience a centripetal force and hence undergo uniform circular motion. Thus, the radius of curvature of this motion for a given potential difference between the two hemispheres is determined by the electron's kinetic energy. The kinetic energy of the electron traveling on the central path $R_0 = (R_1 + R_2)/2$ is given by

$$E_p = \frac{eV}{R_2/R_1 - R_1/R_2} \tag{2.24}$$

This energy is called the pass energy of the analyzer, and it is determined by the radii of the hemispheres and the voltage applied between them. Photoelectrons that have a kinetic energy greater than the pass energy will have a larger radius of curvature and will therefore collide with the outer hemisphere. Whereas photoelectrons that possess a kinetic energy less than the pass energy will have a smaller radius of curvature and will coincidentally collide with the inner hemisphere. Note that the pass energy actually has a small range of energies associated with it, since the space between the hemispheres is not infinitesimally small. When a photoelectron survives to come out the other side of the space between the hemispheres, it strikes an electron multiplier in order to increase the signal to a more discernible amount. Electron multipliers consist of material with electrons in a low binding energy state such that the energy of the photoelectron is capable of dislodging multiple electrons from their atoms, which in turn will dislodge even more electrons. This cascade effect increases the number of electrons striking the detector, thus improving the signal since the current contribution of a single electron would be difficult to detect. Note that the kinetic energy of these detected electrons is not important since the kinetic energy of the electron that started the cascade has already been determined.

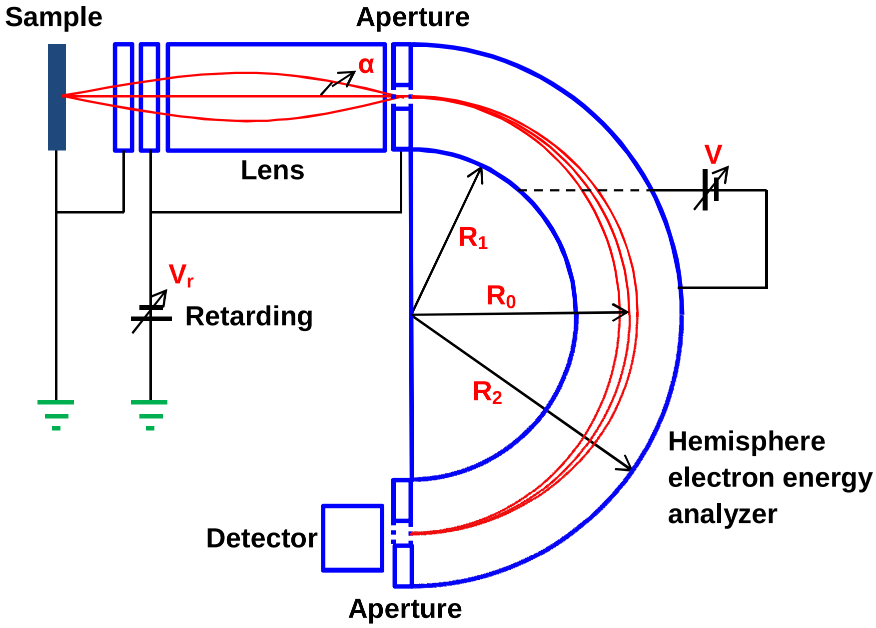

Figure 2.13: Schematic of a concentric hemispherical electron energy analyzer. Taken from Ref. [90].

The energy resolution of a CHA is calculated as [91]

$$\Delta E = E_p(\frac{x_1 + x_2}{2R_0} + \alpha^2) \tag{2.25}$$

where x_1 and x_2 are width of the entrance and exit apertures, α is the angular acceptance of the electron beam at the entrance slit. From the above relation, it is evident that the radii of the hemisphere and the slit width are relevant in determining the resolution of an energy analyzer. Hence, a large hemisphere is inherently favored because of a better resolution. In reality, the pass energy and the aperture sizes are set to achieve a good compromise between signal intensity and energy resolution.

2.8 Modes of photoemission data collection

Photoemission experiments can be performed in different modes. The most common mode is called Energy Distribution Curve (EDC) and consists on measuring the kinetic energy of the photoelectrons for fixed photon energy, as can be seen in Fig. 2.14(a). Since the total energy must be conserved, different kinetic energy implies different initial energy. A typical EDC spectrum is shown in bottom of Fig. 2.14(a). The peaks correspond to elastically scattered photoelectrons, while the inelastic electrons spread in a smooth background. The cut-off at high kinetic energies indicates the Fermi level. In general, EDC curves are used to investigate the dispersion of the initial states, as well as the lifetime of the initial hole and the final electron. By taking EDC curves for different emission angles at the same photon energy we are selecting different parallel momenta and therefore the dispersion of

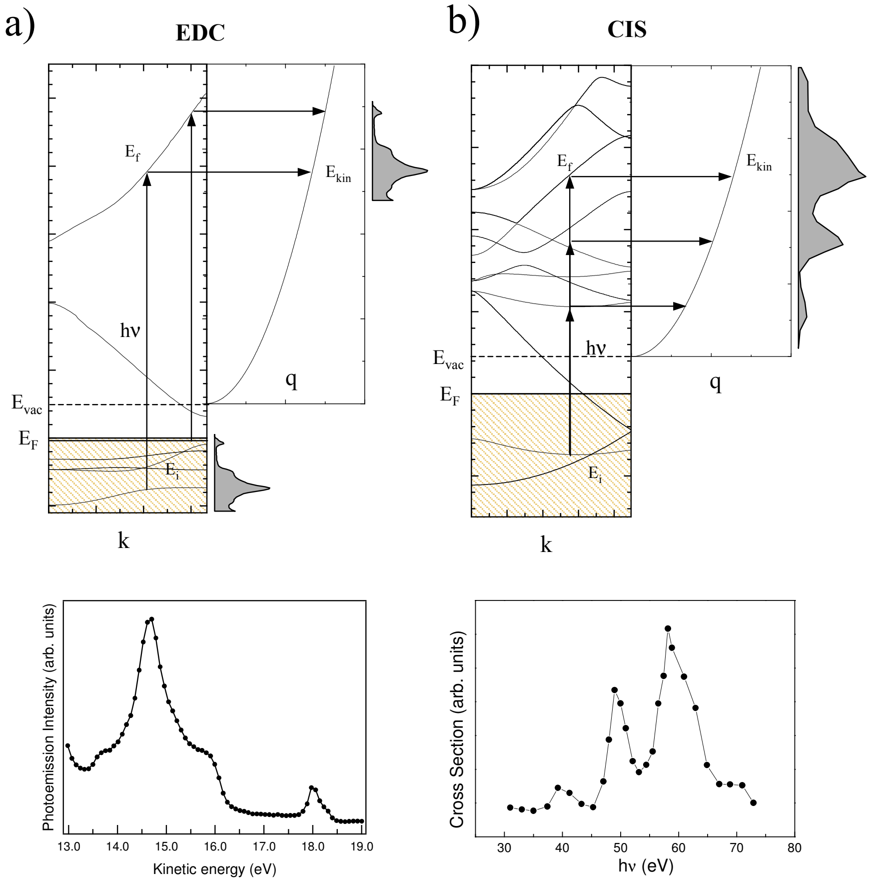

Figure 2.14: Schematic representation of energy balance (top) and typical spectra (bottom) for a) an EDC experiment and b) a CIS experiment [92].

the initial states parallel to the surface can be mapped. This is what is usually done in a laboratory.

Another type of experimental mode is the Constant Initial State (CIS). Here one can fix the initial energy by simultaneously varying both the photon and the measuring kinetic energy, as can be seen in Fig. 2.14(b). Thereby measuring the initial state photoemission cross-section as a function of photon energy. In the CIS spectra shown below, we see that the photoemission cross-section of the initial state oscillates as we vary the photon energy. We can obtain information about the spectral function of the initial and final momentum perpendicular to the surface from CIS experiments. In this thesis all the photoemission data were collected in EDC mode, hence CIS mode is beyond the scope of this thesis.

2.9 Instrument development in the laboratory

A substantial part of the Ph.D. tenure was spent in developing different homemade instruments not only to do cost-effective research but also to achieve better experimental condition like attaining lower base pressure in the UHV chambers by incorporation of homemade getter pumps. Some of the UHV grown thin films that will be presented in the thesis were grown by homemade evaporators. In the following sub-sections, I will discuss the details of the homemade evaporators and getter pumps.

2.9.1 Evaporators

Commercial effusion cell is readily available in the market for thin films deposition. However, commercial effusion cell can be costly at times. So, our motivation was to build cost-effective evaporators also to save time in procuring the evaporators from the company. The basic design of the resistive-type evaporators is shown in the Fig. 2.15 (left) along the actual photograph of the evaporator (right). Two tungsten

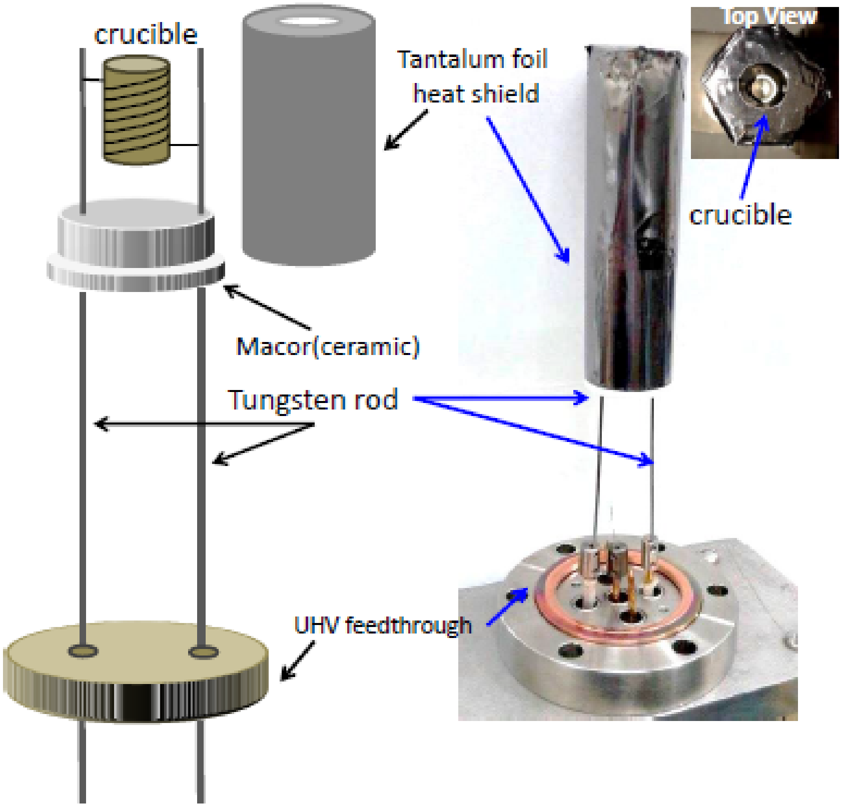

Figure 2.15: Schematic representation of a homemade resistive-type evaporator showing different components (left) and the real photograph of the evaporator (right) with heat shield shown from top (inset).

rods were connected to two opposite feedthrough connector using molybdenum barrel connectors, which was made in our workshop using molybdenum rods. A high purity alumina crucible from Alfa Aesar (Al-23), was used to evaporate the material. However, the choice of crucible is crucial and depends on the material to be deposited. The exact crucible can be chosen from the evaporation table [93]. It was confirmed form the table that Al_2O_3 crucibles can be used for resistive evaporation of magnesium (Mg), the evaporating material in our case. Next, tungsten wire used as filament was wound around the crucible. The diameter of the filament can be of different value. To reach a particular a temperature one needs to send larger current in thicker filament compared to thin one. However, for the mechanical stability of the assembly, an optimum thick tungsten wire is necessary as otherwise the crucible would sag under its own weight when heated to higher temperature. As the temperature required for evaporation of Mg (T= 247°C) was lower, we did not use any extra support to hold the crucible and was hung by the filaments themselves. For Mg, 10^{-6} mbar vapour pressure can be reached at T= 247°C [93]. For that reason we have used a moderate diameter (0.375 mm) tungsten wire as filament. The two ends of the filament is spot welded to the two tungsten rods. The tungsten rods were initially cut to have desired length. A disc made of macor, a machinable ceramic was connected in between the crucible and feedthrough as a housing to the heat shield and also to reduce heat flow to the body of the chamber. A cylindrical heat shield, made of thin tantalum foil (thickness 0.25 mm) was made to reduce the heat flow in the chamber and to attain a good base pressure during evaporation. The reason behind choosing tantalum is that Ta is refractory and gets degassed thoroughly by the heating. So, after proper degassing, the base pressure is very low as well as it contains the heat. The flow of the evaporating material is collimated by means of a hole on top side of heat shield as shown in Fig. 2.15. Once we were finished with the fabrication of the effusion cell we put it in a testing chamber for setting up the evaporator for regular use. The alumina crucible used was first cleaned chemically by ultrasonication. Initially, the crucible was kept empty inside the testing chamber during initial degassing. The idea was to degas the crucible to remove any unwanted or adsorbed material in it. The current in the filament was increased slowly in step to have a well-formed filament. When the filament became red hot after 2-3 cycles of degassing, we increased the current further till the filament became white hot to degas the crucible as well as the tantalum shield. The number of degassing cycles, however, can be increased depending on the base pressure. We have reached as low as 2×10^{-10} mbar base pressure. After that, the evaporator was taken out to put the evaporating material into the crucible. Mg chips (99.98%) from Sigma Aldrich was used as evaporating material in the evaporator. The evaporation rate was calibrated using water-cooled quartz microbalance, and a constant evaporation rate at a low base pressure was observed over a long deposition time. After this, the evaporator was taken out and was installed in the preparation chamber of the ARPES system for the deposition experiments.

2.9.2 Getter pumps

The use of getter material to achieve better UHV condition is well known [94, 95]. Getter provides a pumping action utilizing a chemical reaction where a chemically active gas reacts with chemically active metal to form a low vapour pressure material. Hydrogen (H_2) is the only gas, other than inert gas for obvious reason, which does not react with the getter material instead dissolve into the getter material to form a solid solution. Getters can be classified into two separate categories: evaporable and non-evaporable. Evaporable getters were used in our system. Getter materials are evaporated on an internal array or a portion of the inner surface of the chamber. There it forms a thin film which acts as a pump for active gases and H_2. The pumping speed is directly proportional to the total exposed surface area of the condensed film. The pumping speed of a freshly deposited film will decrease as it reacts (pumps) the gas in the vacuum chamber, and the lifetime of the film depends upon the gas load it is required to pump. Therefore, getter films need to be formed at a regular interval. In case of our UHV system, it was observed that using turbo-molecular pump backed by rotary pump also with a titanium sublimation pump (without liquid nitrogen cooling) was able to reach a pressure 2×10^{-10} mbar. At this low pressure, the major part of the residual gas is H_2 as observed by the Residual Gas Analyser (RGA). So the aim was to reduce the partial pressure of H_2 by using suitable getter material. It is well-known that rare earth material absorbs H_2 gas [96]. So we have chosen Cerium (Ce) as an evaporable getter material. To evaporate Cerium, we have to reach a

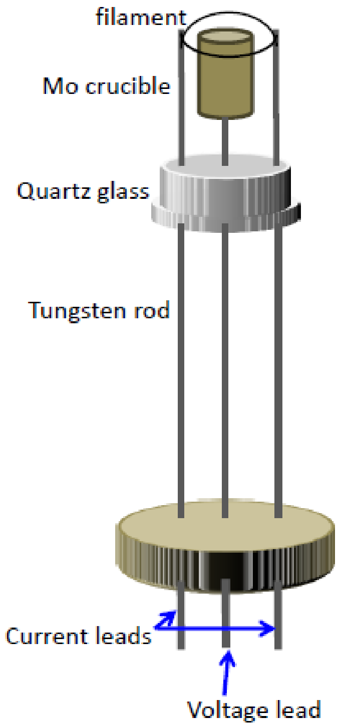

Figure 2.16: Schematic representation of homemade electron-beam type evaporator used for Cerium evaporation.

temperature of 1000 ° C [93]. Though the said temperature can be reached using resistive type evaporator using alumina crucible, we found that alumina got cracked and eventually broke if used continuously at high temperature for Cerium evaporation. So, electron-beam type evaporation was preferred. This Cerium evaporator for the Getter pump was also made in our laboratory. The same type of UHV feedthrough was used to connect two tungsten rods of suitable length. Thin tungsten wire (0.1 mm) was used as filament and connected to the two tungsten rods forming a circle keeping the crucible at the center [see Fig. 2.16]. Molybdenum crucible was machined out from a Mo rod and used in the electron-beam evaporator. The crucible was connected through a tungsten wire to a pin in the feedthrough to keep the crucible at a higher voltage compared to the filament. Now, keeping the crucible at 700-1000 Volt if we pass current through the filament, due to thermionic emission, electrons will be ejected from the filament and strike the crucible to heat. As a result, Cerium will be evaporated. Unlike Macor in resistive case, we had used quartz glass in the form of a disc to reduce heat flow towards flange. There was no heat shield like in the case of resistive evaporator. Instead of the heat shield, an umbrella of stainless steel was used over the evaporator so that the evaporated material evaporates on the umbrella surface and does not get deposited on the main chamber at all. As mentioned earlier, the pumping speed of this type of system is directly proportional to surface area. To enhanced the effective surface area of the evaporated Cerium, many strips of thin stainless steel plates were spot welded inside the umbrella surface. The total system along with the umbrella was put into very small and compact UHV chamber and finally connected to the main UHV chamber so that even accidentally there would be no deposition of Cerium onto the system. Before putting it into the main chamber, the evaporator and the shield were well-degassed in another testing UHV chamber. The pressure of the main chamber was found to reduce to 5×10^{-11} mbar from 2×10^{-10} mbar up on Cerium activation with substantial reduction in the hydrogen partial pressure as could be seen from RGA. The advantage of this pump over the titanium getter pump is that the pumping volume, in this case, is much larger than that of Ti getter pumps since the gases may diffuse easier in the bulk of rare earth metals, and also the pumping surfaces do not have to be cooled with liquid nitrogen.

2.10 Summary

This chapter provides a brief introduction to different experimental techniques used in this thesis. Different aspects of epitaxial film growth on a substrate has been illustrated. LEED technique has been used extensively to study the surface crystalline structure and antiferromagnetism of the grown films. To probe the valence band electronic structure of the crystalline thin films, ARPES has been satisfactorily used. On the other hand, XPS probes the core levels of the elemental components. Development of different homemade instruments in the laboratory during the Ph.D. tenure has also been mentioned here.

3

Growth and characterization of CoO thin film on Ag(001) and Ag(111)

3.1 Introduction

Late transition metal monoxides are promising systems for potential applications in the field of lasers, sensors and catalysts [97–99]. However for use in these applications, one requires a detailed understanding of their optimum growth conditions and the dependence of structural and electronic properties on these growth parameters. Moreover, from a basic science point of view, the exact description of the electronic structure of ultrathin monoxides like NiO, CoO *etc.* is still a matter of interest due to their strong electron-electron correlations. Electronic structure of CoO single crystals was studied by several groups [56, 100–103] though studies using various surface sensitive techniques such as LEED, photoemission *etc.* has been hindered due to the charging effects from the insulating CoO surface. However, now it is well known that growth of high quality insulating ultrathin films on metallic substrates can reduce the charging effects due to their proximity to the metallic substrates. So far, most of the studies related to the electronic structure of CoO systems were

---

Part of the work presented in this chapter has been published in Journal of Crystal Growth, ***487****, 28-33 (2018).*

focussed either on the bulk crystals or on thick films. Though there are studies available on the electronic structure of CoO thin films [1–3], however, detailed growth optimization and the effect of growth parameters on the surface electronic structures have not been addressed so far in the literature. Moreover, a closer inspection near Fermi edge reveals the appearance of interfacial states in the lower coverage of CoO film which has been already known for prototype systems like NiO/Ag(001) [3–5] and MnO/Ag(001) [6]. The interfacial state induced metallic character in the low film coverage disappears in the bulk CoO. The insulating nature of bulk CoO is related to the antiferromagnetic ground state, the metallic behavior in the low coverages may influence the magnetic properties of the film. The present study involves understanding the growth mechanism of CoO films on Ag(001) substrate and related electronic structure in the ultrathin regime. In order to grow a stoichiometric and well-ordered film, control over the growth parameters is essential because non-equilibrium growth conditions can lead to different growth modes and film structures. There are several methods of oxide growth available on metallic single crystal substrates, however, the evaporation of Co metal in the oxygen atmosphere is preferred rather than oxidation of Co film for the layer-by-layer growth [1, 2, 104, 105]. The growth at elevated substrate temperature can be more effective to get a well-ordered stoichiometric film than the two-step growth process, *i.e.*, growth at RT followed by subsequent annealing at a higher temperature. It is evident that two-step growth in the low coverage regime forms precursor state which transforms into a well-ordered (2×1) double layer CoO(001) islands upon post-growth annealing at higher temperature [106, 107]. In the last two decades, CoO growth on different metallic substrates was explored using Scanning Tunneling Microscopy (STM) and photoemission spectroscopic techniques [106–111]. Sebastian *et al.* [107] reported that initial stages of CoO growth drastically depends on the preparation conditions. The growth of well-ordered islands of monolayer CoO(001), CoO(111), and double layer CoO(111) islands on Ag(001) has been studied by STM [105,106]. So, the growth of these transition metal oxides is still a matter of interest, especially in the ultrathin regime.

3.2 Experimental details

All the experiments were performed in a standard UHV setup having base pressure better than 1×10^{-10} mbar. Well-polished Ag(001) substrate was prepared by repeated cycles of Ar^+ ion sputtering (600 eV, 1 μA, 1×10^{-6} mbar) and annealing at 823 K until a well-ordered $p(1 \times 1)$ LEED pattern was observed. High purity cobalt (99.995%) was evaporated from an alumina crucible within a well-degassed effusion cell at a constant rate of 0.4 Å/min, in the oxygen atmosphere. Initially, the oxygen background pressure was kept fixed at 1×10^{-6} mbar and 5 ML CoO films were grown at two different substrate temperatures, namely, room temperature (RT i.e., $\sim$ 300 K) and 473 K. Afterwards, keeping the substrate temperature fixed at 473 K, the oxygen background pressure was changed to 1×10^{-7} mbar. During growth, oxygen was introduced via a capillary tube guided close to the sample surface, resulting in a higher local pressure, without much affecting the base pressure of the chamber. The sample temperature was measured using a K-type thermocouple, in contact with the Ag(001) crystal. The deposition rate was calibrated using a water-cooled quartz crystal thickness monitor, mounted on a linear drive which could move to the sample position to measure the growth rate. The monolayer (ML) of CoO is defined as the atomic density corresponding to 1 ML cobalt on Ag(001), *i.e.*, 9.03×10^{18} atoms/m^2, under the oxygen atmosphere. The surface crystalline quality and the symmetry directions of the surface Brillouin zone (SBZ) were determined using a four-grid LEED apparatus (OCI Vacuum Microengineering) attached to the preparation chamber. A highly sensitive 12-bit Peltier cooled CCD camera was used to collect all the LEED images at RT. ARPES measurements were performed using a combination VG SCIENTA-R4000WAL electron energy analyzer with a 2D-CCD detector and a high flux GAMMADATA VUV He lamp attached to a VUV monochromator, which has been described in detail elsewhere [88]. He I_α(21.2 eV) and He II_α(40.8 eV) resonance lines have been used to excite the photoelectrons from the sample for ARPES measurements while monochromatic Al K_α X-ray source (1486.6 eV) from VG SCIENTA has been used for core level XPS measurements. The Fermi energy (E_F) position and the total experimental energy resolution has been estimated using clean polycrystalline bulk Ag sample as reported earlier [112]. All the XPS and ARPES measurements were performed at RT with total experimental energy resolutions better than 0.6 eV and 0.1 eV respectively, including the thermal broadening near the Fermi energy.

3.3 Experimental results on CoO/Ag(001) and discussion

3.3.1 LEED study at different growth conditions and film coverages

As mentioned earlier, 5 ML CoO was grown under different growth conditions and the surface crystallinity was investigated by LEED in order to obtain the optimum growth condition. For the RT growth (G1), a faint (2×1) twin-domain pattern appears due to the under stoichiometric phase [see Fig. 3.1(a)]. Similar LEED pattern was observed in the early stage of NiO and CoO films growth [107, 113–115] though they are bit different in nature. In the 1-2 ML coverage, NiO and CoO form precursor states at RT growth which give rise to a (2×1) LEED and disappears with increasing coverage or annealing at the higher temperature. In contrast, we have observed this at 5 ML coverage which was not completely removable by post-growth oxygen annealing at 473 K (A1) [see Fig. 3.1(d)]. The growth at the elevated substrate temperature (G3) shows a faint eight-fold mosaic structure surrounding each integer spot of the (1×1) pattern as shown in Fig. 3.1(c). However, the oxygen-deficient elevated temperature growth (G2) shows mosaic-free sharp LEED pattern [see Fig. 3.1(b)].

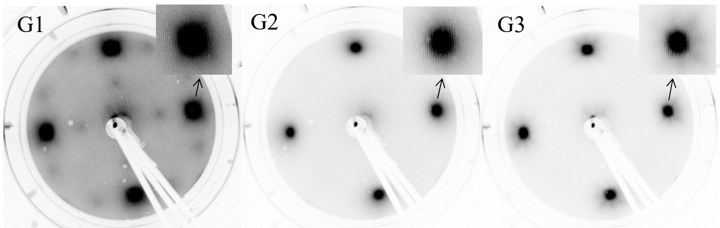

(a) RT, 1×10^{-6} mbar (b) 473 K, 1×10^{-7} mbar (c) 473 K, 1×10^{-6} mbar

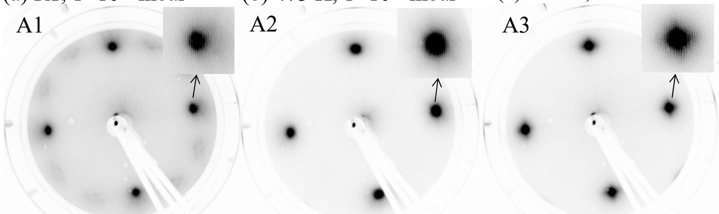

(d) 473 K, 1×10^{-6} mbar (e) 573 K, 1×10^{-6} mbar (f) 673 K, 1×10^{-6} mbar

Figure 3.1: LEED images of 5 ML CoO collected at RT with 55 eV beam energy for different growth conditions. Fig. 1(a)-(c), shows the LEED pattern at three different growth conditions labeled as G1, G2, and G3. Fig. 1(d)-(f) shows the LEED image of the corresponding post-growth annealing at different conditions labeled as A1, A2, and A3, respectively. Inset of each figure shows the zoomed-in view of the (1,0) integer-order spot.

Upon post-growth oxygen annealing at the higher temperature (A2) a very faint mosaic structure starts appearing as shown in the inset of Fig. 3.1(e). Post-growth oxygen annealing at even higher temperature (A3) of the film grown at 473 K (G3), the eight-fold mosaic structure transforms into a four-fold mosaic structure as shown in Fig. 3.1(f). The coverage dependent LEED study also reveals the evolution of mosaic structure with film coverage. Fig. 3.2(a)-(d) shows the LEED images of different film coverages grown at 473 K (G3). In the lower coverage region (2 ML), mosaic-free and high-intensity sharp spots were observed [see Fig. 3.2(a)]. As the film coverage increases, the eight-fold mosaic structure starts appearing at 5 ML [see Fig. 3.2(b)] which transforms into a four-fold mosaic structure at 10 ML [see Fig. 3.2(c)] and finally disappears at 20 ML film coverage as shown in the inset of Fig. 3.2(d). Evolution of in-plane lattice parameter [see Fig. 3.2(e)] shows that the CoO film growth starts with the same in-plane Ag(001) lattice parameter up to 2 ML despite ∼4% lattice mismatch between Ag(001)[4.09 Å] and bulk CoO [4.26 Å]. With further

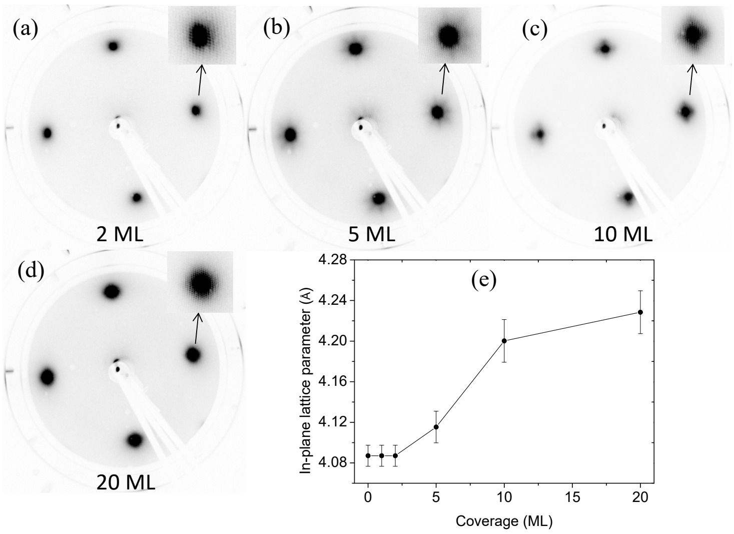

Figure 3.2: (a)-(d) LEED pattern of different CoO film coverages grown at 473 K and 1×10^{-6} mbar oxygen background pressure (G3). All the images were taken at 55 eV incident beam energy where the mosaic intensities were maximum. The zoomed-in view of the (10) LEED spot has been shown for better clarity of the mosaic structure around each spot. (e) Evolution of in-plane lattice parameter as a function of CoO film coverage.

increase in film coverage, in-plane lattice parameter increases steadily and reaches to an almost saturated value 4.22 Å at 20 ML. Complete strain relaxation is expected at even higher film coverages to reach the bulk CoO lattice parameter. After the initial few layers of pseudomorphic growth, the film gradually relaxes by virtue of misfit dislocation at the buried interface which exhibits the mosaic structure in LEED pattern. The misfit dislocations created by interfacial lattice strain between the substrate and the film causes these types of mosaic structure as explained by several groups [116, 117]. We have also observed very faint eight-fold mosaic pattern which transforms into a four-fold mosaic structure upon annealing to a higher temperature or increase in film coverage. Our optimized LEED setup with the high-resolution CCD camera enables us to observe such faint structures in the LEED pattern. In extension to the available explanation of the four-fold mosaic formation, one can predict the eight-fold mosaic formation in a similar fashion. If the mosaic grains form glide planes at an angle 45° to each other in the real lattice, the diffraction pattern in the reciprocal lattice should be eight-fold instead of being four-fold. Upon annealing at a higher temperature, these glide planes reorient themselves in one direction due to the available thermal energy which transforms the eight-fold mosaic into a four-fold mosaic structure. With increasing film coverage, the unidirectional strain relaxation can also lead to the eight-fold mosaic into a four-fold mosaic structure [118]. However, in order to investigate the exact mechanism of this transformation we have to use more direct microscopic techniques like STM.

3.3.2 Core level electronic structure

Fig. 3.3(a)-(b) shows the Co 2*p* and O 1*s* core level spectra of 5 ML CoO for different growth conditions. The RT growth (G1) shows a non-stoichiometric phase of CoO as the Co 2*p* peaks are shifted towards lower binding energy positions. [see Fig. 3.3(a)]. Unlike the stoichiometric CoO, which has only Co^{2+}, this non-stoichiometric phase consists of both Co^{2+} and Co^{3+} cations. The core emission at 779.6 eV primarily corresponds to Co^{3+} which is in line with the spinel Co_3O_4 structure [119], however, the emission at 780.3 eV corresponding to Co^{2+} is shifted from Co^{2+} position (780.5 eV) of spinel Co_3O_4 by $\sim$ 0.2 eV lower binding energy indicates a non-stoichiometric Co_3O_4 growth as well. Moreover, the CoO characteristic shake-up satellites are less prominent for RT (G1) relative to the elevated temperature growths (G2, G3) as reported earlier [119]. This non-stoichiometric phase growth is quite expected due to high sticking coefficient of oxygen at RT. The post-growth oxygen annealing at 473 K (A1) of the RT-grown film (G1) for 20 min was ineffective to grow stoichiometric CoO as there was no significant Co 2*p* peak shift upon annealing [see Fig. 3.3(a)]. The oxygen-deficient growth (G2) shows the weak metallic Co $2p_{3/2}$ and Co $2p_{1/2}$ peaks at 778.3 eV and 793.4 eV, respectively which disappear upon post-growth oxygen annealing (A2) for 20 min. However, the O 1*s* peak is shifted towards lower binding energy which is not desired for stoichiometric growth. For the growth G3,

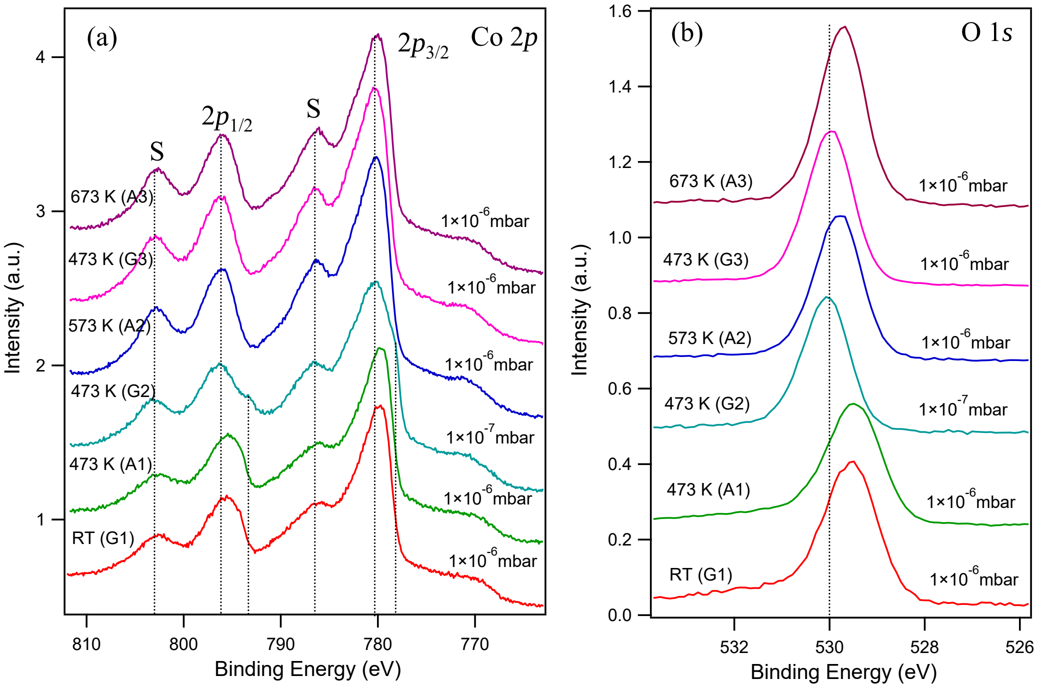

Figure 3.3: (a)-(b) Co $2p$ and O $1s$ core level spectra of 5 ML CoO for different growth and post-growth annealing conditions. Three different set of growth and their corresponding annealing spectra are labeled as G1, G2, G3 and A1, A2, A3, respectively.

Co $2p_{3/2,1/2}$ peaks were observed at 780.5 eV and 796.3 eV, respectively, with their corresponding shake-up satellites about 6.2 eV higher binding energy from the main peaks. The O $1s$ peak was observed at 530 eV for elevated temperature growths (G2, G3) as shown in Fig. 3.3(b). These spectral positions of the film grown at G3 are good in agreement with the earlier reported single crystal data [56, 120]. Post-growth oxygen annealing at 673 K (A3) causes no significant change in Co $2p$ peak position, however, the O $1s$ peak is shifted towards lower binding energy due to the lower oxygen sticking coefficient at elevated temperature. All the Co $2p$ and O $1s$ peak positions for different growth and annealing conditions are shown in Table 3.1. Despite a well-ordered mosaic-free (1×1) LEED at the oxygen-deficient growth (G2), the presence of the metallic character in the XPS spectra suggested using higher oxygen pressure for subsequent growths. XPS results indicate a stoichiometric CoO

Table 3.1: The core level binding energy positions of 5 ML CoO film for different substrate temperature and oxygen partial pressure growth. All the values are in eV.

Core lines	G1	A1	G2	A2	G3	A3	Ref. [56]	Ref. [121]
Co $2p_{3/2}$	779.9	779.9	780.3	780.3	780.5	780.4	780	780.4
Co $2p_{1/2}$	795.5	795.4	796.2	796.2	796.3	796.1	-	796.2
Co $2p_{3/2}$ sat	785.8	786	786.4	786.4	786.6	786.3	786	786.7
Co $2p_{1/2}$ sat	802.6	802.7	802.9	802.8	802.8	802.8	-	802.5
O $1s$	529.5	529.5	530	529.8	530	529.7	528.5	529.4

growth at the elevated substrate temperature ($\sim$ 473 K) with a minimum 1×10^{-6} mbar oxygen background pressure (G3).

3.3.3 Evolution of valence electronic structure with growth conditions and film coverages

Fig. 3.4 shows the ARPES spectra at $\overline{\Gamma}$ symmetry point of CoO(001) surface Brillouin zone (SBZ) for the films grown at different growth conditions using monochromatized He II$_\alpha$ photons within the binding energy (BE) range of 0-10 eV. All the energy distribution curves (EDC) are taken with angular averaging over $\pm2^\circ$ around the $\overline{\Gamma}$ point. The distinct feature 'A' appears at the top of the valence band [see Fig. 3.4] of non-stoichiometric CoO phase grown at RT mainly due to the presence of Co^{3+} as observed in XPS. It is reported that the top of the valence band of Co$_3$O$_4$ results from the 3d$^6\underline{\text{L}}$ final state of the octahedral Co^{3+} $3d$ band which exhibits as a sharp valence band peak at 1 eV below the Fermi level [119]. The feature 'A' also appears at 1 eV with an extended band edge approaching Fermi level which confirms the presence of Co^{3+} in the non-stoichiometric phase grown at RT. Post-growth annealing (A1) does not change the feature 'A' significantly which is consistent with our XPS measurement as well [see Fig. 3.3(a)]. For the oxygen-deficient growth (G2), a feature 'A$'$' similar to 'A' is observed in the vicinity of the Fermi level [Fig. 3.4]. This could be due to the presence of metallic Co or oxygen defects in the CoO films

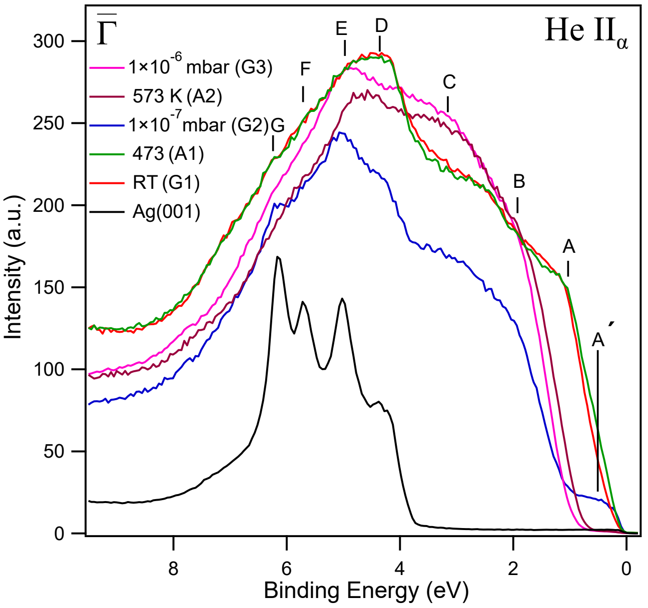

Figure 3.4: ARPES spectra of 5 ML CoO at $\overline{\Gamma}$ point using He II$_\alpha$ photon at different growth conditions. Angle-resolved EDC of clean Ag(001) is also shown as a reference spectra.

which in both cases indicate incomplete oxidation of Co due to insufficient oxygen partial pressure. Upon post-growth oxygen annealing at 573 K (A2) for 20 min, the feature ‘A′’ diminishes and the spectral feature matches well with the elevated temperature growth. The origin of the feature‘A′’ appears at 0.5 eV binding energy most likely to be metallic Co present in the sample as confirmed by XPS. Moreover, we have confirmed it by growing 5 ML Co on Ag(001) that there is a sharp peak at 0.5 eV in the valence band spectra corresponding to Co 3*d* band (not shown). For the film grown at 473 K (G3), there is no such feature corresponding to any Co^{3+} or metallic characteristic states, implying a stoichiometric CoO growth. The features ‘B’, ‘C’ of Co 3*d* origin and ‘D’, ‘E’, ‘F’, and ‘G’ in the Ag 4*d* and O 2*p* region does not change significantly with different growth conditions. So it is evident that the tuning of substrate temperature is more crucial than the oxygen partial pressure as long as there is a minimum oxygen background pressure for stoichiometric CoO growth. In order to monitor the growth in the low coverage, the sensitivity of

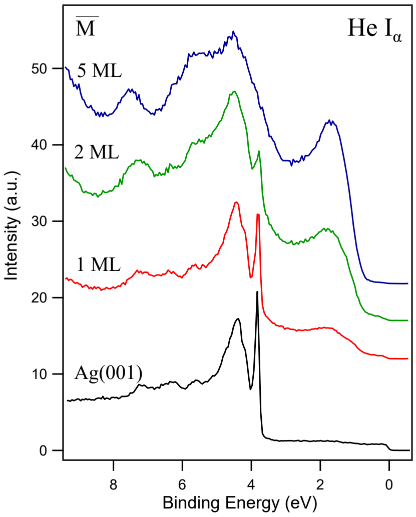

Figure 3.5: ARPES spectra at $\overline{M}$ point of Ag(001) with the different coverages of CoO film. The intensity variation of Tamm-surface state(SS) of Ag(001) with film coverages is shown using He I_α photon energy.

Tamm-surface state (SS) of Ag(001) to surface conditions such as surface adsorption, surface order, surface potential *etc.* has been employed. The Tamm-like surface state at $\overline{M}$ symmetry point of Ag(001), originates due to the lower surface potential of the topmost Ag layer and appears at 3.9 eV binding energy position with a sharp intense peak [122]. ARPES spectra at the $\overline{M}$ point of Ag(001) along with the spectra of 1, 2, and 5 ML CoO films grown at 473 K (G3) are shown in Fig. 3.5. The clean Ag(001) exhibit a strong peak at 3.9 eV binding energy due to the emission from the Tamm SS. Upon deposition of 1 ML CoO, the intensity of SS peak decreases but not very significantly. For 2 ML film coverage also we observe the presence of Tamm SS, but now with diminished intensity. The presence of SS up to 2 ML coverage is a clear indication of the lack of layer-by-layer growth as the intensity of SS is a measure of the bare Ag(001) patches exposed after film deposition. For the full monolayer coverage of material on Ag(001), the SS intensity should vanish completely as no bare Ag(001) surface will be present on the sample [123]. Thus, the observation of non-vanishing SS intensity at 2 ML coverage indicates a lack of complete wetting of

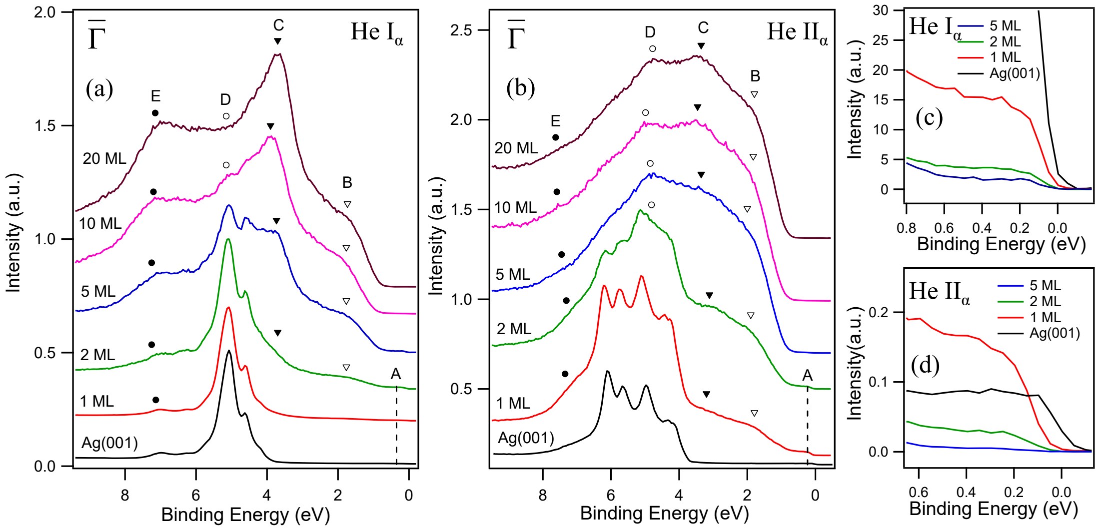

Figure 3.6: Coverage dependent ARPES spectra of CoO with clean Ag(001) at $\overline{\Gamma}$ point using (a) He I$_\alpha$ and (b) He II$_\alpha$ photon energies. (c)-(d) The zoomed-in view of spectra near the Fermi level for He I$_\alpha$ and He II$_\alpha$ photon energies, respectively.

the substrate surface with 3D islands formation. At 5 ML coverage, the SS disappears completely suggesting that complete wetting of Ag(001) surface has been achieved. This was one of the main reason for choosing 5 ML CoO as a nominal coverage for growth optimization. Fig. 3.6(a)-(b) shows the coverage dependent ARPES spectra at $\overline{\Gamma}$ point of CoO(001) films grown under optimized condition (G3) along with clean Ag(001) using He I$_\alpha$ and He II$_\alpha$ photon energies, respectively. Upon deposition of 1 ML CoO film, the density of states appears close to the Fermi edge is denoted by 'A' [see Fig. 3.6(a)-(b)]. These states were visible up to 5 ML and 2 ML film coverages for He I$_\alpha$ and He II$_\alpha$, respectively, due to their different penetration depth. Apart from these states, the valence band structure of Ag substrate is almost preserved after deposition of few initial CoO layers, indicating a weak interaction with the CoO films. For higher coverage, these interfacial states were disappeared, showing the insulating character of CoO films. Similar density of states near Fermi edge in the lower film coverage has been observed for NiO/Ag(001) [3–5] and MnO/Ag(001) [6] systems. Yang *et al.* [4] concluded that features near E$_F$ originate from hybridized states between Ag 5*s* band and the states of Ni 3*d* and O 2*p* originating from the interfacial NiO layer. Cheng *et al.* [3] observed similar density of states near E_F for 2 ML NiO film though no such density of states was observed for 2 ML CoO film in contradiction to our experimental findings. In case of NiO [5] and MnO [6] growth on Ag(001), we have also confirmed the presence of hybridized interfacial states for low coverage films. Here, we have observed similar interfacial features near E_F with maximum intensity at 1 ML film coverage and decreases with further increase in CoO film coverage as shown in Fig. 3.6(c)-(d). As the features are originating at the interface between Ag and CoO layers due to the weak hybridization between the Ag 5*s* band and the Co 3*d* and O 2*p* states, the effective hybridization does not enhance with increasing film coverage. With further CoO deposition, the interfacial features attenuated by the CoO overlayer as the photoemission intensity is limited by the inelastic mean free path (IMFP) of the photoelectrons. Thus, as seen in Fig. 3.6(c)-(d), the intensity of the states near E_F decrease with increasing coverages confirming the interfacial nature of these states. Intensities of the features 'B', 'C', and 'E' are found to increase with the film coverages indicating their association with CoO features. The feature 'D' appearing near 5 eV is modulated by the intense Ag 4*d* bands in the lower film coverages for He I_α, though is more distinctly visible with He II_α photon energy. The feature 'E' observed around 7 eV BE was distinctly visible after 10 ML film coverage for He I_α while it shows very low intensity with He II_α. The feature 'B' (at 1.7 eV) is assigned to the charge transfer $d^7\underline{L}$ final state where $\underline{L}$ signifies a hole on a ligand site. The assignment of feature 'C' (at 3.65 eV) is more complex in terms of charge transfer model. Here, we do not observe any significant dispersions of these features with CoO film coverage. The feature 'B' is a general feature of bulk CoO as it has been observed by several groups in CoO(001) [56, 100, 124] and in CoO(111) [108] as well. The other two features 'D' and 'E' are assigned to the delocalized O 2*p* bands. It is clear from Fig. 3.6(a) and (b) that the electronic structure of the films evolve as a function of the film coverages, with the thicker films (>10 ML) behaves like bulk CoO film [108], though we do not observe significant dispersion of the features with film coverage.

3.4 Introduction to polar cobalt oxide: CoO(111)

Electronic structure of CoO(111) surface has also been a matter of scientific interest since long time. Nowadays, polar surfaces of metal oxides grab attention in fundamental research due to their complex stabilization mechanisms [7] which are far from being well understood. The polar surface of CoO(111) consist of alternate stacking of cation (Co^{2+}) and anion (O^{2-}) layers brings a net dipole moment normal to the surface [8] leading to a surface instability. The understanding of stabilization mechanism of polar surfaces even for the structurally simplest (111) surfaces of rock-salt metal oxides, still remains a challenge. It is almost impossible to cleave the bulk oxide single crystals in the (111) direction and it is often problematic to prepare a stoichiometric and structurally smooth, well-ordered polar oxide surfaces with low defect densities. From a theoretical perspective, it has been shown that to obtain surface stability, the polar surfaces goes through different possible processes [9] such as adsorption of contaminations, hydroxylation, reconstructions, faceting, modification of surface electronic structure and charged surface nano-defects. The (111) polar surfaces of several rock-salt oxides, such as NiO, MgO, FeO, and MnO have been intensively investigated both experimentally and theoretically [9], but a little is known about polar CoO(111) surfaces. Hassel *et al.* [10] have grown epitaxial CoO(111) film on Co(0001) which is terminated by hydroxyl groups. They have explain the stabilization process by adsorption of OH as a means of surface charge reduction which form a more stable adsorbate layer by the adsorption of NO molecules on the surface. A grazing incident X-ray diffraction study [11] describes the stabilization of CoO(111) surface by a 50 Å thick spinel Co_3O_4 overlayer on top of the polar surface. Here, we have grown polar CoO(111) film of different coverages on Ag(111) substrate and study their surface structural properties by LEED and characterize the core and valence band electronic structures using XPS and ARPES techniques, respectively. For the growth of polar CoO(111) on Ag(111), similar growth procedure has been followed as CoO(001) on Ag(001) which is already discussed earlier in this chapter.

3.4.1 Surface structure of CoO/Ag(111): LEED study

Surface structure of CoO thin film grown on Ag(111) surface has been investigated by LEED study. The formation of multi-faceted structure and reconstructed CoO(111) surface are shown in Fig. 3.7(a)- (f). Different type of faceted LEED pattern are observed with increasing incident electron beam energy and film coverage. For 2 ML film, a 12-fold symmetric LEED pattern was observed for beam energy 55 eV

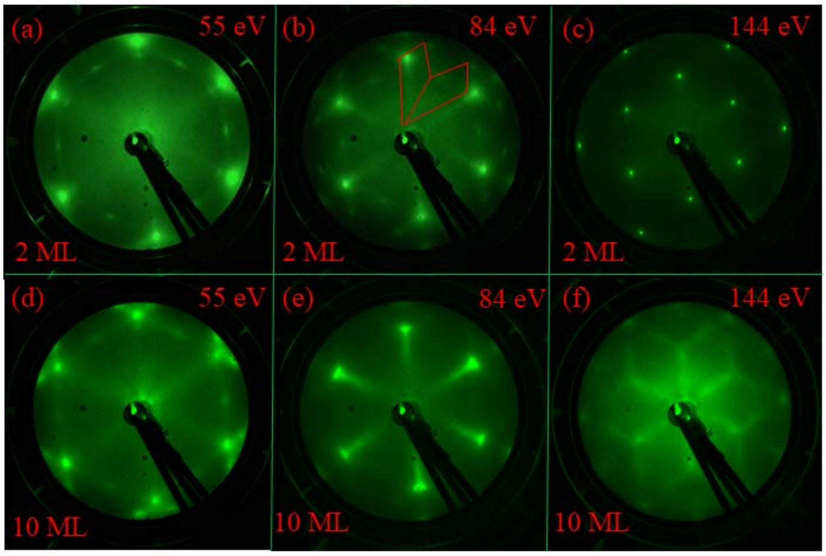

Figure 3.7: (a)-(c): Low energy electron diffraction(LEED) pattern at 55, 84 and 144 eV beam energy for 2 ML CoO film, respectively. Fig. (d)-(f): LEED pattern at 55, 84 and 144 eV beam energy for 10 ML CoO film, respectively. In Fig. (a)- (c), three differently reconstructed LEED pattern of 2 ML CoO films are shown. Here we observe a 12-fold symmetric LEED pattern for beam energy 55 eV whereas a multi-domain structure is observed for beam energy 84 eV. The regular hexagonal $p(1 \times 1)$ pattern has been observed at 144 eV beam energy. Fig. (d)-(f): The evolution of the faceted patterns with film coverage is shown for 10 ML coverage.

whereas a multi-domain structure was observed for beam energy 84 eV as shown in Fig. 3.7(a)-(b), respectively. The regular hexagonal p(1×1) pattern has been observed at 144 eV beam energy in 2 ML film coverage. At 10 ML film coverage, the 12-fold symmetric LEED spot intensity get enhanced and starts appearing a faint stripe-like faceted pattern connecting each spots [see Fig. 3.7(d)]. At higher beam energy, the stripes are prominently visible (84 eV) with the regular hexagonal LEED p(1×1) pattern (144 eV). Upon increasing coverage, the electrostatic potential developed in the film due to the increasing non-zero dipole moment of CoO(111) surface, resulting in the formation of these stripe-like faceted LEED patterns to obtain surface stability. Recently, the stabilization of polar CoO(111) surface grown on Ir(100) has been explained by the termination of thin slab of wurtzite-type CoO with a $(\sqrt{3} \times \sqrt{3})$R30° surface reconstruction [125]. Here, we have also observed a multi-domain reconstruction in the LEED for low film coverage. However, the surface is stabilized by the formation of high intensity stripe-like faceted structure over the LEED superstructure for the higher film coverage.

3.4.2 Core-level and valence band electronic structure of polar CoO(111)

The core level electronic structure was probed by monochromatic Al K_α X-ray photons of 1486.6 eV energy. The Co $2p$ and O $1s$ spectra of three different film coverages are shown in Fig. 3.8(a)-(b). Co $2p$ core level spectra shows Co $2p_{3/2}$ and Co $2p_{1/2}$ peaks at 780.3 and 796.2 eV with two corresponding shake-up satellites (S) at 786.5 and 803 eV binding energy, respectively. The shake-up satellite peaks are the characteristic feature of stoichiometric CoO. Fig. 3.8(b) shows the O $1s$ core level spectra for the different film coverages of CoO. All these peak features and the peak positions are well matching with the non polar CoO(001) film, which has been

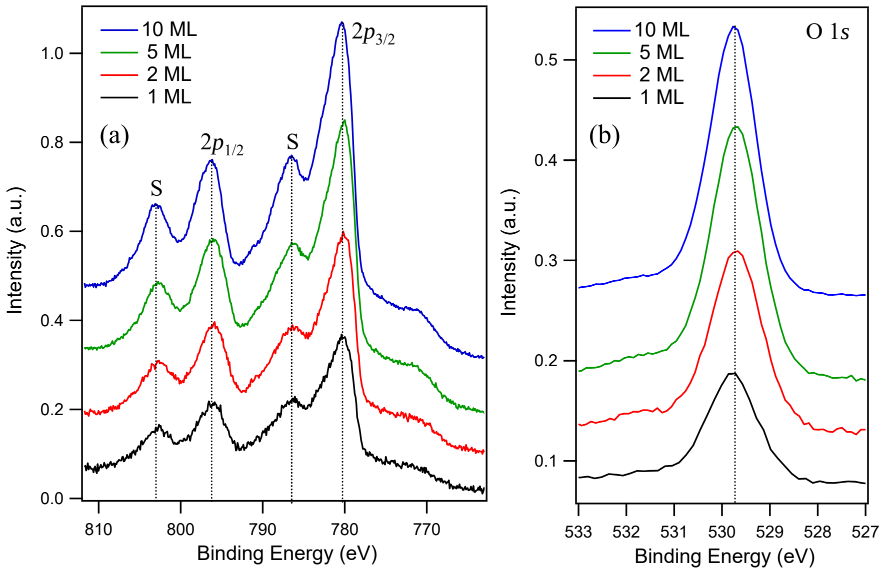

Figure 3.8: XPS core levels of (a) Co 2p (b) O 1s for different CoO film coverages.

discussed in detail in the previous section, suggesting the CoO stoichiometry of the film.

Fig. 3.9 shows the valence band ARPES spectra of bare Ag(111) along with different CoO film coverages at $\overline{\Gamma}$ point. In the ARPES spectra of clean Ag(111) surface, a Shockley type surface state (SS) [126] of Ag appears (feature A), near the Fermi level. Upon deposition of 1 ML CoO, the SS was still present in the spectra, but with a reduced intensity. The presence of the SS even after deposition of 1 ML CoO film indicates that the film does not completely wet the Ag(111) substrate, so the SS feature is appearing from the bare Ag(111) region. The SS peak vanishes for 5 ML coverage suggesting that the film has covered the entire surface. As the film coverage increases, the contribution from the Ag(111) substrate decrease and only the CoO electronic states dominate the spectrum. The feature B about 1.5 eV binding energy is assigned to be $d^7\underline{L}$, where $\underline{L}$ stands for ligand hole states. The features C, D, E in the 4-7 eV binding energy range are mainly oxygen 2*p* states with some admixture of Co 3*d* band. We do not observe any significant dispersions of these states with the film coverages. The feature E around 7.2 eV is absent for the case of

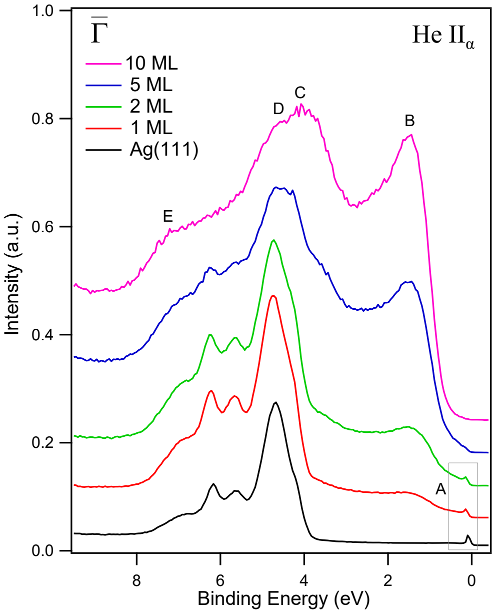

Figure 3.9: ARPES spectra of different CoO film coverage.

non-polar CoO(001) [see Fig. 3.6(b)] which could be due to the redistribution of the surface electronic structure due to the polar surface of CoO(111). Possible changes of electronic structure for the polar surface is already theoretically predicted [9]. Further, for the detailed understanding of the facet structures, microscopic experiments are necessary and is beyond the scope of the thesis.

3.5 Summary

In this chapter, growth, and characterization of CoO films on Ag(001) and Ag(111) substrates have been studied in detail. The combined core level and valence electronic structure study reveal the non-stoichiometric features under different growth conditions of CoO on Ag(001). The well-ordered stoichiometric growth of CoO has been observed at 473 K substrate temperature and 1×10^{-6} mbar oxygen background pressure. The pseudomorphic growth in the initial few layers followed by the gradual strain relaxation close to the bulk lattice was confirmed by the coverage dependent LEED study. The appearance of mosaic structure within 5-10 ML coverage range was explained by means of tilted growth of mosaic grain along the glide plane due to the buried misfit dislocation network at the interface. The Tamm-like surface state of Ag(001) depicts the quasi-2D growth of CoO in the low film coverage. The coverage dependent evolution of valence electronic structure of the optimized CoO film was investigated by ARPES. The interfacial state which is visible up to 5 ML film coverage originates due to the hybridization between Ag $5s$ band and the Co $3d$ and O $2p$ states. These interfacial states were observed in the stoichiometric CoO films grown at the optimized condition suggesting an intrinsic origin. This seems a general feature of transition metal monoxides as it has been observed in NiO, MnO, and CoO as well. With increasing coverage, these interfacial states gradually disappear and mostly non-dispersive CoO bands appear in both He I_α and He II_α spectra.

The polar CoO has also grown on Ag(111) and probed the surface structure by LEED. Evolution of the faceted and multi-domain surface structure with incident beam energy and film coverage has been investigated. Although there are many processes involved to stabilize the polar surface, for CoO(111) we find that it is stabilized by the formation of stripe-like faceted structure in the higher film coverages. Redistribution of the electronic density of states also realized from the photoemission spectra of polar CoO. The core level and valence band electronic structures are the average information obtained by summing over contributions from these different facets. Further, we show that core level binding energies do not get affected by the formation of facet structures which is confirmed by XPS studies.

4

Growth and coverage dependent electronic structure of MgO on Ag(001)

4.1 Introduction

The field of simple metal oxides has grabbed the attention of many researchers due to their versatile technological applications as well as for the basic understanding of the oxide-metal interfaces [127–130]. Especially, metal-supported ultrathin oxide films have been extensively used in various fields such as catalysis, spintronics or nanoelectronics [131, 132]. It is well-known that physical properties of the correlated oxide systems are determined by a few fundamental quantities. The on-site Coulomb interaction U is one of the most important quantities, related to the correlated motion of electrons between the open transition metal (TM) $3d$ shell and the corresponding multiplet structure. The charge transfer energy (Δ) is another important quantity defined as the energy required to transfer an electron from the O $2p$ to the TM $3d$ orbitals [30]. The values of U and Δ relative to the bandwidth defines the nature, and magnitude of the conductivity gap. Modifications of these values can give rise to remarkable changes in the properties of these materials, like changes in the magnitude

---

The work presented in this chapter has been published in Surface Science, ***677****, 60-67 (2018).*

of the conductivity gap and strength of the various exchange and superexchange interactions [31, 58]. In general, the variation in the strength of these exchange interactions leads to changes in the transition temperatures of various phase transition phenomena. The most convenient way to change these basic electronic structure parameters U and Δ is by growing a few layers of oxide on a metal substrate or as an oxide/metal multilayers [32–34]. In order to avoid the complexity of correlation effects in $3d$ TM oxides, MgO was chosen due to its closed-shell electronic structure over TM oxides. Moreover, MgO has a similar crystal structure and lattice parameter compared to some TM oxides and may serve as a model system to investigate the changes in their basic electronic structure parameters. Further, MgO is used as a substrate for the growth of many TM oxide films and will be important to understand the substrate electronic structure.

The MgO/Ag(001) is an important model system to study the metal-oxide interfaces as they have a small lattice mismatch and grows in a layer-by-layer fashion up to several monolayers (MLs) [35]. Despite the extensive use, understanding of the electronic structure and properties of MgO is still far from satisfactory as the use of electron spectroscopic techniques are hindered due to the charging effects for its insulating nature. Though there are several structural studies performed on this system in the literature, detailed study of the interfacial and coverage dependent electronic band structure are still limited [36–38]. The growth of a well-ordered unreconstructed MgO(001) surface on Ag(001) is challenging even though they have a small lattice mismatch (~3%) between them. There are several reports where thin films of MgO have been grown on different substrates by reactive deposition of Mg in oxygen environment [35, 133–135]. Wollschlager *et al.* [35] have grown MgO film on Ag(001) by reactive deposition of Mg in presence of oxygen atmosphere and they have observed the growth of mosaic-like structure by spot-profile analysis low energy electron diffraction (SPA-LEED). The growth of monolayer MgO on Ag(001) forms the corrugated islands which have transformed into extended flat terraces upon controlling the thermodynamic constraints by post-growth treatments [136]. The generation of characteristic oxygen vacancies and nonstoichiometric MgO on Ag(001) has been investigated by Peterka *et al.* [137] using XPS and electron energy loss spectroscopy (EELS). Moreover, the image charge screening and charge fluctuations at the oxide-metal interface have been extensively studied by different groups [32,33,138]. Altieri *et al.* [33] have demonstrated that the Coulomb and charge transfer energies in MgO layers deposited on highly polarizable Ag(001) substrate are reduced significantly from their bulk values. This efficient image potential screening provides a new way to alter different properties and transition temperatures of correlated oxide thin films [29].

4.2 Experimental details

All the experiments were performed in a standard ultra-high vacuum spectrometer having base pressure better than 8×10^{-11} mbar. Mechanically polished Ag(001) substrate has been cleaned by the repeated cycles of Ar^+ ion sputtering (600 eV, 1 μA, 1×10^{-6} mbar) and annealing to 823 K. The well-ordered crystalline quality and the cleanliness of the Ag(001) surface were confirmed by LEED and XPS, respectively. Metallic Mg was evaporated from a homemade resistive evaporator with a deposition rate of 0.3 ML/min as monitored by the quartz crystal thickness monitor. During Mg deposition, 1×10^{-7} mbar oxygen background pressure was maintained in the preparation chamber for simultaneous oxidation and the substrate was kept at 473 K. A K-type thermocouple connected to the substrate was used to measure the sample temperature. In order to improve the crystalline quality, post-growth annealing was performed at 673 K with the same oxygen background pressure for 15 min. After completion of growth, the sample was transferred to the 4 grid LEED apparatus within the preparation chamber where a high sensitivity 12-bit Peltier cooled CCD camera was used to collect the LEED images. The sample was further transferred to the analysis chamber for photoelectron spectroscopic measurements. The spectroscopic measurements were performed using a VG SCIENTA-R4000WAL electron energy analyzer. We used Al K_α monochromatic X-ray source to excite the photoelectrons from sample surface for XPS measurements while monochromatized He I_α (21.2 eV) and He II_α (40.8 eV) resonance lines were used for ARPES measurements [88]. All the XPS and ARPES measurements were performed at RT with total experimental energy resolutions better than 0.6 eV and 0.1 eV, respectively, including the thermal broadening near the Fermi energy.

4.3 Experimental results and discussion

4.3.1 Low energy electron diffraction study

After completion of growth, the samples were cooled down to RT and transferred to LEED set up for investigating the crystalline quality as well as the crystallographic symmetry directions from the LEED pattern. Fig. 4.1(a)-(d) represents the coverage dependent LEED patterns for 1-20 ML MgO films at 55 eV primary electron beam energy. For the lower film coverage regime (1 - 5 ML) [see Fig. 4.1(a) and (b)], MgO grows almost with the same lattice parameter of Ag accommodating the interfacial lattice strain. The observation of sharp $p(1 \times 1)$ LEED spots with low background intensity is an indication of the atomically clean well-ordered MgO(001) surface. As the film coverage increases further, the spots get broader with an enhanced background intensity as shown in Fig. 4.1(c) and (d). Inset of each LEED images shows the zoomed-in view of the (1,0) spot to clearly visualize the weak intensity features around the spots. In Fig. 4.1(e), the average radial intensity profiles of LEED spots has been plotted for different film coverage. The radial profile plot of the LEED spots shows how the intensity decreases radially with increasing distance from the centre of the spot. The sharpness of the radial profile plot provides the qualitative information about the structure of the film. The best quality film with

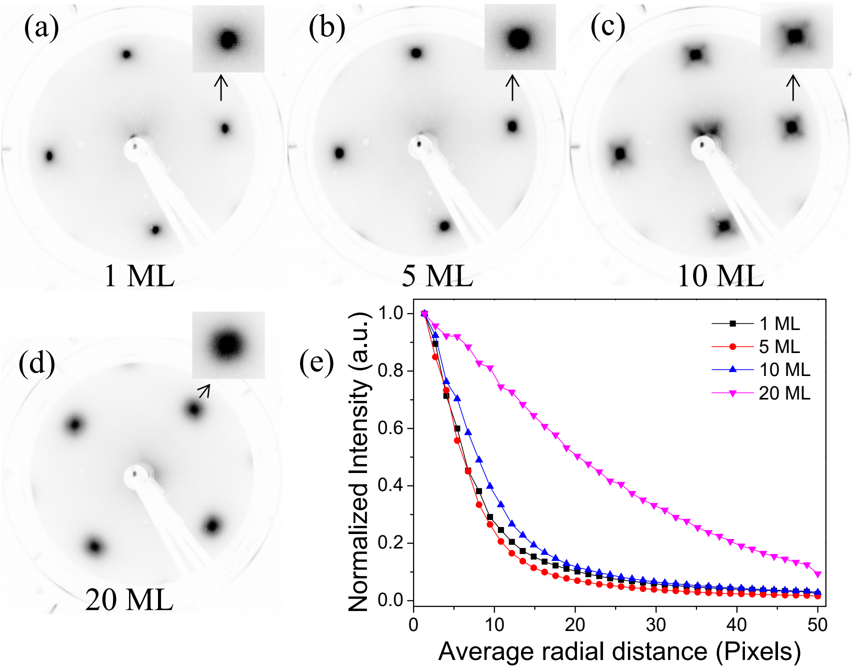

Figure 4.1: LEED patterns of different MgO film coverages. (a)-(b) In the lower coverage regime 1-5 ML, a sharp LEED spot with very faint mosaic structure are shown. (c) The high-intensity fourfold mosaic structure was observed at 10 ML film coverage. (d) At 20 ML, mosaic structure disappears and a high-intensity background around each LEED spot was observed. (e) The average radial intensity profile of LEED spots for different film coverages.

the highest atomic order should show the steepest curve and with smallest full width at half maximum (FWHM) of the spots. The overall quality of the spots is almost same up to 10 ML film coverage as the radial profiles are closely lying to each other maintaining almost the same FWHM. However, the intensity profile of 20 ML film is found to be decaying much slower than others as the surface crystalline quality of the film degrades with increasing coverage and as a consequence, the spots become broader with enhanced background intensity. This weak intensity variation around the main spot [see the inset of Fig. 4.1(d)] is a clear indication of the increased defect density in the film. The 10 ML film [see Fig. 4.1(c)] shows a clear mosaic structure in the LEED pattern. The lattice mismatch produces a strain at the film-substrate

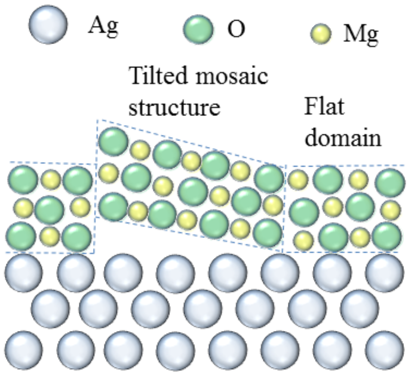

Figure 4.2: The schematic of the mosaic structure formation by the misfit dislocations at the film-substrate interface.

interface for the pseudomorphic growth. Thus, misfit dislocations are introduced at the interface to relax the strained structure and to minimize the surface energy [139]. In MgO films, misfit dislocations with (110) glide planes are known to develop for film coverages larger than 1-2 ML resulting in mosaic structure formations [140]. A faint mosaic structure starts appearing at 5 ML film and it is prominent at ∼10 ML film coverage [see the inset of Fig. 4.1(b) and (c)]. For higher film coverages, mosaics are expected to decrease due to the strain relaxation. No mosaic structure was observed at 20 ML while a high-intensity background around each LEED spot [inset of Fig. 4.1(d)] was observed as mentioned before. Earlier studies reveal that mosaics appear at the closure of the first layer and finished after a coverage of 7 ML of MgO on Ag(001) [35, 140]. On the contrary, we have observed the most intense mosaics at 10 ML coverage which is quite similar to the report of Dynna *et al.* [141] on MgO/Fe(001) system where they have shown that mosaics started to grow at a critical coverage of 8 ML at RT. In Fig. 4.2, a model for the mosaic formation due to misfit dislocations at the interface is presented schematically [35, 140, 142]. The fourfold satellite spots around each LEED spot, as observed in the 10 ML film, appear due to this tilted mosaic structure at the interface. The other possibility could be the edge dislocations due to the misfit at the interface if the Burger vector has a component along the out-of-plane of the interface [143]. The misfit dislocations can be created only after a critical coverage as only then the film relax and release the required energy for the formation of dislocations [144]. Thus, the strain-layer epitaxy is possible up to a critical coverage, at which point the overlayer relaxes either by agglomeration, misfit dislocations or both. The expected critical coverage is typically ∼8 to 15 Å for a ∼3% mismatch [145]. So the ∼3% lattice misfit of MgO/Ag(001) interface would correspond to a critical coverage of 4-8 ML of MgO. Hence, the observed mosaic structure for 5-10 ML MgO coverage is consistent with the model as described above.

4.3.2 Core level electronic structure

Fig. 4.3(a)-(b) shows the Mg 1*s* and 2*p* core levels for different coverages of MgO. In case of the bulk single crystal of MgO, electron spectroscopic measurements are hindered due to the charging effects. In our study, to rule out the issue of charging effect in the film, we have varied the incident X-ray intensity by changing the X-ray source power and have monitored the core level peak position. No core level peak shifts were observed with intensity variation indicating the absence of the charging effects, as expected due to the proximity to the metallic Ag(001) substrate. The zero of the binding energy scale was fixed at the Fermi level of a cleaned polycrystalline Ag foil. Fig. 4.3(a) shows the Mg 1*s* spectra for several film coverages. Here, as the coverage decreases the core level shifts towards lower binding energy scale, about 0.2 eV, 0.7 eV and 1.1 eV for the 10 ML, 5 ML and 1 ML films, respectively, relative to the 20 ML film, considering the 20 ML MgO film as the bulk. Similar behavior is also observed for Mg 2*p* core level spectra [see Fig. 4.3(b)] as the core level shifts towards lower binding as a function of decreasing film coverages. The Mg 2*p* core level also shifts by 0.3 eV, 0.9 eV and 1.5 eV for the 10 ML, 5 ML and 1 ML films, respectively, *w.r.t* 20 ML MgO film. In Fig. 4.3(c), we show the coverage dependence

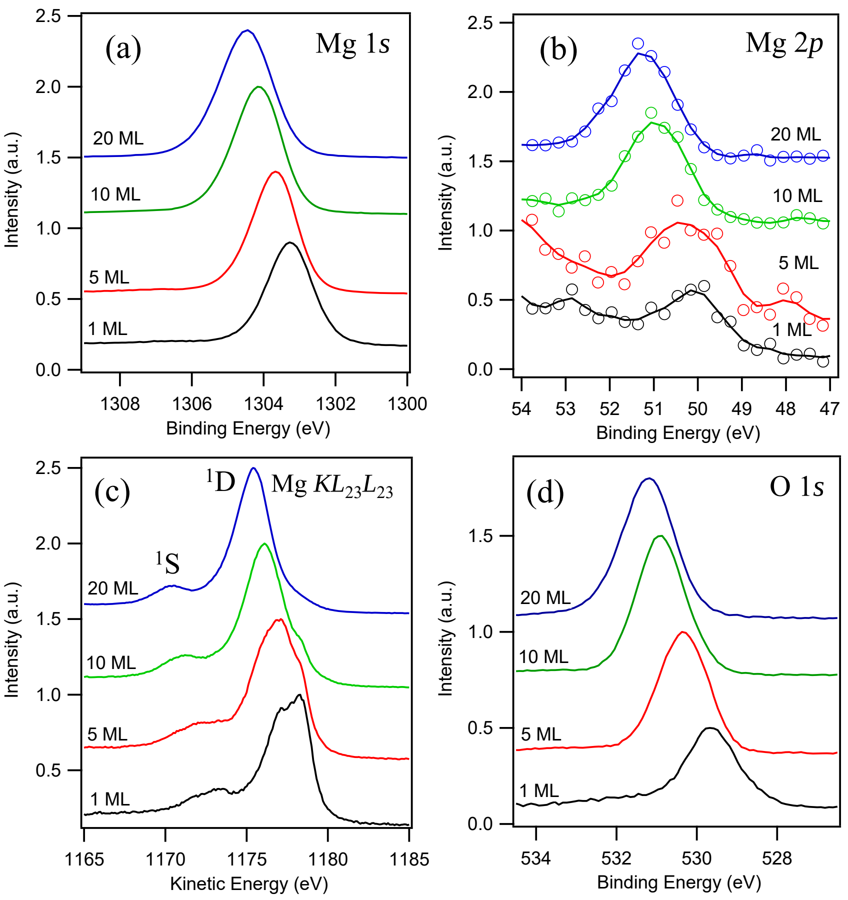

Figure 4.3: (a) Mg 1*s* core levels of the 10 ML, 5 ML and 1 ML film shift towards the lower binding energy by 0.2 eV, 0.7 eV and 1.1 eV respectively, *w.r.t* the 20 ML film. (b) Mg 2*p* core level shifts by 0.3 eV, 0.9 eV and 1.5 eV for the 10 ML, 5 ML and 1 ML films, respectively, *w.r.t* the 20 ML MgO film. (c) Mg $KL_{23}L_{23}$ Auger spectra of MgO(001) films on Ag(001). With ^1S to ^1D multiplet splitting of the Mg $2p^4$ Auger final state being constant for all coverages, a rigid shift of 0.7 eV, 1.7 eV, and 2.9 eV *w.r.t* the 20 ML MgO is observed for the 10 ML, 5 ML, and 1 ML films, respectively. (d) O 1*s* core levels of the 10 ML, 5 ML, and 1 ML film shift towards lower binding energy by 0.3 eV, 0.8 eV, and 1.5 eV respectively, *w.r.t* the 20 ML film.

of the Mg $KL_{23}L_{23}$ Auger transition. Relative to the 20 ML MgO, a shift of 0.7 eV, 1.7 eV and 2.9 eV was observed for the 10 ML, 5 ML and 1 ML films, respectively. These shifts are more than those for Mg 1*s* and Mg 2*p* while, the ^1S to ^1D multiplet splitting in the Mg $2p^4$ Auger final state (5.2 eV) is found to be a constant for all coverages, as expected. O 1*s* spectra [Fig. 4.3(d)] also displays large core level shifts towards lower binding energy scale as a function of decreasing film coverage. The O 1*s* shifts by 0.3 eV, 0.8 eV, and 1.5 eV for the 10 ML, 5 ML, and 1 ML films, respectively, *w.r.t* 20 ML film.

The binding energy shifts of the core levels with film coverage for MgO/Ag(001) system has been extensively studied by Altieri *et al.* [33]. C. J. Nelin *et al.* have also observed similar surface core level shift of 30 ML MgO film on Mo(100) by grazing angle XPS measurement [146]. Moreover, they have explained the pronounced decrease of line widths of MgO ionizations with decreasing MgO films thickness using cluster model calculations [147]. By accounting the effect of image charge screening, they have successfully explained these core level shifts. Using the approach suggested by Altieri *et al.* [33], we have found that Coulomb (U) and charge-transfer (Δ) energies in 1 ML MgO film are reduced by as much as 1 eV and 1.4 eV, respectively, *w.r.t* 20 ML MgO film. Yang *et al.* [34] have also demonstrated that U and Δ in correlated oxide layers deposited on a highly polarizable metallic substrate are reduced significantly from their bulk values. These results indicate the large reduction of U and Δ values due to the image potential screening but also there is a significant countering effect associated with the appreciable loss of polarization energy by the oxides itself due to the finite size effect near the interface.

4.3.3 Valence band electronic structure

In Fig. 4.4, the ARPES band dispersion (left panel) and their second derivatives (right panel) along the $\overline{\Gamma} - \overline{X}$ symmetry direction of the SBZ are shown for four different MgO(001) film coverages, together with that of the clean Ag(001) substrate. The second derivative of the ARPES data, extracted following Zhang *et al.* [148], provides a better way of visualizing the weakly dispersive features. All the data were taken at RT using He II_α (40.8 eV) photons up to 10 eV binding energy below the

Fermi level (E_F). The valence band of Ag(001) primarily consists of the high-intensity feature of Ag 4*d* within the binding energy range of 4-7 eV and the Ag 5*sp* band approaching the E_F [see Fig. 4.4(a) and (b)]. Upon deposition of 1 ML MgO film, the intensity of the Ag 5*sp* band is reduced significantly relative to the bare Ag(001) [see Fig. 4.4(c) and (d)]. In the second derivative data, a non-dispersive flat feature is visible just below the E_F [see Fig. 4.4(d) and (f)], which is an artifact resulting

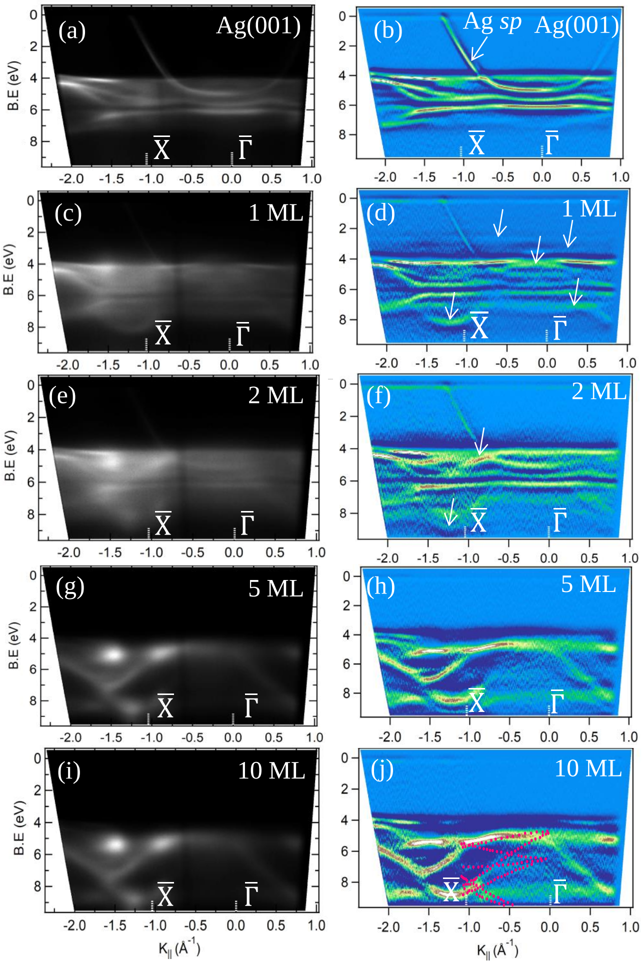

Figure 4.4: The band dispersions of Ag(001) and MgO/Ag along the $\overline{\Gamma} - \overline{X}$ symmetry direction using He II$_\alpha$. The band dispersions and the respective 2nd derivative of the band dispersions of Ag(001), 1 ML, 2 ML, 5 ML and 10 ML MgO are shown in (a)-(b), (c)-(d), (e)-(f), (g)-(h), (i)-(j), respectively. Different bands are shown using arrows only to guide the eyes. The calculated band dispersions [149] are traced by brown dotted curves to compare with 10 ML MgO band dispersions as shown in (j).

from the second derivative process due to the drastic changes in the photoemission intensity at the Fermi edge. At 1 ML, several MgO derived bands appear at 2.7 eV, 3.5 eV, 4.25 eV, 7.1 eV, and 8.15 eV below E_F as shown in Fig. 4.4(d) by arrows. The band dispersion at 4.25 eV and 8.2 eV are found to be consistent with the reported theoretical band structure for the 1 ML buckled MgO layer [149]. Though the direct comparison with the calculated band dispersions is difficult due to the different Fermi energy consideration in the calculation [149]. Two non-dispersive weak intensity bands at 2.7 eV and 3.5 eV and a dispersive band at 4.25 eV about $\overline{\Gamma}$ point has been observed for 1 ML coverage. These two non-dispersive bands disappear at 2 ML coverage. The dispersive band at 4.25 eV is also not prominently visible in 2 ML which could further support the origin of these bands due to the formation of the buckled layer for the 1 ML case. A more detailed calculation is needed for further understanding of the valence electronic structure of monolayer MgO film. At 2 ML, two highly dispersive bands appear at 4.6 eV and 8.9 eV as shown by arrows [see Fig. 4.4(f)]. With further increase in coverage, highly dispersive MgO derived bands are gradually shifted to higher binding energies relative to 1 ML film. Here the bands at 4.25 eV and 8.15 eV in 1 ML film are gradually pushed below with increasing coverage and they appear at 5 eV and 8.9 eV in 10 ML film, respectively. However, the band about $k_{||} = -2$ Å^{-1} [near the $\overline{\Gamma}$ point of 2nd SBZ] was fixed at 4 eV from 5 ML film coverage onwards. With further increasing coverage (20 ML) no further band shifts were observed (not shown). In Fig. 4.5, the ARPES band dispersion (left panel) and their second derivatives (right panel) along the $\overline{\Gamma}-\overline{M}$ symmetry direction are shown for the same four MgO coverages, besides the clean Ag(001) substrate. MgO derived bands along $\overline{\Gamma}-\overline{M}$ direction for 1 ML coverage can be identified at 2.75 eV, 4.25 eV, 7.1 eV and 7.3 eV binding energies [see Fig. 4.5(c) and (d)]. The band at 2.75 eV close to the $\overline{M}$ point is not visible for 2 ML coverage while a similar band is observed at 3.9 eV binding energy as the valence band maxima ($k_{||} = -1.85$ Å^{-1}) of the 5 ML film. The other MgO derived bands observed for 1 ML are also

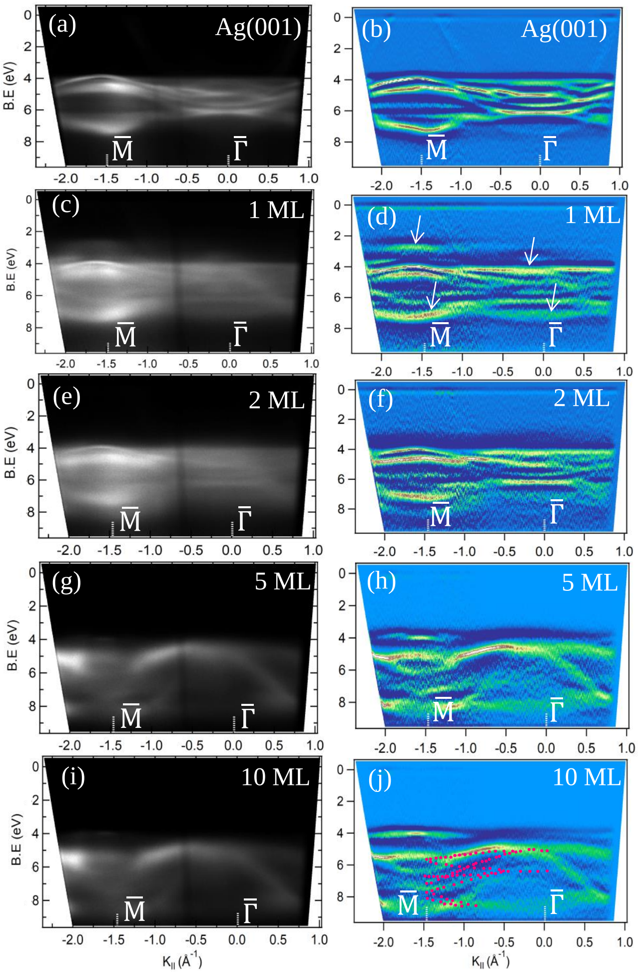

Figure 4.5: The band dispersions of Ag(001) and MgO/Ag along $\overline{\Gamma} - \overline{M}$ symmetry direction using He II$_\alpha$. The band dispersions and the respective 2nd derivative of the band dispersions of Ag(001), 1 ML, 2 ML, 5 ML and 10 ML MgO are shown in (a)-(b), (c)-(d), (e)-(f), (g)-(h), (i)-(j), respectively. Different bands are shown using arrows only to guide the eyes. The calculated band dispersions [149] are traced by brown dotted curves to compare with 10 ML MgO band dispersions as shown in (j).

found to be pushed down with increasing coverage as they are observed at 4.9 eV, 8.5 eV, and 8.8 eV in 10 ML film, respectively. However, the valence band maxima remain fixed at 3.9 eV with increasing coverage suggesting the formation of the bulk band gap of MgO film, though we measure only the gap below E$_F$.

The experimental band dispersions of 10 ML MgO film in both the symmetry directions are compared with the bulk electronic band structure obtained by DFT-

PBE [149]. The band at 5 eV matches well with the calculated band dispersion, a direct comparison of which is shown in Fig. 4.4(j) where the lines are taken from Shayeganfar *et al.* [149]. The highly dispersive band at 8.9 eV near $\overline{X}$ point [Fig. 4.4(j)] approaching the calculated band dispersion [149]. The band dispersions along $\overline{\Gamma} - \overline{M}$ direction also matches quite well with the calculated band dispersions [149], a direct comparison of which is shown in Fig. 4.5(j). The band at 4.9 eV and 7.5 eV matches accurately with the DFT-PBE results [149]. However, a few calculated bands are found to be absent in our experimental data as well, possibly due to the reduced photoemission cross sections of these energy bands for the used photon energy (40.8 eV).

It is reported in the literature that the energy band gap of 1 ML thick MgO adjacent to the metallic substrate is same as that of the bulk MgO surface [150]. However, we have observed a few MgO derived band due to the strong O 2*p*-Ag 5*sp* hybridization within 4 eV binding energy for the 1 ML coverage leading to the reduction of the insulating gap in proximity to Ag(001). These hybridized bands start disappearing at 2 ML coverage resulting in shifting the valence band maxima to 3.9 eV for higher coverages. Thus, similar to the core levels, the O 2*p* dominated MgO valence bands are also found to be gradually shifted to the higher binding energies with increasing coverage up to 10 ML. With further increase in coverage, the bands remain almost at the same binding energy positions as observed in 20 ML coverage (not shown). For instance, the band at 8.15 eV in 1 ML near $\overline{X}$ point is shifted by 0.75 eV to the higher binding energy going from 1 ML to 10 ML. However, the valence band maxima remain fixed at 3.9 eV binding energy for coverages above 5 ML, maintaining the band gap of bulk MgO. Using layer-resolved differential conductance measurements, it has been shown that the bulk band gap of 6 eV is formed even at 3 ML film of MgO [151] which is consistent with our results. Similar binding energy shifts have also been suggested from the angle-integrated ultraviolet photoemission spectra (UPS) of the MgO films grown on Ag(001) using a deconvolution procedure [150]. This band shifting could be explained by the image charge screening of a hole created by photoionization in the vicinity of Ag(001). As suggested by Altieri *et al.* [33], we have also observed that the effects of image charge screening due to the presence of oxide/metal interface are observable to coverages as high as 10 ML. Creation of a hole by the photoionization process leads to a relaxation of the other electrons to lower energy states to screen this hole. The creation of positive charge by photoionization is also accompanied by the simultaneous creation of a negative image charge in the metal which is in the proximity to the insulating layer [33, 138]. Using the classical image potential model for 1 ML MgO system, Kiguchi *et al.* [150] had shown $E_{image} = 3.6$ eV with a loss of polarization energy $\Delta E_{pol} = 3$ eV for going from the bulk to the monolayer, leaving a net gain of relaxation energy by 0.6 eV. Therefore, the observed binding energy shift (~ 0.75 eV) of the MgO valence band is close to the image charge results. The differences between the observed shift and the calculated energy difference could be due to the neglect of factors such as the dipole-dipole interaction and the expected deviations from the classical 1/r dependence of the image potential in the model [33].

In Fig. 4.6(a) and (b), we show the ARPES energy distribution curves (EDC) at $\overline{\Gamma}$ of various MgO film coverages along with the clean Ag(001) using He I_{α} and He II_{α} photons, respectively. Upon deposition of 1 ML MgO on Ag(001), there appears finite density of states as the valence band edge of 1 ML MgO/Ag(001) within 0- 4 eV binding energy range for both He I_{α} and He II_{α}. This valence band edge is shifted towards Fermi level relative to the Ag(001) valence band edge. With increasing MgO coverage, these states gradually disappear and the valence band edge is again shifted towards higher binding energy position at $\overline{\Gamma}$ due to image charge screening as explained above. This valence band shift with MgO film coverage is related to the change in work function (ϕ) of MgO/Ag system. In fact, it has been already estimated by UPS measurement that work function $\phi = 3.05 \pm 0.05$ eV for 2-5 ML MgO and $\phi = 3.30 \pm 0.05$ eV for 8-12 ML MgO on Ag(001) [152].

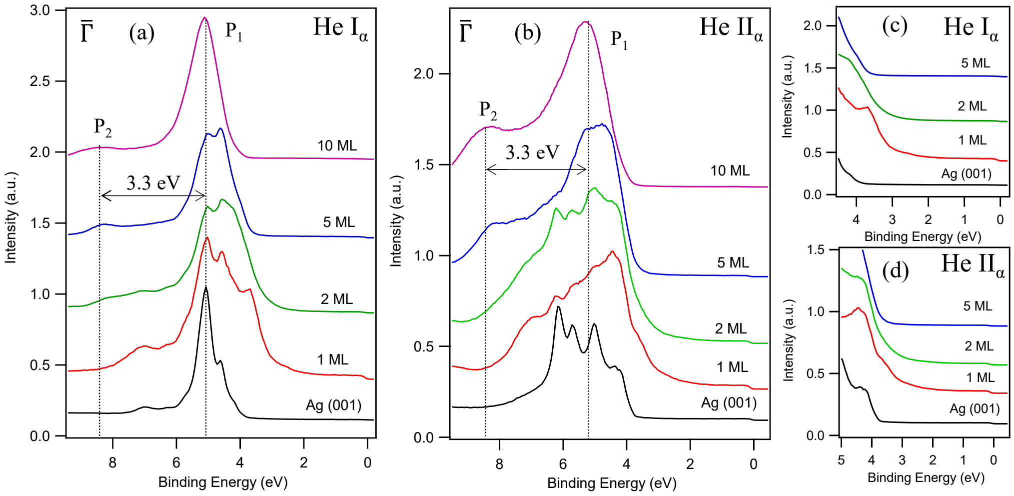

Figure 4.6: The coverage dependent angle-resolved energy distribution curves (EDC) at $\bar{\Gamma}$ point of MgO(001) films with clean Ag(001) spectra using (a) He I$_\alpha$ and (b) He II$_\alpha$ photon energies. The features within 0-4 eV binding energy are clearly shown using (c) He I$_\alpha$ and (d) He II$_\alpha$.

The states that appear at the interface of MgO/Ag between the Fermi level and 4 eV binding energy [see Fig. 4.6(c) and (d)] are mainly due to the interaction of O 2p with Ag 4d and Ag 5sp. The hybridization between Ag 4d and O 2p of MgO is not strong enough as one can expect for degenerate binding energy [36]. The features below 4 eV binding energy possesses a strong O 2p character which is extended towards Fermi level due to the strong hybridization with the wide Ag 5sp band. The enhancement of density of state of monolayer MgO film over a clean Ag(001) in the proximity of Fermi level was already confirmed by Butti *et al.* [37] using DOS calculations. In our case, with further increasing coverage, these states disappear resulting in a valence band gap about 3.9 eV from the Fermi level. From 5 ML onwards, no bands or any density of states were observed between 0-4 eV binding energy range. In the binding energy range of 4-10 eV, bulk-like MgO valence band is found with two O 2p peaks [labeled by P$_1$ and P$_2$ in Fig. 4.6(a)-(b)] separated by 3.3 eV are consistent with the literature [152].

4.4 Summary

Growth and coverage dependent electronic structure of MgO on Ag(001) has been investigated by means of LEED and photoemission spectroscopic studies. The appearance of the mosaic structure in LEED within 5-10 ML film coverage has been explained by the fact that the required energy for misfit dislocations will release only after a certain coverage by relaxing the strain of the film. The core level XPS peak shift with film coverage illustrates the change in on-site Coulomb (U) and charge transfer (Δ) energies of MgO layers deposited on highly polarizable Ag(001) substrate. The valence band electronic structure has been probed by ARPES using He I_α and He II_α photon energies. For the low coverage films, the presence of O $2p$-Ag $5sp$ hybridized bands near the Fermi level reduced the MgO bulk band gap substantially as a result of the finite size effects in the proximity to the metallic substrate. As the coverage increases, few bands pushed below, towards higher binding energy up to 10 ML film coverage. However, from film coverages 5 ML onwards, the valence band maxima remain at the same binding energy position resulting in the bulk MgO band gap. This valence band shifting has been explained by the image charge screening effect in the oxide-metal interface. The band dispersions are in good agreement with the theoretical bulk band dispersions for the 10 ML film, however, a rigorous calculation is necessary to understand the monolayered MgO band structure properly. In the higher film coverage, the features near the Fermi level disappear and mainly the bulk sensitive MgO bands were observed from 4 eV below the Fermi level in both the symmetry directions.

5

Electronic structure and surface antiferromagnetism of CoO/Ag(001)

5.1 Introduction

Electronic structure of transition metal monoxides like NiO, CoO has been a major topic of interest in condensed matter physics since last few decades [153–157]. This field grabbed more attention after the discovery of the cuprate superconductors where the electronic correlations were also found to be very important [12]. There are several interesting aspects of the electronic structure of TM monoxides such as electron correlation effects, antiferromagnetic (AF) order and translational symmetry boosted researchers to explore the field of TM oxides further. The correlation effects due to the strong Coulomb interactions are well-known in transition metal monoxides. The electron correlation causes the breakdown of the one electron picture of these materials which led to the famous Mott-Hubbard picture of insulators [13]. NiO and CoO are well-known antiferromagnetic insulators below their Néel temperatures (T_N) at 523 K and 291 K, respectively. The AF order in these oxides also an important correlation phenomenon need to be considered in the band structure description [14]. The translational crystal symmetry also plays an important role to describe the electronic structure of the crystalline materials. Among these aspects, the correlation effects are the extensively discussed and controversial issue [14, 53–55]. In the Mott-Hubbard picture, due to the strong Coulomb interaction between the $3d$ electrons leads to an energy gap of several eVs between the filled and empty states in the $3d$ band. A combination of Becke's three-parameter exchange functional and the Lee-Yang-Parr correlation functional (B3LYP) calculations [15] predict the insulating character of CoO correctly in the antiferromagnetically ordered phase with a gap of 3.5 eV, although this gap is larger than the gap of 2.5 eV, estimated by the combined study of XPS, bremsstrahlung isochromat spectroscopy (BIS), and X-ray-absorption spectroscopy (XAS) [16]. Oguchi *et al.* [55] performed self-consistent augmented spherical-wave band calculations which included a treatment of exchange and correlation within a local-spin-density formalism. Their results show that the band structure is strongly dependent upon the magnetic ordering and, in particular, that CoO is an insulator with the antiferromagnetic ordering along [111] direction, as observed experimentally [18]. Their calculations also predict the possibility of having an insulating state due to the population imbalance in the minority-spin t_{2g} band induced by the intra-atomic exchange interaction. On the other hand, the bulk magnetism of many binary (NiO, CoO, MnO) or complex oxides (Cr_2O_3, Mn_3O_4, $BaTiO_3$, *etc.*) are well understood but little is known about their surface magnetic properties even for the simple binary oxides in the reduced dimension. The possible reason could be the lack of availability of high-quality oxide surfaces to obtain reproducible results and difficulties in the electron spectroscopic measurements due to the insulating nature of most of the bulk oxides [158, 159]. Another issue is that cleaved surface of oxides single crystals is often with poor crystalline quality consisting of high terrace densities. Generally, by the growth of ultrathin film, we can overcome these issues as well as we can expect the possibility of new electronic and magnetic properties of the film due to confinement in a thin layer. Thus, it is interesting to study the growth, electronic structure, and magnetism of the CoO ultrathin film. Magnetic oxides (MO; M = Ni, Co, Fe, Mn) in the rock-salt structure are well-known antiferromagnetic insulators and the antiferromagnetic superexchange mechanism occurs through the M-O-M network. The bulk antiferromagnetic properties of TM oxides were studied using magnetic neutron diffraction, X-ray magnetic scattering, different magnetometries such as SQUID, VSM and other X-ray spectroscopies such as X-ray absorption/emission spectroscopies *etc.* by several groups of researchers [18, 160–163]. However, there are very few techniques such as spin-polarized scanning tunneling microscopy (SP-STM), X-ray magnetic linear dichroism-photoemission electron microscopy (XMLD-PEEM) *etc.* [20–22] available to probe the antiferromagnetism of these oxides in the ultrathin film regime. Recently, Batanouny *et al.* [164] have used metastable helium ion scattering techniques to the NiO(001) and CoO(001) surface to find out the surface antiferromagnetic structure. Long time back, Palmberg *et al.* [23] had first used LEED as a technique to detect surface antiferromagnetism of NiO(100). They have observed half-order spot with a (2×1) translation symmetry produced by exchange scattered low energy electrons below the Néel temperature ensuring the presence of antiferromagnetic ordering at the surface of the crystal. They have also mentioned, as the exchange interaction is much smaller than the Coulomb interactions, the intensity of these spots will be very small (2-6% of the integer spot). In recent times, our group is using this technique extensively for different antiferromagnetic systems like NiO thin films [22, 24], flat monolayer Cr film [25, 26, 142], *etc.* as a probe of surface antiferromagnetism. It is not only a new technique for probing antiferromagnetic structure but also the most direct means for studying the role of exchange in electron scattering. The half-order magnetic spots are detectable even in the ultrathin submonolayer regime as LEED is a surface sensitive technique. The intensities of the half-order magnetic spots produced by the interaction of the incident beam with the spin system are dependent on the spin ordering of the film. The measurement of the temperature dependence of the magnetic spot intensities will give rise to the various information about the surface spin ordering, in-plane and out-of-plane exchange parameters [27] as well as the Néel temperature of the surface/ultrathin films [26, 27]. Near the critical temperature (T_C), by fitting the experimental temperature dependence of the square root of half-order intensity variation data with the universal power law of the sublattice magnetization, $M_S(T) \sim (1-T/T_C)^\beta$ gives information about the critical exponent of the magnetization (β) [28]. Although there are many physical and technological importance of CoO thin films, only a few studies [69, 165–167] emphasized on the surface magnetism and the coverage dependent evolution of magnetic properties. Evidence of short-range magnetic ordering above the Néel temperature is controversially described in the literature [18, 56, 168]. We probe the surface antiferromagnetic ordering of the ultrathin CoO(001) film using LEED and it is probably the first experimental report, where we observed the evidence of antiferromagnetism in the ultrathin film (down to 0.2 ML) region. Evolution of the surface antiferromagnetic Néel temperature is studied with film coverage as well as with different substrates. In our experiment, the observation of higher Néel temperature relative to its bulk value even in the case of 2 ML CoO on Ag(001) cannot be explained by considering only the superexchange interactions, even though the bulk antiferromagnetism is well understood in terms of the superexchange interactions. We have introduced image charge screening effects [29] along with the superexchange interaction and finite size effects to explain the observed Néel temperature variation.

5.2 Coverage dependence of core level electronic structure

Evolution of core level electronic structure with film coverage has been investigated in this section. Fig. 5.1(a)-(c) shows the XPS core level spectra of Co 2*p*, O 1*s* and Ag 3*d*, respectively. In Fig. 5.1(a), we show the Co 2*p* core level spectra for different film coverage of CoO(001) grown on Ag(001). The Co 2*p* main peaks and their shake-up satellites are almost in the same binding energy for all the film coverages.

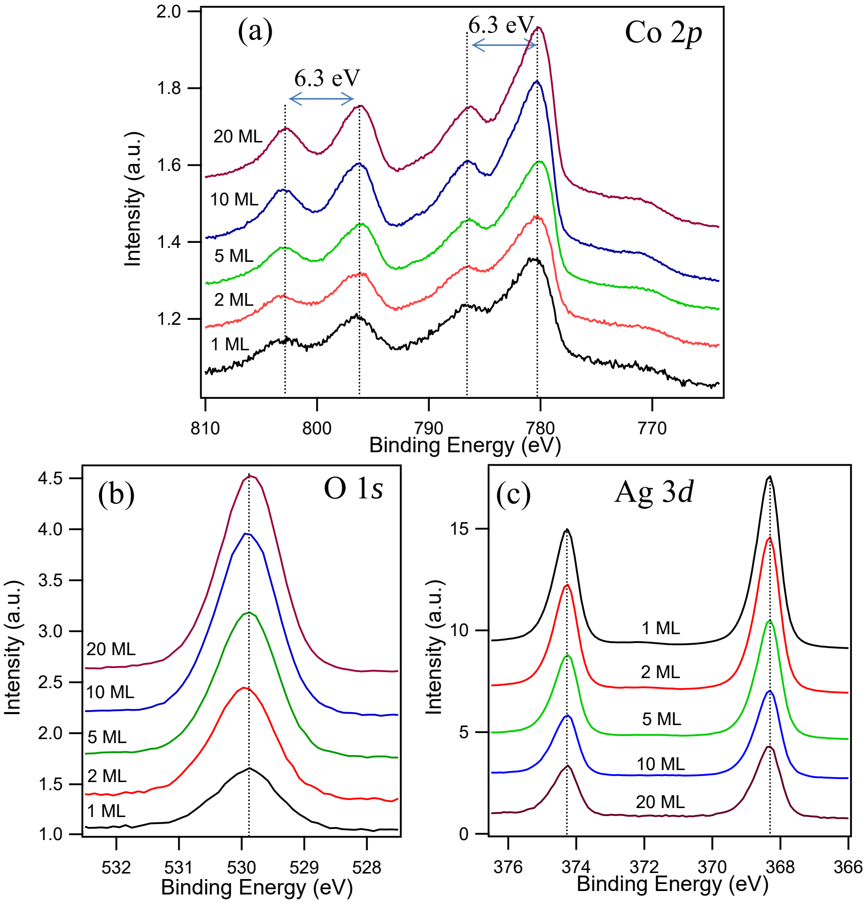

Figure 5.1: (a) Co $2p$ core level of CoO film for various film coverage. The satellite peaks were observed at 6.3 eV higher binding energy than the main peaks of Co $2p$. (b) O $1s$ core level for different film coverage. (c) Ag $3d$ for different film coverage.

However, there is a significant difference in the spectral features for the low coverage (1-2 ML) films. The presence of relatively low intense shake-up satellites is due to the less number of nearest neighbours in the reduced dimension. The satellites are prominently visible from 5 ML onwards about 6.3 eV higher binding energies with respect to the main peaks which is close to the reported single crystal value [56]. Due to the significant admixture of oxygen orbitals, Co $2p$ core level photoexcitation has both $2p^5 3d^7$ and $2p^5 3d^8 \underline{\mathrm{L}}$ final states where $\underline{\mathrm{L}}$ represents a hole in the O $2p$ band. The lower binding energy Co $2p_{3/2,1/2}$ peaks are associated with $2p^5 3d^8 \underline{\mathrm{L}}$ state and the higher binding energy charge transfer shake-up satellites with the $2p^5 3d^7$ state.

The O 1s peak was observed about 529.9 eV almost for all the film coverage as shown in Fig. 5.1(b). However, it is well-known from the previous studies that the lattice O 1s binding energy position for transition metal monoxides is relatively insensitive to changes in near-surface stoichiometry [169]. The intensity of Ag 3d peak [see Fig. 5.1(c)] decreases with the increasing film coverage, while the intensity of Co 2p and O 1s increases progressively with increasing film coverage, is consistent with the quasi-2D growth as investigated earlier using the surface sensitivity of the Tamm surface state of Ag(001) in chapter 3. With increasing CoO film coverage, Ag 3d peak does not shift in energy position indicating that there is no alloying between Co and Ag at the interface.

5.3 Valence band structure of CoO/Ag(001)

5.3.1 Earlier works

There are many theories developed to explain the insulating nature of CoO as the single band theory cannot explain it completely. The exact origin, nature, and size of the insulating gap of CoO have been a subject of debate since last few decades, among the researchers [55,170,171]. Despite its successes, density functional theory (DFT) in the framework of local density approximation (LDA) and the generalized gradient approximation (GGA) is inapplicable to the strongly correlated system like CoO. DFT predicts that CoO to be antiferromagnetic but metallic. The inappropriate treatment of exchange interaction in these approximations leads to this incorrect prediction. The screened exchange local density approximation (sX-LDA) can successfully predict the electronic properties of CoO with overall similar or greater accuracy than the other hybrid functional theories. In a local spin density treatment of exchange and correlation, the long-range magnetic order in CoO is responsible for the gap as demonstrated by Terakura *et al.* [55] who found a metallic system for the paramagnetic phase. Although it has been generally thought that electron-electron correlation effects are of central importance in explaining the electronic structure of these materials, there has been controversy concerning not only the magnitude of the Coulomb interaction but, also more fundamentally, whether the insulating gap is of cation $3d \rightarrow$ cation $3d$ or of anion $2p \rightarrow$ cation $3d$ character [14, 172]. According to the relative amplitude of the four parameters namely, the d-d Mott-Hubbard repulsion (U), the ligand-metal charge transfer energy (Δ), the TM $3d$ bandwidth (w), and the ligand $2p$ bandwidth (W), the $3d$ TM compounds can be classified within a phase diagram, the Zaanen-Sawatzky-Allen, ZSA, diagram [52], where the charge transfer (CT) insulators, Mott-Hubbard insulators, and the metallic compounds are properly classified. In the ZSA diagram, CoO [16] and MnO [173] placed in the intermediate region between charge transfer ($\Delta <$ U) and Mott-Hubbard ($\Delta >$ U) insulators as the U and Δ charge fluctuation energies being close to each other. Calculations of the energy-band structure of rocksalt transition metal monoxides have been performed in the framework of two seemingly contradictory approaches: a one-electron energy band [153, 174] and a more localized electron picture including the configuration interactions (CI) between hybridized $3d$ and ligand orbitals [52]. Both approaches seem to provide results that are consistent with several experimental observations. Despite the success of one electron spin-polarized energy band calculations in describing the electronic structure of magnetic $3d$ metal monoxides [55], as a whole, they do not reproduce the band gap values and underestimate the values of local magnetic moments. Although the local spin density approximation (LSDA) reproduces the ground-state magnetic structure of NiO-MnO series, it predicts CoO and FeO to be metals, while they are the insulator with well-established correlation gaps. So, it is evident that one electron band theory is not suitable for strongly correlated materials. A fundamentally different view of the electronic structure of $3d$ TM monoxides based on highly localized electron behavior has been made by the cluster method initiated by several groups of researchers [16, 175–178]. For CoO, the CI cluster calculation by van Elp and co-workers [16] suggests that the CoO band gap is of an intermediate character, between Mott-Hubbard type and charge transfer type with the value of U and Δ are 5.3 eV and 5.5 eV (U$\sim$ Δ), respectively. Recently, the variational cluster approximation is applied to the calculation of the single-particle spectral function of the $3d$ TM oxides MnO, CoO, and NiO which are in good agreement with the available ARPES data [179]. Moreover, the indication of 'Coulomb generated' band structure claims that it would be a promising tool for the study of realistic models of strongly correlated systems. Despite the advancement of band structure calculation techniques, the controversy regarding the correlation between electronic structure and antiferromagnetic ordering of the insulating $3d$ TM oxides through the Néel temperature is still unresolved [55, 56, 168]. The spin-polarized band structure calculation [171] leads to an insulating gap of CoO in contrast to a standard band structure calculation. Terakura and co-workers [55] have mentioned that band structure is very sensitive to the magnetic order as it is related to the narrowing the insulating band gap of NiO. The band structure calculation based on coherent potential approximation [180] show that the insulating gap persists even in the complete disordering of the magnetic moments in MnO whereas the calculated gap closes for such disordered moments in NiO. The photoemission spectra were taken with different photon energies at antiferromagnetic (AFM) and paramagnetic (PM) phases of CoO were found to be identical as reported by Shen *et al.* [56]. This has been explained by the fact that even in the paramagnetic phase, local spin order still exists within certain domains such that they look like same as the antiferromagnetic phase when probed by photoemission spectroscopy as it is a spin insensitive local probe technique. The evidence of short-range magnetic order above T_N has been observed in photoelectron diffraction of Mn compounds [181, 182]. Recently, our ARPES study on MnO during PM to AFM transition reveals the valence band narrowing along with the widening of the energy gap by 0.2 eV [6]. However, the situation is different for CoO as there is no such gap opening upon PM to AFM transition though there is a magnetic backbending corresponds to the local magnetic order as reported by Shen *et al.* [56, 57]. On the contrary, a recent angle-resolved Auger-photoelectron coincidence spectroscopy (AR-APECS) study on CoO reveals the collapse of the short-range magnetic order above the Nèel temperature [168]. There are several theoretical studies available where the two-dimensional (2D) energy band dispersion for PM [183] and AF-II [184–186] phases of CoO are being investigated. The experimental energy-band mapping of CoO(001) surface is poorly studied in the literature. In this section, I have tried to address these issues. We have grown high-quality CoO(001) film on Ag(001) and performed ARPES measurements both in the PM and AF-II phase of CoO and found there is good agreement with the theoretically predicted density of states (DOS) by Nekrasov *et al.* [183]. We have observed good agreements of our 2D experimental band mapping to the theoretically calculated energy band dispersions as well.

5.3.2 ARPES studies: 20 ML CoO/Ag(001)

ARPES is a well-established experimental technique to study the bulk energy band dispersions for metal and semiconductors. However, the angle-resolved studies on strongly correlated transition metal oxides are quite challenging due to its broad and complex valence band dispersions, especially in the insulating single crystal surfaces. We have undertaken a detailed band structure mapping of CoO films of various coverages starting from monolayer to the bulk-like 20 ML CoO towards two different crystallographic symmetry directions. The symmetry directions of fcc bulk Brillouin zone (BBZ) and the corresponding surface Brillouin zone (SBZ) are shown in Fig. 5.2. The surface crystallographic symmetry directions were determined from the LEED image of CoO(001) surface and hence the corresponding symmetry directions of bulk CoO can also be obtained from the Fig. 5.2. Fig. 5.3(a) and (b) show the valence band structure of 20 ML CoO film along $\bar{\Gamma}$-$\bar{X}$ direction of the CoO(001) SBZ

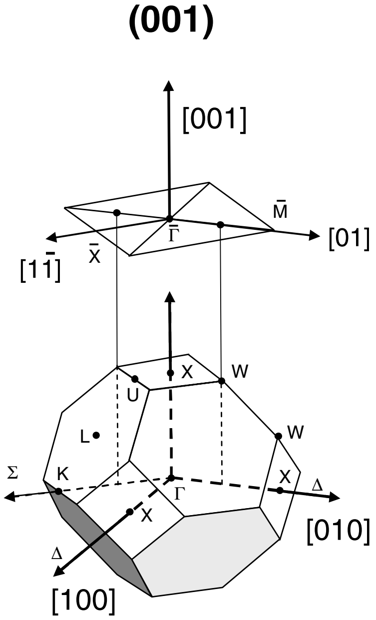

Figure 5.2: Surface Brillouin Zone (SBZ) of the fcc(001) crystal plane projected from the fcc Bulk Brillouin Zone (BBZ). The figure is taken from the Ref. [187].

using He I$_{\alpha}$ ($\hbar\nu = 21.2$ eV) and, He II$_{\alpha}$ ($\hbar\nu = 40.8$ eV) photon energies, respectively. The corresponding second derivative images helped us to clearly identify the band dispersion curves as shown in Fig. 5.3(d) and (e). The band dispersion along $\bar{\Gamma}$-$\bar{M}$ direction of the CoO(001) SBZ and the corresponding second derivative are shown in Fig. 5.3(c) and (f), respectively. The ARPES data of 20 ML CoO on Ag(001) is expected to be bulk-like due to the limited mean free path of photoelectrons. Moreover, it is also consistent with the fact that the finite-size effects will be minimal and will be more like the surface of the bulk CoO. Fig. 5.4(a) shows the theoretical band structure of bulk CoO along [001] direction [183]. By varying the parallel momentum (K$_{||}$) along the $\bar{\Gamma}$-$\bar{M}$ direction of the CoO(001) SBZ, we mapped out the electronic states along the Γ-Δ-X symmetry direction of the BBZ. Similarly, the $\bar{\Gamma}$-$\bar{X}$ direction in SBZ corresponds to the Γ-Λ-L direction in BBZ of CoO [see Fig. 5.2]. The O 2p band dispersion within -4 to -7 eV binding energy along $\bar{\Gamma}$-$\bar{X}$ direction [Fig. 5.3(d)] is matching well with the theoretical band dispersion along

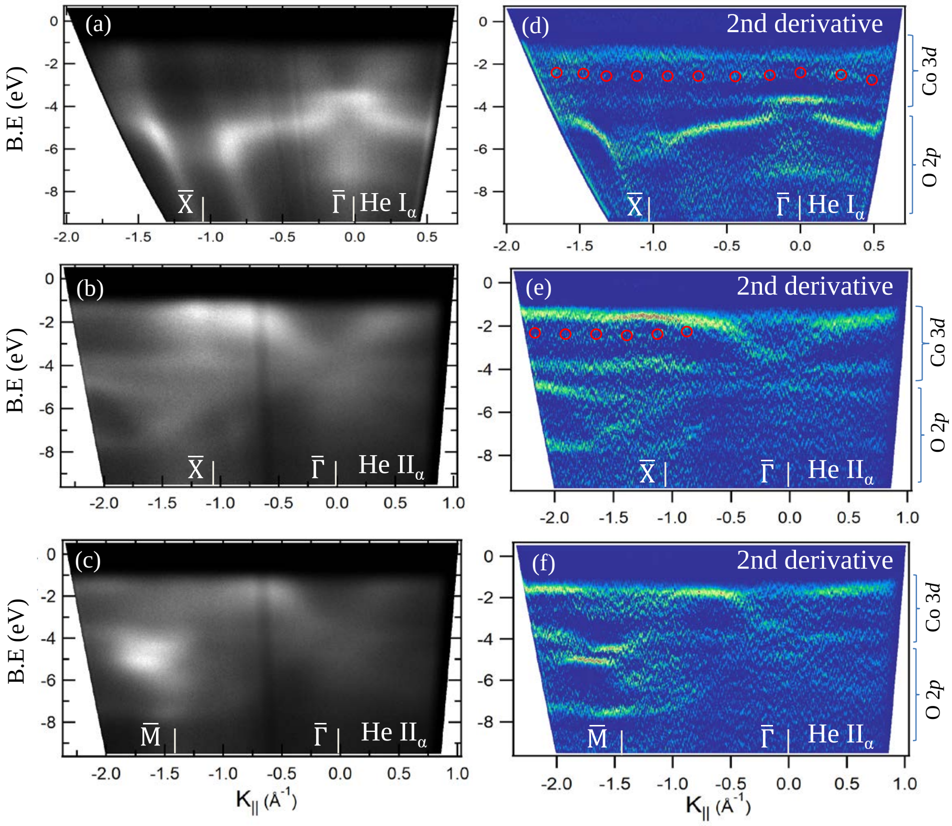

Figure 5.3: (a)-(b) ARPES data for 20 ML CoO/Ag(001) along $\bar{\Gamma}$-$\bar{X}$ direction of the CoO(001) SBZ using He I$_\alpha$, He II$_\alpha$ and (c) along $\bar{\Gamma}$-$\bar{M}$ direction using He II$_\alpha$. (d)-(f) are the 2nd derivatives of (a)-(c), respectively. The weakly intense bands are traced by the red circles to guide the eyes in (d) and (e).

Γ-L direction [Fig. 5.4(a)]. Similarly, the Co 3d band at -1.8 eV with a strong dispersion about Γ [Fig. 5.3(e)] is also consistent with the weak intensity calculated band dispersion. The O 2p derived bands along $\bar{\Gamma}$-$\bar{M}$ direction [see Fig.5.3(f)] are weak and difficult to compare with the calculated band structure [Fig. 5.4(a)] of bulk CoO along Γ-X direction. Despite these matching, there are also a few bands in our ARPES data which are absent in the calculated band structure and vice versa possibly due to the reduced photoemission cross sections of these energy bands for the used photon energies. Further, the calculated surface band structure (blue lines) with the projected bulk band structure (gray shaded areas) of CoO(001) is

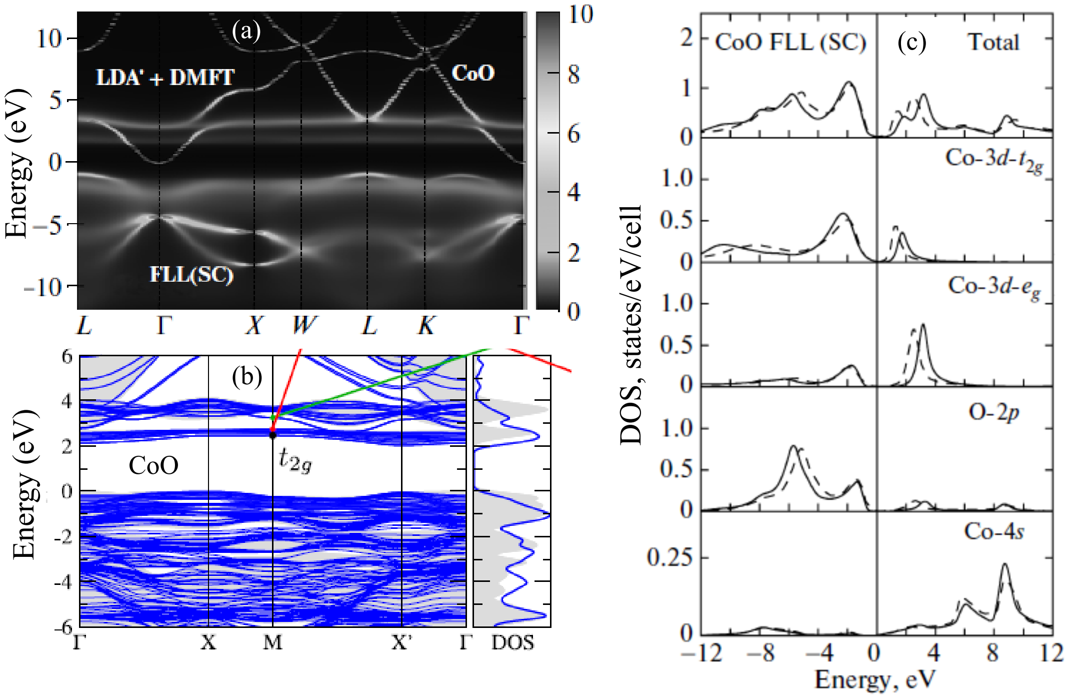

Figure 5.4: (a) Calculated bulk band structure of paramagnetic CoO using LDA′+DMFT. (c) The partial and total density of states (DOS) for CoO(001). The data are taken from Nekrasov *et al.* [183]. (b) Calculated surface band structures of the antiferromagnetic CoO(001) using DFT+U, data is taken from Schrön *et al.* [188].

taken from the Ref. [188] [Fig. 5.4(b)] for direct comparison with our ARPES data. The band dispersion about -1.8 and -3.5 eV matches well with the projected bulk band structure (gray shaded areas) along $\bar{\Gamma}$-$\bar{X}$ direction [Fig. 5.4(b)]. However, the complete description of surface band structure requires an exact slab calculation as each CoO(001) layers are contributing separately in the surface band structure. The calculated density of states (DOS) [183] show the lower Hubbard band which consists of respective Co-3d t_{2g} and e_g contributions at -2.5 eV and -1.8 eV, respectively [see Fig. 5.4(c)]. The O 2p states are located between -4 eV to -9 eV which has been observed in our experimental band dispersion as well. The O 2p states at -1.5 eV together with Co-3d e_g states form the so-called Zhang-Race band. This is a bound state that appears when a strongly interacting band is hybridized with the charge reservoir. If we look at the experimental band dispersion, the low intense band at -2.5 eV is almost non-dispersive [traced by red circles in Fig. 5.3(d) and (e)], however, the band at -1.8 eV has a significant dispersion at $\bar{\Gamma}$ point. Another Co-3d t_{2g} derived band at -3.8 eV [see Fig. 5.3(e)] is absent in the calculated 2D band structure [183]. The valence band XPS study by K.S. Kim [189] reveals the presence of a state at -3.8 eV which may be the same feature as observed in our ARPES results. Previous studies [190] suggested that CoO exhibit a gap between t_{2g} and e_g states which is about 1-1.5 eV whereas our experimental data shows relative dispersion between t_{2g} and e_g varies within $\sim$ 0.7-2.2 eV [Fig. 5.3(d) and (e)]. This dispersion was observed due to the hybridization between Co 3d e_g and O 2p, as O 2p is well dispersed. Further, the dependency of photoemission cross-section on the band intensities is clearly visible from our experimental band dispersion shown in Fig. 5.3 as the O 2p bands are distinctly visible when probed by He I_α while Co 3d bands are clearly visible with the He II_α photon energy. The overall band dispersions about Γ point of SBZ for both He I_α and He II_α photon energies are in good agreement with the theoretically predicted band dispersion.

5.3.3 ARPES: Coverage dependence

The valence band electronic structure of CoO film with different coverages on Ag(001) are shown in Fig. 5.5, where He II_α was used as excitation energy. For better visualization of dispersive features of the bands, corresponding second derivative ARPES data are presented in Fig. 5.6. The *sp* band of Ag(001) has lower intensity relative to the d bands which enable the Co 3d bands to be easily detectable from the very initial stages of CoO film growth. However, the O 2p bands are not clearly distinguishable before 5 ML coverage due to the overlapping with high-intensity Ag 4d bands. From 5 ML onwards, the contribution of buried Ag decreases and mostly the CoO(001) bands are visible. In case of 1 ML CoO, the maximum of the

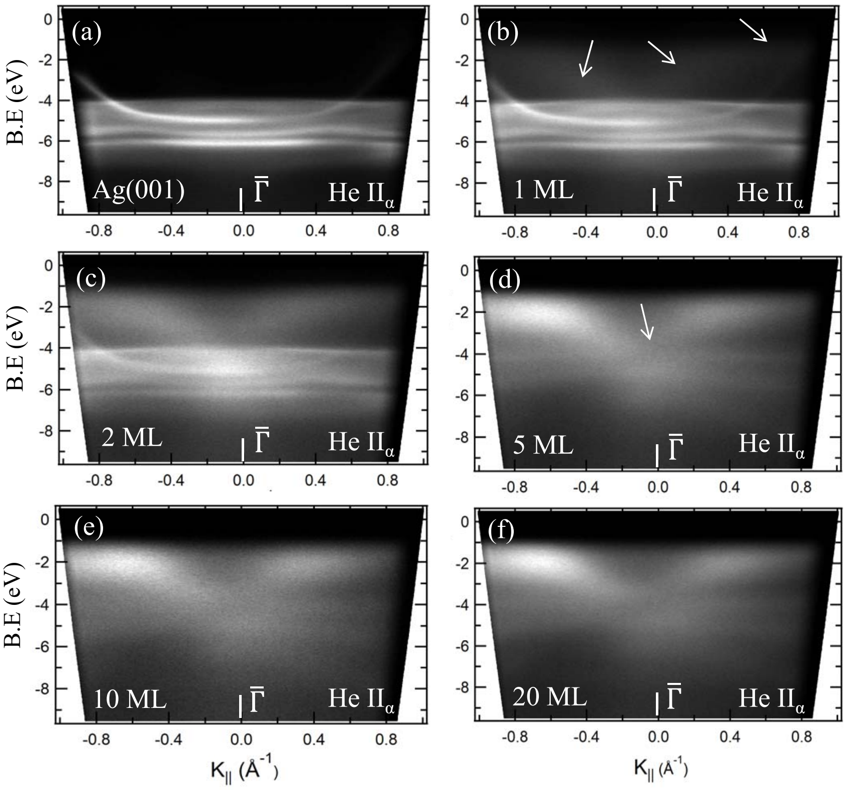

Figure 5.5: Coverage dependent ARPES data around $\overline{\Gamma}$ point using He II$_\alpha$ as an excitation energy. All the data are taken at RT.

valence band is located at -1.1 eV [see Fig. 5.6(b)] and with increasing coverage, this feature disappears from 5 ML onwards. So, it is indicative that with increasing film coverage, the film is getting more insulating as the density of states decreases near the Fermi level. At 1 ML coverage, two almost non-dispersive band appears at -1.8 eV and -3 eV, with increasing coverage a relative dispersion has been observed about $\overline{\Gamma}$ point [see Fig. 5.6(b)-(d)]. Upon increasing coverage, the band at -1.8 eV remains almost non-dispersive, however, the band at -3 eV disappears and a highly dispersive band [see Fig. 5.6(d)] evolves from 5 ML onwards. The relative dispersion results in a gap of $\sim$ 1.6 eV between these two bands at $\overline{\Gamma}$ point. From 5 ML coverage onwards, almost non-dispersive O $2p$ bands are weakly visible within -4 eV to -7 eV binding energy about the $\overline{\Gamma}$ point [see Fig. 5.6(d)-(f)]. In the low coverage (1-2 ML),

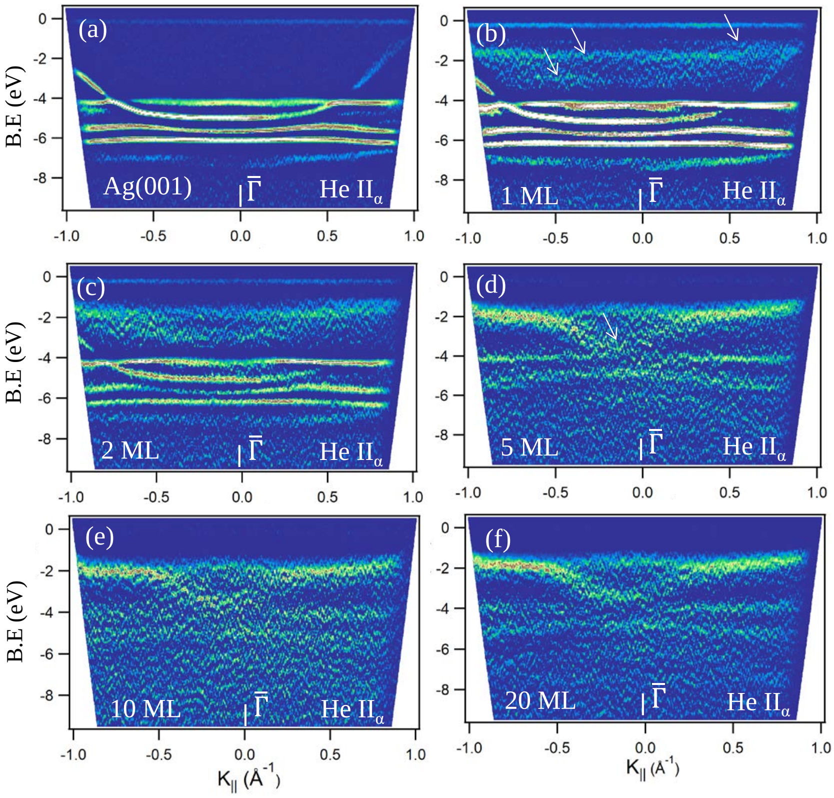

Figure 5.6: The 2nd derivative of ARPES data around $\overline{\Gamma}$ point using He II$_\alpha$ for the different coverages of CoO(001) films taken at RT. The 2nd derivatives of the ARPES band dispersions were obtained following Zhang *et al.* [148].

the band/states that appear at -1.1 eV and -3 eV and disappears upon increasing coverage. These states arise due to the interfacial effects which have been already discussed in Chapter 3. From 5 ML onwards, the ARPES band dispersions are quite similar to the previously discussed bulk CoO band structure [183].

5.4 Surface antiferromagnetism of CoO/Ag(001)

The bulk CoO has rock-salt structure with a lattice parameter of 4.26 Å is a well-studied antiferromagnet with a Néel temperature (T$_N$) of 291 K [191]. The bulk antiferromagnetic properties of CoO were studied using magnetic neutron diffraction, X-ray absorption spectroscopy(XAS), magnetic X-ray dichroism (MXD) by several groups of researchers [17, 18, 162, 192, 193]. However, there are very few reports available on the surface antiferromagnetism of CoO in reduced dimension [165, 167, 168]. Palmberg *et al.* [23] first observed the antiferromagnetism of NiO single crystal by exchange scattering in low energy electron diffraction experiment. The appearance of additional magnetic half-order spots below the Néel temperature due to the exchange scattering of the incoming electron to the atomic electron ensures the presence of antiferromagnetic ordering on the crystal surfaces. It was not only a new method for probing the magnetic structure but also the most direct means for studying the role of exchange in electron scattering. The half-integer magnetic spots are detectable even in the ultrathin submonolayer regime as the low energy electron diffraction is a surface sensitive technique. The intensities of the half-ordered magnetic spots produced by the interaction of the incident beam with the spin system are dependent on the spin ordering of the film. The measurement of the temperature dependence of the magnetic spot intensities will provide information on the surface spin dynamics of the system. This is the first report on the investigation of surface antiferromagnetism of CoO(001) film by means of exchange scattered half-ordered LEED spots to the best of our knowledge. The dependence of the antiferromagnetic ordering temperature (T_N) of CoO on the film coverage is investigated using the temperature dependence of the half-order spot intensities. Upon cooling down the well-ordered p(1×1) CoO(001) film keeping under LEED, there appear few extra spots midway position between the (0,0) spot and p(1×1) spots and these spots are only visible in the low electron beam energy(15 -40 eV). These spots are known as half-order spots and usually defined as a p(2×1) twin-domain structure, similar to the NiO [23] and MnO [6]. Fig. 5.7(a) shows the LEED image of clean Ag(001) surface at 22 eV beam energy. We do not observe any spot in the LEED screen as the first order diffraction spots are out of the field-of-view due to the low energy of electron beam. Upon deposition of 0.5 ML CoO, the half-order spots appear below a certain temperature [see Fig. 5.7(b)]. The evolution of half-order spot intensity

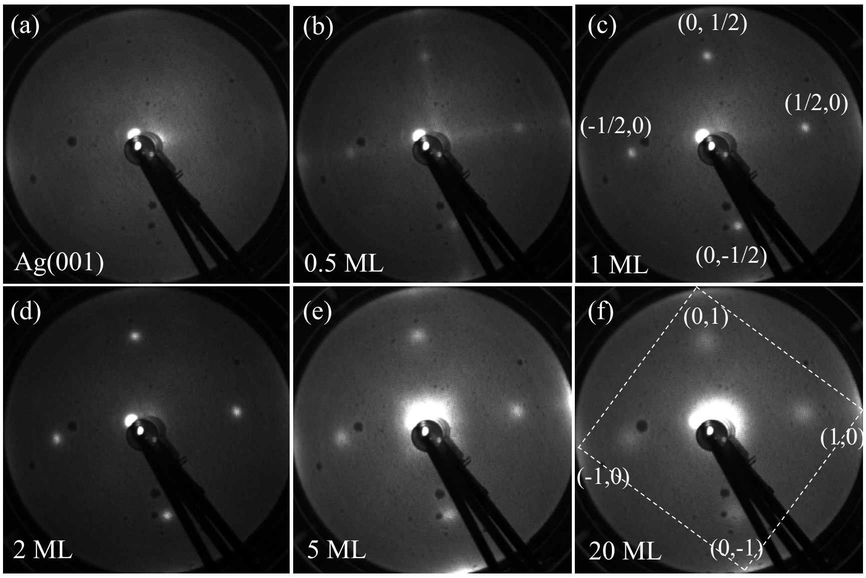

Figure 5.7: LEED images for different film coverages, taken at 22 eV electron beam energy and at 150 K (a) Clean Ag(001) substrate (b) 0.5 ML CoO (c) 1 ML CoO (d) 2 ML CoO (e) 5 ML CoO (f) 20 ML CoO. The half-order spot positions [in (c)] and the p(1×1) unit cell shown by the dotted line square [in (f)]. The integer order spots are outside the field-of-view of the LEED screen, while the tails of the peaks can be observed as marked and indexed as in (f).

with film coverage at 150 K are shown in Fig. 5.7(b)-(f). All the LEED images were taken at 22 eV electron beam energy to get the maximum intensity of these exchange scattered spots. We have observed these spots starting from submonolayer (0.5 ML) to almost bulk [20 ML] film coverage. The intensity of the half-order spots enhanced with increasing film coverage up to 2 ML, beyond this coverage the spots became broad and diffused. The intensity of these half-order spots are related to the surface magnetic ordering and as the coverage increases, the surface structural quality as well as the magnetic ordering deteriorates. The appearance of the half-order spots can be explained by the magnetic unit cell structure of CoO, similar to the case of NiO [23]. Schematic diagram of the CoO magnetic unit cell is shown in the Fig. 5.8(a), where we have only shown the spin arrangement of Co^{2+} ions in the CoO unit cell. The moment of each Co^{2+} ions are aligned in a way such that the

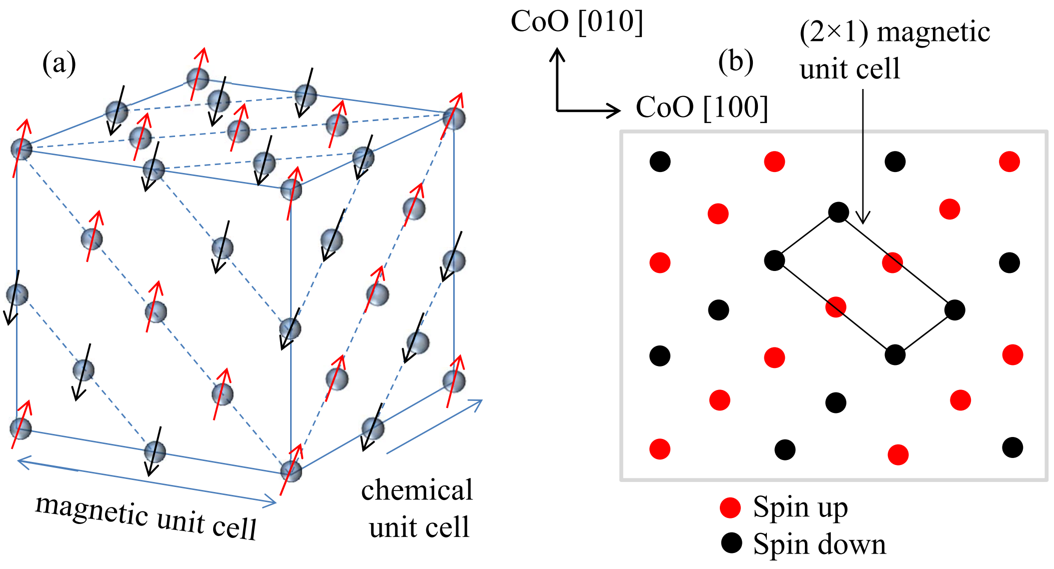

Figure 5.8: Schematic diagram of the spin arrangements of Co^{2+} ions in CoO. The O^{2-} ions are not shown here. In each (111) planes, magnetic moments are ferromagnetically aligned parallel to the plane and the consecutive (111) planes are antiferromagnetically aligned. The red and black arrow represents the spin directions between two consecutive (111) planes. (b) The real space spin arrangements of Co^{2+} ions in the CoO(001) surface. Here the red and black dots represent the spin up and spin down Co^{2+} ions, respectively. The rectangle in (b) represents the (2 ×1) magnetic unit cell. The figures are adopted from the Ref. [23] and redrawn.

spin arrangement of each (111) plane are parallel within the plane and antiparallel between the adjacent planes. The red and black arrow indicates the spin directions of two adjacent (111) ferromagnetic sheet aligned antiferromagnetically. The real space spin arrangement of CoO (001) plane is shown in Fig. 5.8(b) which has a p(2×1) translational symmetry relative to the chemical unit cell. Thus, the p(2×1) magnetic unit cell will give rise to a p(2×1) magnetic twin domain pattern in the LEED image. Due to the square symmetry of the CoO(001) surface, twin domains appear in LEED at the right angle to each other. The origin of this type of twin domains (half-order) can be either magnetic or structural. If the appearance of these spots is due to structural origin, then one can expect the intensity of these spots should

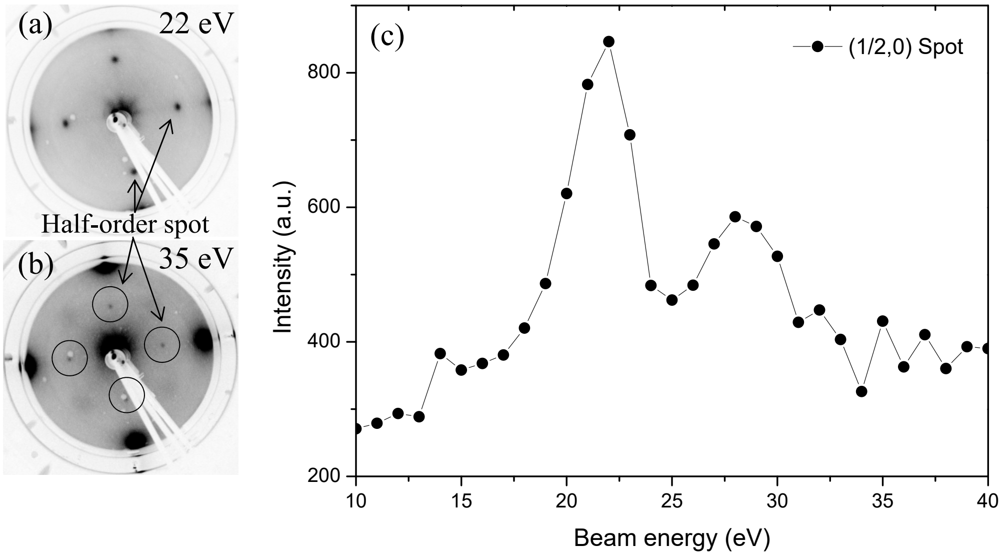

Figure 5.9: Half-order spot of 2 ML CoO taken at 150 K with (a) 22 eV and (b) 35 eV beam energy. (c) The intensity variation of the half-order spot with incident electron beam energy. At 22 eV incident beam energy, the half-order spot shows maximum intensity.

be comparable with the integer order spots and the intensity should not change significantly with temperature apart from the thermal effects given by Debye-Waller factor [194]. But our experimental findings rule out the possibility of structural origin as the spots disappear when the temperature of the film is raised above the critical temperature and reappeared on cooling below the critical temperature. For the incident beam energy range of 15-40 eV and well below the critical temperature, the intensity of the half-order spot was 2-3% of the integer spot intensity which is similar to the cases of NiO [23] and MnO [6]. Moreover, the intensity variation curve (I-V) of the half-ordered spots with incident electron beam energy persists only below 45 eV [see Fig. 5.9(c)] as the cross-section of exchange scattering decreases with increasing electron beam energy [23]. The weak intensity of the half-order spots resulting in a poor statistics for the measured I-V curve shown in Fig. 5.9(c). The intensity of the half-order spot is maximum at 22 eV beam energy [see Fig. 5.9(a)] and decreases with increasing electron beam energy [see Fig. 5.9(b)]. It is clear from the Fig. 5.9(c) that the maximum spot intensity is observed at 22 eV beam energy with a secondary maxima at 28 eV. So the visibility of these spots only in the lower energy range (<45 eV) having low intensity (2-3%) in comparison with the integer order spots with the typical temperature dependence of the spot intensity confirms their antiferromagnetic origin.

The temperature dependent intensity profile of the exchanged scattered magnetic half-order spots has been used to study the antiferromagnetic properties of the film. In order to estimate the antiferromagnetic ordering temperature of CoO, the variation of background subtracted half-order spot intensity with temperature has been plotted for the different film coverage of CoO [see Fig. 5.10(a)]. The ordering temperature has been estimated from the discontinuity of the slope of the polynomial fitted curve [see Fig. 5.10(b)] [195]. Since the nature of the temperature dependence curves of all the four half-order spots $(0, \pm\frac{1}{2})$, $(\pm\frac{1}{2}, 0)$ are identical, one can use any one of it to

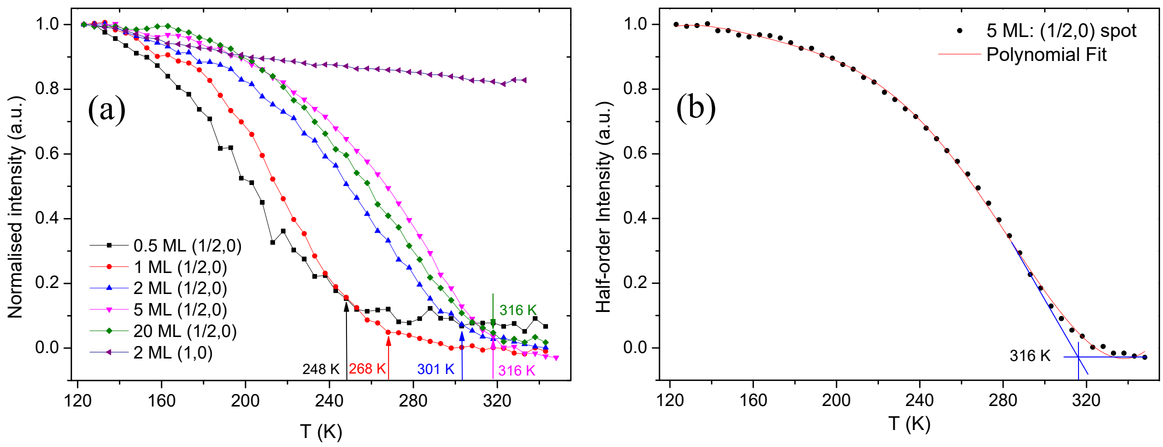

Figure 5.10: (a) The background subtracted half-order $(\frac{1}{2}, 0)$ LEED spot intensity variation with film coverage. The integer order (1,0) spot intensity variation is also shown to discriminate the origin of half-integer order and integer order spots. The surface Nèel temperatures for different film coverages are shown by arrows. (b) The surface Nèel temperature was estimated from the half-order intensity versus temperature curve. The point of discontinuity of the slope of the polynomial fitted curve has been taken as surface Nèel temperature.

elucidate the antiferromagnetism of CoO. In order to distinguish the origin of integer and half-integer order spots, we have plotted integer order spot (1,0) intensity along with the $(\frac{1}{2}, 0)$ spot intensities with temperature. Half-order spot intensities decrease with increasing temperature and eventually vanishes above the ordering temperature while the (1,0) spot intensity does not change significantly. A small decrease in the intensity of the (1,0) spot was observed due to the thermally scattered electrons in the higher temperature range [Debye-Waller factor]. The antiferromagnetic surface ordering temperature increases with increasing film coverage and saturated after 5 ML coverage [Fig. 5.11(b)]. We observe that the surface ordering temperature is saturated at 316 K for 20 ML CoO film which is about 25 K higher than the bulk antiferromagnetic Néel temperature [291 K]. Antiferromagnetism of bulk CoO is well understood in terms of superexchange interaction between Co 3*d* and O 2*p*. Néel temperature depends on the Co 3*d*-O 2*p* hybridization. But the observed effects in our experiment, cannot be explained solely by superexchange interaction. In order to explain our observation one has to incorporate the finite size effect, the in-plane lattice strain along with image charge screening effects due to the highly polarizable Ag(001) substrate as well. As Ag has ∼4% smaller lattice parameter than CoO, the film is subjected to in-plane compressive stress which results in the increase of Co 3*d*-O 2*p* hybridization due to the enhanced overlap between these orbitals from the reduced lattice parameter. This enhanced hybridization strengthens the Co 3*d*-O 2*p* superexchange interaction and as a consequence the Néel temperature increases. But as the film coverage increases, the surface strain relaxes [see Fig. 5.11(a)] and the superexchange strength decreases which leads to a lowering in Néel temperature. However, our experimental results show just the opposite effect [see Fig. 5.11(b)], where the T_N increases with the film coverage and finally saturates. This increase in T_N can be explained by the combined effect of the interfacial lattice strain and the change of surface coordination number with film coverage. Although, the superexchange interaction enhanced due to the in-plane compressive lattice

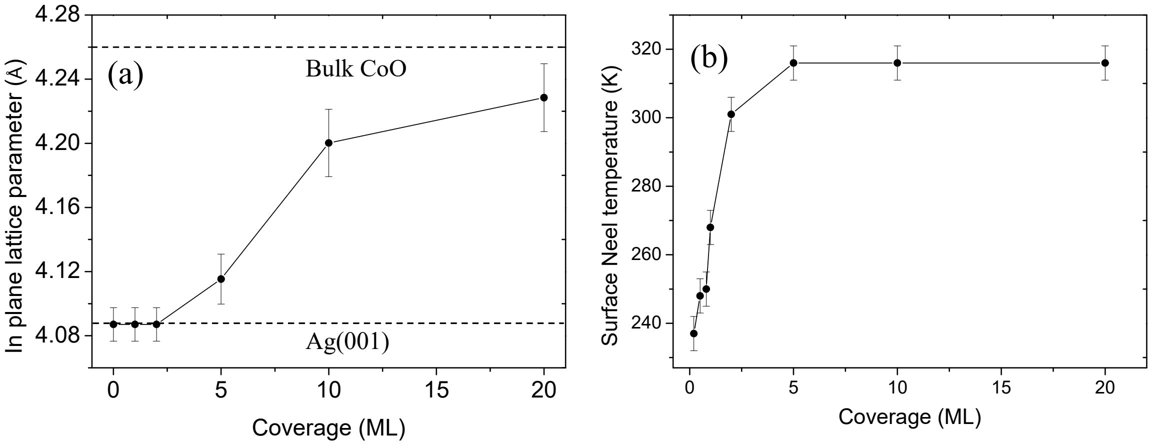

Figure 5.11: (a) The variation of in-plane lattice parameter is shown as a function of film coverage. The lattice parameters of bare Ag(001) and bulk CoO are also shown by the dotted lines as references. (b) The evolution of surface Nèel temperature with film coverage.

strain it again reduces due to the least number of nearest neighbors (finite size effects) in the lower film coverage regime. After the initial pseudomorphic growth, gradual strain relaxations is started from 2 ML onwards and reaches close to the bulk CoO lattice parameter at 20 ML [see Fig. 5.11(a)]. However, if we look at the Néel temperature variation with film coverage [see Fig. 5.11(b)], it is already saturated at 5 ML, whereas the strain is just started to relax. After 5 ML coverage, no changes in the Néel temperature were observed with further strain relaxations as the surface coordination number (finite size effects) is almost saturated which leads to the saturation of the Néel temperature. From the Fig. 5.11(b), it is clear that the Néel temperature of 20 ML is 316 K which is about 25 K higher than the bulk value (291 K) of CoO. Interestingly, even for 2 ML of CoO, T_N is higher than bulk value which can be explain by the enhancement of superexchange interaction due to the in-plane compressive strain. But for 20 ML film coverage, the enhancement of Néel temperature beyond the bulk T_N value, despite the near absence of strain effects and finite size effects is still a matter of discussion. This can be elucidate by taking into account of the image charge screening due to the proximity to the highly polarizable Ag(001) substrate [33]. According to Altieri *et al.* [29], in the close proximity of the strongly polarizable Ag(001), the superexchange interaction of CoO and the corresponding antiferromagnetic ordering temperature can be substantially amplified by reducing the energies of underlying virtual charge excitations as a result of image charge screening. The effects of underlying substrate on Néel temperature were further studied using less polarizable MgO as substrate. In the next chapter, I will discuss about these aspects of the CoO film grown on MgO film supported by Ag(001) substrate.

5.4.1 Antiferromagnetism vs. Paramagnetism: Band structure perspective

In this section, I will discuss how the valence electronic structure modified upon the change of magnetic ordering of the CoO(001) film. From LEED study, we have already shown that long-range magnetic order exhibits half-order spots in antiferromagnetic phase below the surface Nèel temperature of CoO(001). Fig 5.12(a)-(b), shows explicitly the appearance of magnetic half-order spots at 123 K which disappears upon annealing above the Nèel temperature. Now it is interesting to explore how the surface electronic structure modifies through this antiferromagnetic (AFM) to paramagnetic (PM) transition. Fig. 5.12(c) shows the valence band electronic structure of 5 ML CoO grown on Ag(001) for both the paramagnetic and antiferromagnetic phases. The different features are labeled by ‘a’, ‘b’, ‘c’, and ‘d’, respectively, which are controversially discussed in the literature. But calculations on the basis of ligand field theory combined with the model cluster approach [16] can explain the observed experimental features quite well. Photoemission ground state of Co^{2+} in CoO has $^4T_{1g}$ symmetry with an electronic configuration $[(t_{2g}\uparrow\uparrow\uparrow)(e_g\uparrow\uparrow)(t_{2g}\downarrow\downarrow)$. The first electron removal state of CoO is $^3T_{1g}$, an intermediate spin character. The interatomic

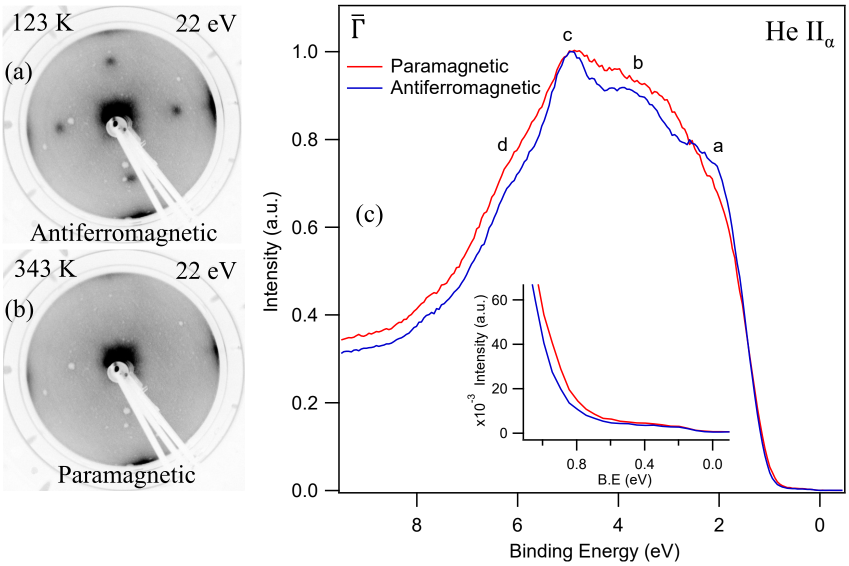

Figure 5.12: (a)-(b) LEED images at 22 eV beam energy for the antiferromagnetic and paramagnetic phases of CoO. (c) ARPES spectra of 5 ML CoO film at $\overline{\Gamma}$ using He II$_\alpha$ (40.8 eV) photon energy in PM and AFM phase. The enlarged view of the spectra near the Fermi level is shown in the inset.

transition of d electrons between two Co sites can involve the excitation of spin up e_g electrons into spin down t_{2g} states. Transition probability for such processes is expected to be weak at high primary energy, even if they are antiferromagnetically coupled. The transition of spin down electrons from t_{2g} states of a Co ion to the spin down empty t_{2g} states of adjacent Co ions resulting in the next ionization $^5T_{2g}$ state. The third ionization state is of $^3T_{2g}$ character. The first two ionization states have considerable $d^7\underline{\mathrm{L}}$ character [16]. The feature 'a' in Fig. 5.12(c) mainly corresponds to the $^5T_{2g}$ state, while other two relatively less intense states are observed within about 0.5 eV at higher ($^3T_{2g}$) and lower $^3T_{1g}$ binding energy. The feature 'a' associated with $^5T_{2g}$ state is more resolved with slightly higher intensity in AFM phase suggesting the t_{2g} band narrowing which is crucial for the insulating nature of CoO. The features 'b' and 'd' are the O $2p$ derived states consists of π emission about 4 eV and a σ contribution at 6.2 eV, respectively, are consistent with the reported data [100]. The feature ‘c’ appears mainly due to the Ag $4d$ band buried under 5 ML CoO with a contribution of O $2p$ bands. The band edge near Fermi level for AFM phase is slightly shifted towards higher binding energy than the PM phase as shown in the inset of Fig. 5.12(c). This is a clear indication that the AFM phase of CoO is more insulating relative to the PM phase, and in the AFM phase, $^5T_{2g}$ states is sharper than the PM phase. The observation of band narrowing and the sharper $^5T_{2g}$ state in the AFM phase is consistent with the theoretical prediction of Terakura *et al.* [55]. However, no major changes in the spectral features between AFM and PM phase were observed. The most probable reason could be the presence of short-range antiferromagnetic ordering in CoO even above the Nèel temperature as explained by Shen *et al.* [56]. The presence of short-range antiferromagnetic ordering above T_N in bulk CoO is already confirmed by neutron diffraction experiments [18, 196, 197]. We obtain an almost similar valence band electronic structure in both AFM and PM phase of CoO due to the existence of the short-range magnetic correlations whose length scales are larger than the photoemission correlation lengths. However, the LEED coherence lengths are much larger (few hundred Angstroms) and are able to detect the AFM to PM transitions as a function of temperature. Further studies are required to confirm this hypothesis as well as to understand the nature of these short-range correlations.

5.5 Summary

In summary, detailed coverage dependent study of the electronic structure of CoO(001) film on Ag(001) has been investigated using XPS and ARPES techniques. Coverage dependent valence electronic structure reveals the appearance of almost nondispersive band from the very initial CoO film coverage. As the coverage increases, a relative dispersion has been observed about the $\overline{\Gamma}$ point. At 20 ML coverage, the band dispersion is almost bulk-like and quite similar to the calculated bulk band structure. We have used LEED as a technique for probing surface antiferromagnetism of

CoO(001) film grown on Ag(001) and have shown that the antiferromagnetic ordering temperature can be estimated from the temperature dependence of the half-order magnetic LEED spot intensity. The half-order spots have been observed in LEED due to the low energy exchange-scattered electrons from CoO(001) surface with the periodicity of the CoO magnetic unit cell, for the first time from the CoO(001) surface. The presence of weak intensity exchange-scattered half-order spot below the critical temperature in the low electron beam energy (<40 eV) with a reversible temperature dependency of the half-order spots, confirms its antiferromagnetic origin. Variation of the surface Nèel temperature with film coverage has been discussed. The higher value of the observed surface Nèel temperature of CoO(001) than the bulk CoO Nèel temperature has also been discussed by means of image charge screening effect. The effect of antiferromagnetic ordering in the electronic structure has been illustrated using the ARPES spectra of CoO(001) for both AFM and PM phases. The observed band narrowing effects and the sharper $^5T_{2g}$ state in the AFM phase is consistent with the theoretical prediction. Though we do not observe a significant change in the valence band structure through the AFM to PM phase transition of CoO due to the existence of the short-range antiferromagnetic correlations even in the PM phase.

6

Surface antiferromagnetism of CoO/MgO(001)

6.1 Introduction

Magnetism of transition metal oxides is one of the central issues in condensed matter physics due to the spectacular magnetic and electrical properties making them promising for the field of nanoscience technology applications. The reduction of magnetic critical/ordering temperatures due to the finite size effects shrinks the field of applications of these materials. There are a few techniques available to overcome these issues such as the use of chemical doping, high pressure, and strain [66–68]. The reduction of magnetic transition temperature is well understood in terms of finite size scaling for ferromagnetic materials in low dimensions [62–64]. However, the observations of enhanced Nèel temperature of metal supported antiferromagnetic oxides in reduced dimensions cannot be explained only by considering the finite size effects [29, 65]. In order to explain this, the image charge screening has been introduced by Altieri *et al.* [29]. The insulating oxide materials in the close proximity to strongly polarizable medium results in the reduction of energies of the underlying virtual charge excitations [33, 34, 198]. As a consequence, the relevant exchange and superexchange interactions, and thus the related magnetic transition temperature can be substantially amplified. The exact dependence of charge excitations energies to the superexchange interaction can be found from the well-known extended Anderson expression of superexchange coupling constant J [52,60], $J = -\frac{2t^4}{\Delta^2}(\frac{1}{\Delta} + \frac{1}{U})$, where t is the anion $2p$-cation $3d$ transfer integral, Δ the $2p$-$3d$ charge transfer energy, and U is the on-site $3d$ Coulomb potential. So, the superexchange interaction J, and consequently T_N can be enhanced by increasing the transfer integral t and/or decreasing U and Δ. The image charge screening could result in a 50% reduction of U and Δ values for NiO on Ag [33]. This large screening causes a substantial enhancement of J and T_N in NiO/Ag. Moreover, the change in the on-site Coulomb (U) and charge transfer (Δ) energies of insulating oxides in close proximity to the polarizable medium can vary depending upon the dielectric polarizability of the medium. Thus, the enhancement of transition temperature can also be varied by the appropriate choice of polarizable medium up to some extent. Apart from the image charge screening, conventional methods like high pressure, compressive lattice strain can also reduce the interatomic spacing and thus lead to enhanced superexchange interactions and the T_N in many transition metal oxides [66–68]. However, the effects of modified superexchange transfer integral t on J and T_N in NiO/Ag and NiO/MgO films are negligible as shown by Altieri *et al.* [29].

In order to explore the concept of image charge screening, CoO film was grown on Ag(001) and MgO/Ag(001) and the corresponding Nèel temperatures were estimated using exchange scattered half-order LEED spots as described in the previous chapter. Enhancement of CoO/Ag(001) Nèel temperature over the bulk values has been explained by the underlying virtual charge excitations due to the image charge screening. In this chapter, I have introduced less polarizable MgO films of different coverage as a spacer layer between CoO and Ag(001). CoO films on Ag(001) and MgO(001) are ideal model systems to study this because CoO can grow epitaxially on both Ag(001) and MgO(001) due to the small lattice mismatch and they have well-characterized growth properties [199–203]. By introducing MgO as a substrate, lattice strain of CoO can reduce substantially as bulk CoO [4.26 Å] and MgO [4.21

Å] has smaller lattice misfit relative to the Ag(001) [4.08 Å]. However, it has been experimentally shown that for CoO film on MgO, uniaxial lattice strain up to 2% has negligible effects on T$_N$ [69]. This shows that T$_N$ enhancement based on the increase of superexchange transfer integral t is hardly affected by the substrate-induced strain.

6.2 Evolution of half-order spots: Film and substrate coverage dependence

Antiferromagnetism of CoO films on Ag(001) has been successfully described using exchange scattered low energy electrons (magnetic half-order LEED spots) in the previous chapter. Coverage dependent magnetic properties of these films were also studied using LEED and photoemission techniques. However, the effects of underlying substrate on the magnetic properties are yet to be explored. Different coverages of

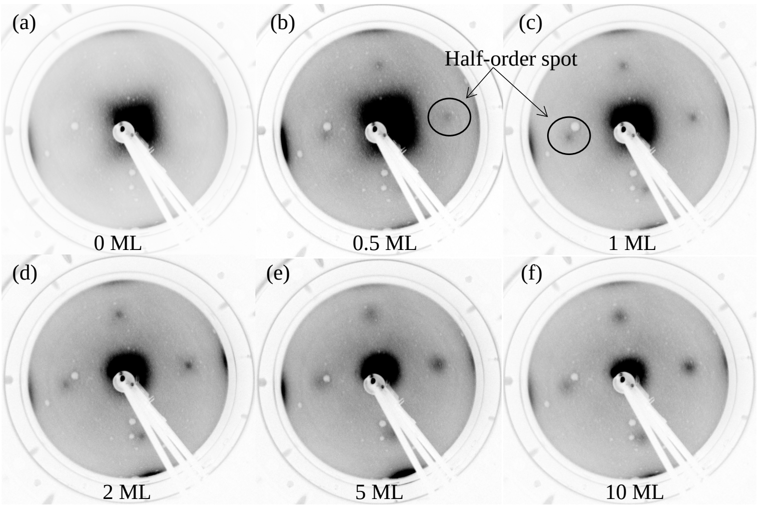

Figure 6.1: Coverage dependent evolution of half-order LEED spots of CoO on 10 ML MgO/Ag(001). All the images were collected at 22 eV beam energy and at 123 K.

MgO layers were grown on Ag(001) to investigate the substrate induced magnetic properties of CoO films. Growth details and characterization of MgO films are already discussed in chapter 4. Fig. 6.1 show the LEED images of different CoO film coverages grown on 10 ML MgO/Ag(001). All the images are taken at 22 eV primary electron beam energy and at 123 K, well below the Nèel temperature of the films. It is interesting to note that half-order spots are visible even at submonolayer regime (0.5 ML) and the intensity of these spots increases with film coverage. However, the spots get broader for the higher film coverages due to the reduced surface crystalline quality. In order to investigate the evolution of the half-order LEED spots as a function of substrate coverage, experiments were performed for 2 ML CoO film with varying the coverage of the underlying MgO layers. This is because 2 ML CoO has the maximum half-order intensity. Fig. 6.2 shows the half-order spots of 2 ML CoO grown on Ag(001) and three different MgO substrates. The most intense, well-ordered spots were observed on Ag(001) and as the MgO spacer layer coverage increases, the quality of the half-order spot degrades. CoO grows pseudomorphically on Ag(001) in the initial stages, however, upon insertion of MgO layers, the film relaxes by the formation of dislocations network after a certain coverage as discussed previously. The misfit-dislocations results in a mosaic structure in LEED pattern as

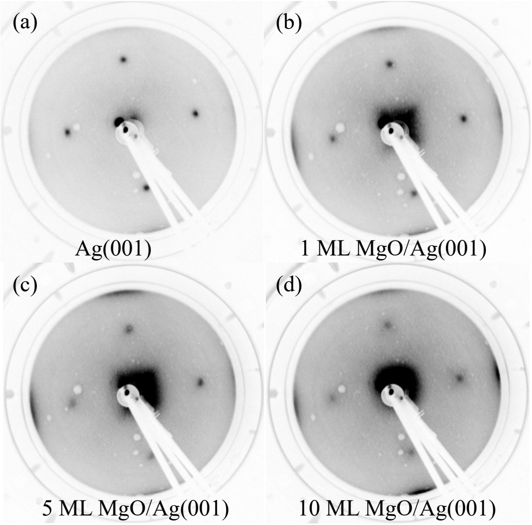

Figure 6.2: Half-order LEED spots at 22 eV of 2 ML CoO grown on different substrates; (a) Ag(001) (b) 1ML MgO/Ag(001) (c) 5 ML MgO/Ag(001) and (d) 10 ML MgO/Ag(001).

well as degrade the surface crystalline quality as observed in half-order spots of 2 ML CoO grown on 5 ML and 10 ML MgO [see Fig. 6.2(c)-(d)].

6.2.1 Nèel temperature variations with CoO and MgO coverage

Temperature dependent half-order LEED images were collected at 22 eV beam energy within the temperature range of 123 K to 343 K. Background subtracted half-order spot intensities were plotted with temperature to estimate the Nèel temperature of different CoO films, similar to the CoO/Ag(001) system. Fig. 6.3(a) shows the temperature variations of half-order (1/2,0) spot intensities for different CoO film coverages on 10 ML MgO/Ag(001). The intensity variation of the specular beam (0,0) of 2 ML CoO film is also shown to differentiate the nature of magnetic half-order and nonmagnetic integer-order spots. With increasing temperature, the intensity of the specular beam is reduced a little due to the thermal scattering of the electrons. Nèel temperatures have been estimated from the discontinuity of the slope of the polynomial fitted curves indicated by arrows as described in the previous chapter. With increasing CoO film coverage, the Nèel temperature gradually increases and

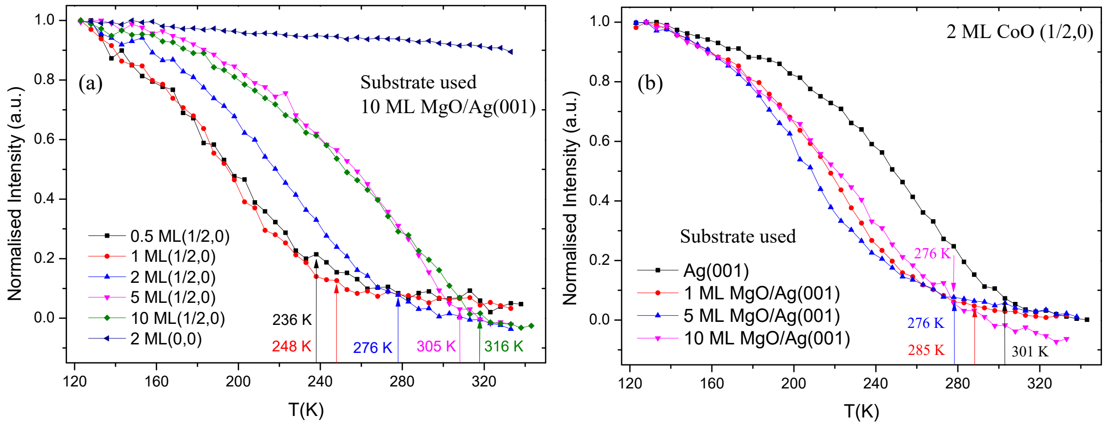

Figure 6.3: (a) Background subtracted half-order intensity variations with temperature for different CoO coverages on 10 ML CoO/Ag(001) and (b) for 2 ML CoO film on different substrates. The approximate Nèel temperatures are shown by arrows.

reaches to 316 K for 10 ML CoO. However, these temperatures are lower than the respective CoO coverages on bare Ag(001) below 10 ML CoO coverage [see Fig. 6.4(a)]. For 10 ML CoO, T_N is saturated at 316 K for Ag(001) and it also seems to be saturated for 10 ML MgO/Ag(001) substrates. Due to poor surface crystalline quality and consequently the diffuse half-order spots, we could not measure the T_N beyond 10 ML CoO on 10 ML MgO/Ag(001). The maximum reduction in T_N of 25 K was observed for 2 ML CoO grown on 10 ML MgO/Ag(001) relative to Ag(001).

The effect of substrate coverage, *i.e.* the MgO spacer layer coverage between CoO and Ag(001) on Nèel temperature has also been investigated by growing same CoO coverage on different coverages of MgO substrates. The half-order intensity variations with temperature of 2 ML CoO on different substrates are shown in Fig. 6.3(b). The Nèel temperature of 2 ML CoO on Ag(001) is 301 K and as the MgO spacer layer introduce, T_N decreases with increasing MgO coverage and start saturating from 5 ML MgO coverage. So, in general, the Nèel temperature of CoO/MgO/Ag(001) system is lower than CoO/Ag(001) system. The maximum decrease in Nèel temperature has been observed for 2 ML CoO is about 25 K [see Fig. 6.4(a)]. In order to explain this lowering of surface Nèel temperature of CoO in close proximity to a polarizable medium, finite size, interfacial lattice strain, and image charge screening effects need to be considered apart from the conventional Co $3d$-O $2p$ superexchange interaction. Fig. 6.4(b) show the in-plane lattice parameter variation with CoO film coverages on Ag(001), 10 ML MgO/Ag(001) and for MgO/Ag(001) as well. The lattice parameter of CoO remains the same in the lower coverage due to the pseudomorphic growth and gradually reaches close to the bulk value. The Nèel temperature variation of CoO film on Ag(001) has been already described by considering the combined effects of in-plane lattice strain, finite size and image charge screening effects in the previous chapter. The in-plane lattice parameters of MgO films on Ag(001) increases slowly with film coverage. The growth of CoO films on 10 ML MgO/Ag(001) is also pseudomorphic up to 2 ML and lattice parameter increases slowly with further increase in film

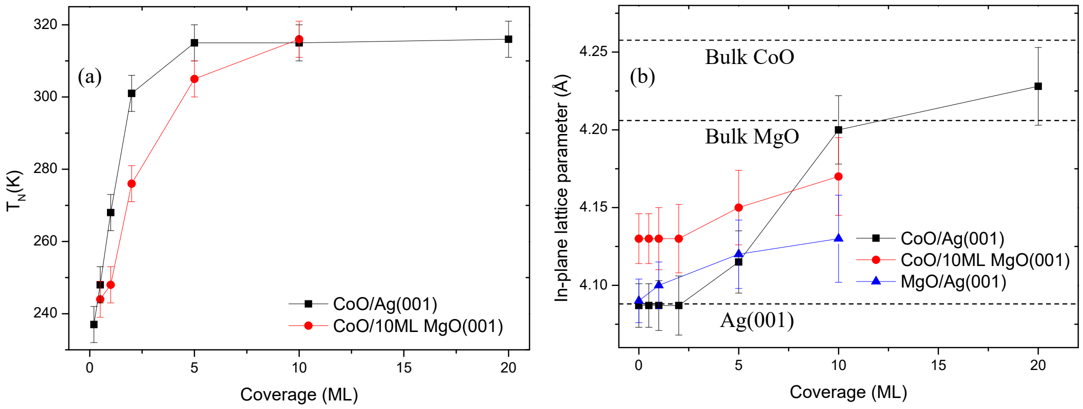

Figure 6.4: (a) Coverage dependent variation of T$_N$ of CoO on Ag(001) and 10 ML MgO/Ag(001). A manual error bar of T$_N$ was set by taking the twice of the temperature difference of two consecutive data points in half-order intensity-temperature curves. (b) Variation of in-plane lattice parameter of CoO on Ag(001), 10 ML MgO/Ag(001) and MgO on Ag(001). Error bars are proportional to the average diameter of the LEED spots. The horizontal dotted lines represent the bulk lattice parameters of CoO, MgO, and Ag(001).

coverages, similar to Ag(001). The in-plane lattice strain of CoO films on 10 ML MgO/Ag(001) is lower than Ag(001) up to 5 ML CoO coverage. Hence, the reduction of T$_N$ due to the lower strength of superexchange interaction relative to the Ag(001) substrate seems consistent. However, the observation of same T$_N$ of 10 ML CoO on 10 ML MgO/Ag(001) and on Ag(001) cannot be explained by only considering the strain induced enhancement of superexchange strength as 10 ML CoO has smaller in-plane lattice parameter on 10 ML MgO/Ag(001) than on Ag(001) [see Fig. 6.4(b)]. The finite size effect has also an impact on surface Nèel temperature need to be included as in the lower coverages T$_N$ reduces due to the least coordination number. At higher coverages, finite size effect and hence T$_N$ saturates due to the increased nearest neighbours. So, the reduction of T$_N$ upon insertion of 10 ML MgO spacer layer between CoO and Ag(001) can be explained by the substrate induced lattice strain for the lower CoO coverages, however, the strain effect is suppressed at higher coverage due to increased coordination number.

In order to explain the enhancement of T$_N$ of CoO on 10 ML MgO/Ag(001) over the bulk T$_N$ (291 K) of CoO, the image charge screening effect has to be introduced similar to the CoO/Ag(001) system. The enhancement of T$_N$ is lower for 10 ML MgO/Ag(001) than Ag(001) [see Fig. 6.4(a)] due to the presence of lower polarizable MgO substrate which is screening the image charge effect of highly polarizable Ag(001). For instance, 5 ML CoO on 10 ML MgO/Ag(001) [305 K] has 11 K lower T$_N$ compared to 5 ML CoO/Ag(001) [316 K]. The maximum reduction of T$_N$ of 25 K was observed for 2 ML CoO film on 10 ML MgO(001)/Ag(001) which has least image charge screening effect compared to Ag(001). Further, the variations of T$_N$ of 2 ML CoO film with the MgO spacer layer coverage can be explained by the different screening of image charge effect for different MgO coverages on Ag(001) [see Fig. 6.3(b)]. With increasing MgO coverage on Ag(001), the effect of image charge is screened by the less polarizable MgO substrate i.e., the values of U and Δ are increased relative to the CoO/Ag(001) system and consequently, the T$_N$ is reduced for a fixed CoO film coverage.

From the above discussion, it is clear that the image charge screening effect is the main reason behind the enhancement of T$_N$ for CoO(001) film grown on MgO/Ag(001). However, we do not observe huge changes in the surface Nèel temperature due to the image charge screening unlike Altieri *et al.* [29] have observed for NiO/MgO system.

6.2.2 Half-order spot profile analysis: domain size

Exchange scattered half-order spot intensity variations with temperature described the antiferromagnetic ordering of CoO on different substrates. Moreover, the intensity profile of half-order spot provides the information about the long-range antiferromagnetic ordering of the film. Using the inverse of full width at half maximum (FWHM) of half-order spots in proper units, a rough estimation of average antiferromagnetic $p(2 \times 1)$ domain size can be performed [204,205]. Fig. 6.5(a) show the line scan of the

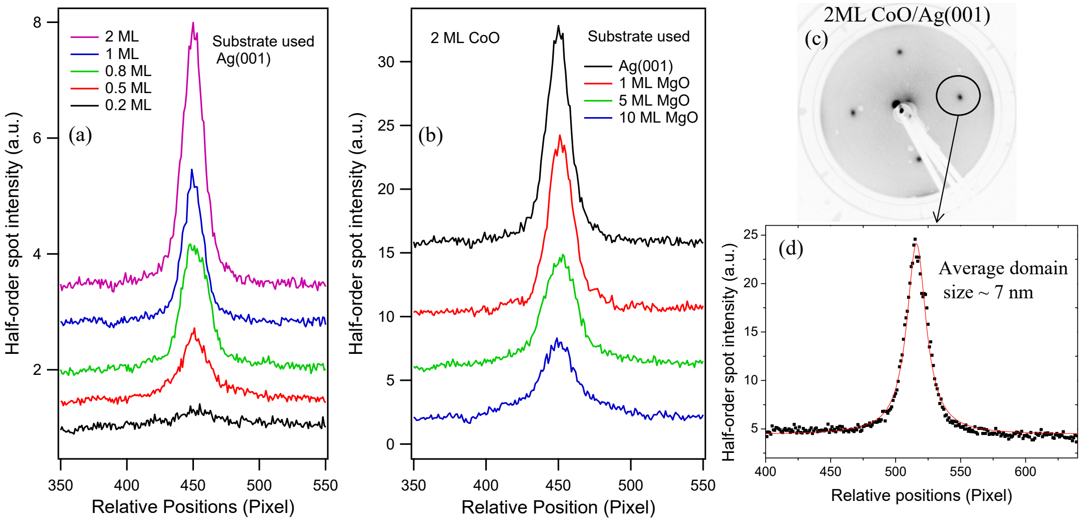

Figure 6.5: (a) Line scan of the half-order spot of CoO/Ag(001) surface, showing the increase of average domain size with film coverage. (b) MgO spacer layer coverage dependence of average domain size of CoO on MgO/Ag(001). (c)-(d) A Lorentzian fit of 2 ML CoO/Ag(001) gives an average domain size of 7 nm.

half-order spots of CoO on Ag(001) starting from submonolayer to 2 ML coverages. In the submonolayer regime, very weak and broad half-order spots were observed due to the finite size effects. With increasing coverage, the half-order spots become sharper with lower FWHM as the antiferromagnetic $p(2 \times 1)$ domain sizes are now dominated by the physical grain sizes in the film [22]. Bigger domain size corresponds to a longer antiferromagnetic correlation length and an enhanced exchange scattering strength, reflected in the increment of $p(2 \times 1)$ spot intensity. The sharpest half-order intensity with minimum FWHM was observed for 2 ML CoO on Ag(001). A Lorentzian fit of this intensity profile gives an average domain size of $\sim$ 7 nm [see Fig. 6.5(d)]. With further increase in film coverage, the spot profile does not improve due to the reduced surface crystalline quality in presence of weak intensity mosaic structure (not shown). Fig 6.5(b) show the half-order spot profiles of 2 ML CoO grown on different substrates. With increasing MgO spacer layer coverage the FWHM also increases relative to the Ag(001) substrate. So, screening of the image charge effects by MgO spacer layer not only reduces the T$_N$ of CoO films but also reduces the average antiferromagnetic domain sizes.

6.3 Critical exponent with Debye-Waller correction

The intensity of exchange scattered half-order LEED spots decreases with increasing temperature due to the reduction of the sublattice magnetization. In addition to that, the LEED spot intensity is also known to decrease with temperature due to thermally induced diffuse scattering. As a result, the beam intensity is reduced by the Debye-Waller factor, exp(-2W), where W is a function of temperature T [194]. Our experimental LEED intensities closely follow a simple temperature dependence in the form $I = I_0\exp(-\alpha T)$. Fig. 6.6(a) show the temperature variation of logarithmic intensities of (0,0) and (1/2,0) spots for 2 ML CoO film grown on Ag(001). For the integer order spot, ln(I) decreases linearly over the whole temperature range as a result of thermal vibrations. In contrast, for the half-order spots ln(I) is decreasing

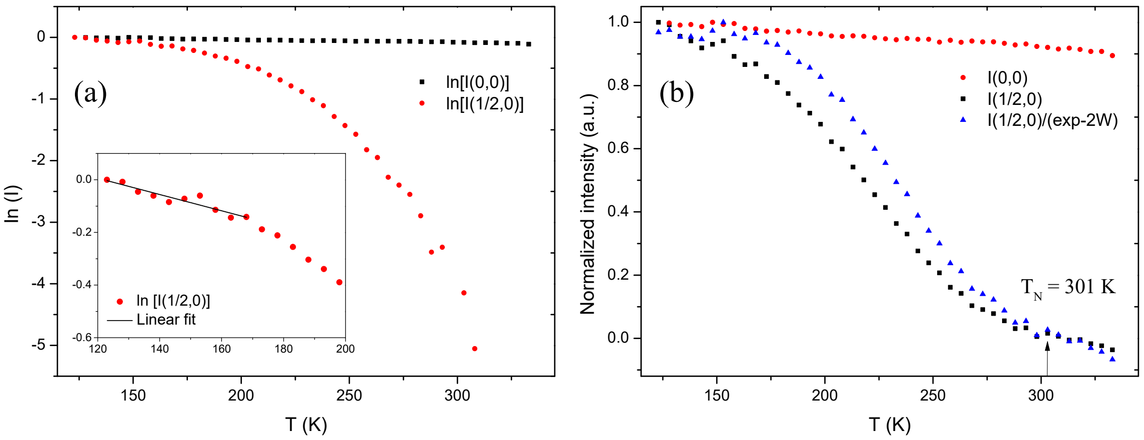

Figure 6.6: (a) Temperature dependent logarithmic intensity of (1/2,0) and (0,0) order LEED spots of 2 ML CoO on Ag(001). Inset shows the linear fit of the ln[I(1/2,0)] = f(T) curve between 120 and 140 K. (b) Debye-Waller factor corrected I(1/2,0)/exp(-2W) represents the temperature variation of $\langle M_s \rangle^2$. Despite the change in curvature, antiferromagnetic transition temperature T$_N$ remain the same as indicated by the arrow.

linearly with T only between ∼ 120 and 140 K and intensity (I) gradually falls to zero at the magnetic transition temperature. So, both thermal vibrations and decrease of the sublattice magnetization must contribute to the temperature dependence of the magnetic half-order spots. Fig. 6.6(b) shows the temperature dependence of the half-order intensity I(1/2,0) corrected by the Debye-Waller factor exp(-2W), along with the half and integer order intensities of 2 ML CoO. The Debye-Waller factor has been extracted from the linear part of the ln[I(1/2,0)] = f(T) curve, *i.e.*, between 120 and 140 K [see the inset of Fig. 6.6(a)]. The contributions of thermal vibrations are removed by this correction from the temperature dependence curve of I(1/2,0) and now it reflects the square of sublattice magnetization ($\langle M_s \rangle^2$) only as the half-order spot intensity I(1/2,0) is proportional to $\langle M_s \rangle^2$, the square of the thermal average of the spin moment component of the scattering atom [70]. The Debye-Waller correction slightly changed the curvature of the I(1/2,0) curve, though no change has been observed in the antiferromagnetic ordering temperature (T_N) [see Fig. 6.6(b)].

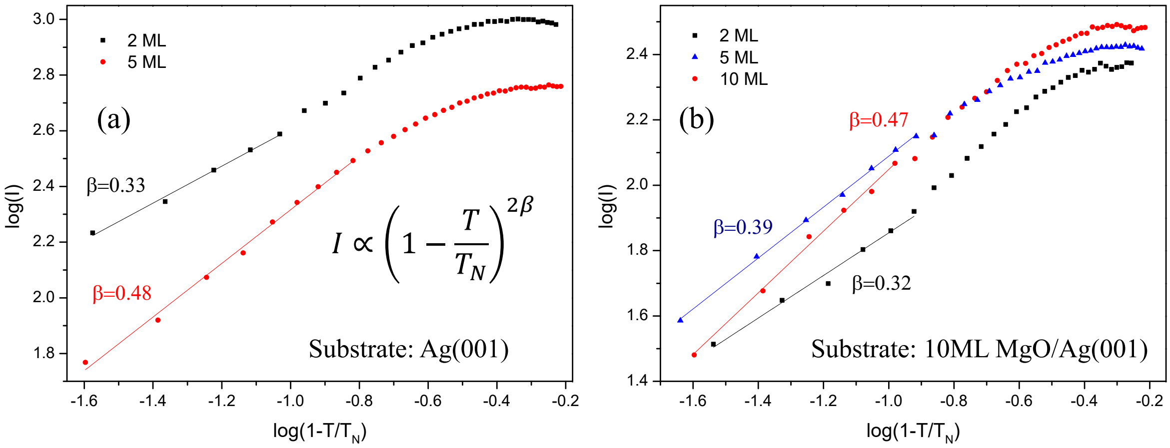

Figure 6.7: (a) Log-log plot of exchange scattered magnetic half-order intensity of CoO/Ag(001) films versus (1-T/T_N). The critical exponent obtained from the linear fits in the temperature range 0.97 T_N - 0.88 T_N are 0.33 and 0.48 for 2 and 5 ML CoO films, respectively. (b) The similar plot has also shown for CoO film grown on 10 ML MgO/Ag(001). The obtained critical exponents are 0.32, 0.39 and 0.47 for 2, 5 and 10 ML CoO, respectively.

The decay of antiferromagnetic long-range order of CoO film in the critical region can be described in terms of the critical exponent, β. The universal power law of spontaneous sublattice magnetization is given by $M(T) = M(0)(1 - T/T_N)^{\beta}$. The exchange scattered half-ordered LEED intensity is proportional to the square of the sublattice magnetization and thus we can estimate the value of 2β from $I(1/2, 0) = C(1 - T/T_N)^{2\beta}$ similar to other studies of Ising and Heisenberg systems [206,207]. Fig. 6.7(a) show the log(I) vs. log(1-T/T$_N$) plots for 2 and 5 ML CoO film on Ag(001). The correction for Debye-Waller factor has been into account though it does not have a significant effect on the critical exponent [206, 207]. The value of critical exponent has been estimated by linear fitting of the log(I) vs. log(1-T/T$_N$) plot in the temperature range of 0.97 T$_N$ - 0.88 T$_N$. The value of β was found to be around 0.33 for 2 ML CoO suggesting the three-dimensional Ising/Heisenberg like behaviour though it is increased to 0.48, close to the mean-field value (0.5) at 5 ML CoO film coverage. Similarly, the critical exponents gradually increases from 0.32 to 0.47 for going 2 ML to 10 ML CoO film grown on 10 ML MgO/Ag(001) [see Fig. 6.7(b)]. Moreover, β varies with temperature range as the log(I) vs. log(1-T/T$_N$) plot is not perfectly linear throughout the temperature range. It is known that no one theoretical model can describe satisfactorily the ordering behaviour of CoO over the entire temperature range [192]. Rechtin *et al.* [192, 206] have explained the critical behavior near T$_N$ of CoO by considering rigid lattice Ising-model with critical exponent values near 0.3125 (3D Ising model) is close to our observed exponent values for 2 ML CoO. This three-dimensional Ising/Heisenberg like magnetization decay can be explained by considering the growth of the quasi-2D islands of CoO on Ag(001) as described in chapter 3. Here, the ultrathin CoO films grown on Ag(001) or MgO are not an ideal 2D geometrical system due to the lack of perfect flat monolayer growth, often there are islands of a few atomic layer height can exhibit a quasi-2D system. If the LEED coherence lengths are comparable with the 3D islands sizes then it can give rise to a three-dimensional Ising/Heisenberg behavior even at 2 ML film coverage. At 10 ML CoO coverage, T_N saturates about 25 K higher than the bulk value, i.e., the surface exchange coupling (J_s) is stronger than the bulk exchange coupling (J_b). This should lead the CoO surface order a pure two-dimensional surface transition followed by a crossover behavior at T_N^b as the bulk counterpart at the same temperature is still in a paramagnetic state. However, with increasing film coverage we are having enhanced critical exponent value well above even the 3D Ising/Heisenberg antiferromagnet. At 10 ML coverage, the estimated exponent value approaches close to the mean-field value of 0.5. So, it is evident that there is a dimensional crossover from 3D Ising/Heisenberg to mean-field critical behavior. A recent numerical study by Monte-Carlo method predicts that there is a dimensional effect in the critical properties of multilayered Heisenberg films [208]. They have shown that the calculated critical exponents exhibit a dimensional transition from two dimensional to three dimensional properties of the films with increasing film thickness. Further, the scaling functions can also describe the crossover from Ising-like critical behavior to classical critical behavior in 2D systems [209]. Similar scaling functions in the vicinity of the critical point are necessary to describe our observed crossover from 3D Ising/Heisenberg to classical mean-field critical behavior properly.

It is reported in the literature [164, 207, 210] that surface critical exponent of prototype NiO film differs from the bulk critical exponent. However, the observed CoO exponent values seem to corresponds to the bulk values. Despite several similarities between NiO and CoO, the critical behavior is quite contrasting as NiO exhibit a surface extraordinary transition while CoO shows anomalous enhancement of surface sublattice magnetization with temperature increase [164]. The single site-anisotropy of CoO is quite higher relative to NiO both in bulk and on the (001) surfaces which can drive the critical behavior of CoO in different ways.

6.4 ARPES of CoO/MgO(001): Effect of AF order in valence electronic structure

Effect of antiferromagnetic order in the electronic structure of CoO/Ag(001) system has been already discussed in chapter 5. However, upon deposition of CoO on wide gap MgO substrate, Co $3d$ band dispersions are distinctly visible due to the absence of substrate bands within 0-4 eV binding energy range. Moreover, the reduced image charge screening in presence of MgO layers can modify the valence electronic structure significantly. Fig. 6.8(a)-(b) shows the ARPES band dispersion about $\overline{\Gamma}$ of 10 ML CoO on 10 ML MgO/Ag(001) using He I_α in both paramagnetic (343 K) and antiferromagnetic (123 K) phases. The main observed difference between PM and AFM band structure is the band splitting at about 5 eV binding energy as shown in Fig. 6.8(b) by arrow. Theoretical band structure calculation including the AF

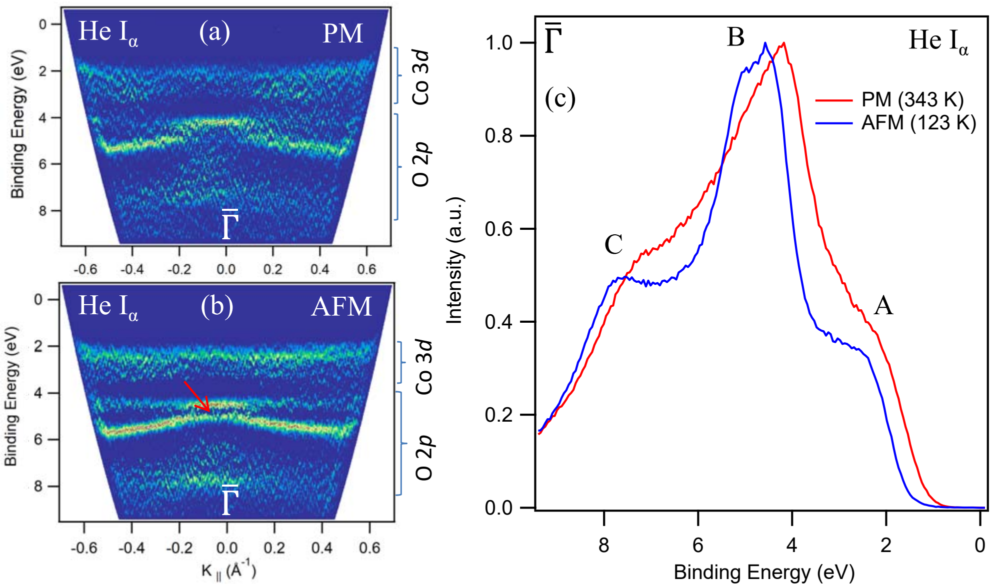

Figure 6.8: (a)-(b) ARPES band dispersion about $\overline{\Gamma}$ of 10 ML CoO in both PM and AFM phase using He I_α. The gap between two O $2p$ bands is shown by arrow. (c) ARPES spectra at $\overline{\Gamma}$ point to investigate the evolution of individual features upon PM to AFM transition.

order shows similar splitting of O $2p$ derived Δ_1 band [56]. It is also experimentally observed that even at paramagnetic phase the short-range magnetic order contributes to the local antiferromagnetic bands [56]. Moreover, the Co $3d$ band narrowing near Fermi level in AFM phase makes the insulating gap wider due to strong correlation effects. Fig. 6.8(c) shows the ARPES spectra at $\overline{\Gamma}$ point for both PM and AFM phases. The valence band edge is shifted towards higher binding energy in AFM phase showing the more insulating character of CoO relative to the PM phase. The feature 'A' corresponds to Co $3d$ states and the feature 'B' and 'C' are assigned to Δ_5 and Δ_1 symmetry oxygen bands, respectively. All these features are more prominent in AFM phase and also shifted to the higher binding energies possibly due to the image charge effects in addition to the antiferromagnetic band narrowing. The shoulder of the feature 'B' that appears in presence of long-range antiferromagnetic order exhibiting the small gap between two oxygen bands.

Similarly, the ARPES band dispersions of 10 ML CoO/10 ML MgO/Ag(001) for both paramagnetic (343 K) and antiferromagnetic (123 K) phases using He II_α are shown in Fig. 6.9. Here, Co $3d$ bands are distinctly visible with a gap in AFM phase as shown by arrow [Fig. 6.9(b)]. However, the non-dispersive O $2p$ bands are weaker relative to that of the He I_α. The effect of the band narrowing in Co $3d$ is stronger than O $2p$ as the magnetic moments are located at the Co sites. The ARPES spectra at $\overline{\Gamma}$ show the evolution of different features 'A', 'B','C' upon PM to AFM transition [see Fig. 6.9(c)]. The Co $3d$ feature 'A' and 'B' get enhanced and the band edge is shifted to the higher binding energy results the insulating gap opening in AFM phase. The feature 'C' associated with O $2p$ is shifted to the higher binding energy possibly due to the image charge screening in addition to the AFM band narrowing.

Despite the intensity enhancement due to band narrowing of antiferromagnetic CoO, no major changes in valence electronic structure were observed in presence of antiferromagnetic ordering in the sample. The short-range magnetic correlation persists well above the Nèel temperature as observed by neutron diffraction exper-

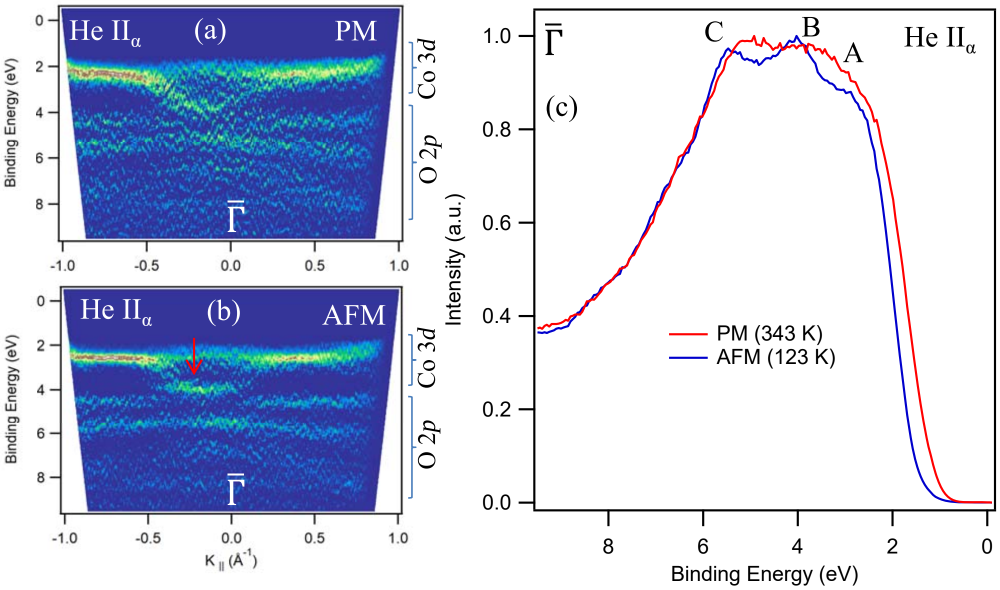

Figure 6.9: (a)-(b) ARPES band dispersion about $\overline{\Gamma}$ of 10 ML CoO in both PM and AFM phase using He II$_\alpha$. The gap between two Co $3d$ bands is shown by arrow. (c) ARPES spectra at $\overline{\Gamma}$ to monitor the individual features upon PM to AFM transition.

iments [18, 196, 197]. This short-range magnetic correlations whose length scale is larger than the photoemission correlations length makes the electronic structure similar in both AFM and PM phase, as already observed in CoO single crystal by Shen *et al.* [56].

6.5 Summary

Evolution of magnetic $p(2\times1)$ half-order spot with CoO film coverage on MgO/Ag(001) as well as on several Ag(001) supported MgO substrate coverages were investigated. The effects of underlying MgO substrate on antiferromagnetic ordering temperature was studied using the temperature dependent exchange scattered half-order intensity profiles. The variations of Nèel temperature with film and substrate coverage were explained using the combined effects of finite size, in-plane lattice strain, and image charge screening. A rough estimation of average antiferromagnetic domain size was carried out from the FWHM of the Lorentzian fitted half-order intensity profile. Moreover, the variations of FWHM of different films with different conditions gives an idea about the average domain size of the films. The reduction of LEED spot intensity with increasing temperature due to diffuse scattering *i.e.*, the Debye-Waller factor was corrected, though it has a little effect on sublattice magnetization. The decay of long-range antiferromagnetic order in the critical region has been described using the universal power law of spontaneous sublattice magnetization. The value of critical exponent β suggest a 3D Ising/Heisenberg behavior in low film coverage, however, a mean-field behavior is observed in higher film coverage. The temperature dependent ARPES study reveals the evidence of short-range antiferromagnetic ordering above the Nèel temperature as the valence band electronic structure is similar in both PM and AFM phase except the small gap opening with the narrowing of Co $3d$ and O $2p$ bands.

7

Growth and Characterization of Fe_xO on Ag(001) and MgO/Ag(001)

7.1 Introduction

Iron oxides and their surfaces are important for various applications in a large number of areas, such as sensors, catalysis, corrosion and magnetism [211–213]. Despite technological and scientific interests, the growth of iron oxide thin films such as FeO (wustite), Fe_3O_4 (magnetite) and Fe_2O_3 (hematite) are still poorly understood. The main concern of these iron oxide growth studies is the preparation of well-ordered stable surfaces. To investigate the growth of well-defined stable surfaces, different strategies have been adopted such as single crystal oxidation, oxygen assisted molecular beam epitaxy (MBE) and sequential iron deposition/oxidation cycles on metallic substrates [214]. Generally, the grown films contain more than one crystallographic phase [215] due to the different available oxidation states of Fe. Attempts have been made by several groups of researchers to grow FeO films on different substrates. In order to study the intrinsic properties of $Fe_{1-y}O$ surfaces, one might think to grow non-polar $Fe_{1-y}O(001)$ on Ag(001) substrate. However, despite the small lattice mismatch, the growth of FeO on Ag(001) results in the growth of a hexagonal FeO(111) phase for few-monolayer coverage regime. This clearly demonstrates that the polar orientation is strongly favored for the low film coverage regime. However, Merte *et al.* [216] have shown that grains of $Fe_{1-y}O(001)$ were formed *via* the oxidation of metallic Fe grains at 623 K and 2×10^{-7} mbar oxygen on Ag(001). Kim *et al.* [217] have grown oriented FeO film on Si(100) from Fe_3O_4 containing Fe nanocrystallines by post-annealing at 873 K. As FeO is found to be stable only above 843 K [218], below this temperature it decomposes back to metallic Fe and Fe_3O_4. Recently, Abreu *et al.* [215] have grown iron oxide films on atomically clean Ag(001) surface by molecular beam epitaxy (MBE). They have prepared series of iron oxide films by varying different growth parameters such as atomic flux, oxygen partial pressure, annealing temperature to establish the best preparation conditions for obtaining films with the highest concentration of FeO(100) phase. Depending upon the oxygen partial pressure, the sample contains both Fe_3O_4 as well as metallic Fe. Annealing at higher temperatures, the Fe_3O_4 transforms into FeO, though it worsens the surface epitaxial order as observed by LEED and XPS. Sebastien *et al.* [219] have shown that growth of a pure metal on the native metal oxide layers can reduce the oxide to its lowest oxidation state and stabilized it. They have studied the *in situ* oxidation of iron layers and the chemical changes induced by subsequent deposition of Fe metal using hard x-ray absorption spectroscopy.

The physical and chemical properties of oxides are dependent on the exposed crystallographic surface. For example, wustite or FeO has rocksalt structure and consists of alternating (111) planes of either only Fe or O atoms, *i.e.*, it possesses a polar surface termination. On the other hand, the (001) termination is non-polar as it consists of 50% Fe and 50% O atoms. The stoichiometric FeO has the lowest contingent of oxygen and it is not stable under ambient condition. Therefore, FeO exhibits iron deficiencies which are usually indicated by the notation, $Fe_{1-\delta}O$ with $0.04 < \delta < 0.12$ [39]. Rocksalt FeO exhibits antiferromagnetism below the Nèel temperature of 198 K, with the Fe^{2+} spin arrangement parallel to the (111) planes and antiparallel to the adjacent planes similar to CoO [220, 221]. However, the magnetic axis of FeO is perpendicular to (111) plane unlike the other transition metal oxides [17]. The surface magnetism of FeO is poorly explored in the literature possibly due to the lack of a well-ordered stoichiometric surface. Real FeO samples will always have Fe^{2+} vacancies, and these vacancies induce the creation of two Fe^{3+} ions. Therefore, in addition to antiferromagnetic superexchange interaction within Fe^{2+}-O^{2-}-Fe^{2+} network, a ferromagnetic interaction may appear between Fe^{2+} and Fe^{3+} ions in the neighborhoods of Fe^{2+} vacancies [220].

7.2 Growth of Fe_xO film on Ag(001)

The growth of stoichiometric single phase iron oxide is quite challenging due to its complex phase diagram. We have undertaken a detailed growth study of FeO on Ag(001) using reactive evaporation of Fe under oxygen environment. Different growth parameters such as substrate temperature, oxygen partial pressure, post-growth annealing conditions etc. were varied to obtain the well-ordered $Fe_xO(001)$ surface with maximum Fe^{2+} content. Well polished and atomically clean Ag(001) single crystal was used to grow Fe_xO at various growth conditions. The surface crystalline quality was investigated by LEED whereas XPS was used to monitor the relative binding energy positions of different core levels to obtain the stoichiometric information of the grown films. Moreover, a coverage dependent evolution of surface geometrical as well as electronic structure were investigated by LEED and XPS, respectively.

7.2.1 Growth at different conditions: LEED and XPS study

Fig. 7.1(a)-(d) show the LEED pattern of 3 ML Fe_xO films grown at different growth and post-growth annealing conditions. All the LEED images were collected at 85 eV primary beam energy where the superstructures are clearly visible with the regular

$p(1 \times 1)$ pattern. Initially, 3 ML Fe$_x$O was grown on Ag(001) at 473 K substrate temperature and 5×10^{-8} mbar oxygen partial pressure [see Fig. 7.1(a)]. Post-growth annealing at three different conditions was performed with the aim of improved surface crystalline quality and stoichiometry. Annealing at 573 K with 1×10^{-7} mbar oxygen partial pressure exhibit a $p(2 \times 1)$ twin domain superstructure as shown in Fig. 7.1(b). Annealing at relatively lower oxygen pressure (7×10^{-8} mbar) shows apparently similar LEED superstructure as before. However, a closer inspection reveals that each superstructure spot consists of uniaxially split diffraction spots [see Fig. 7.1(d)]. Annealing in absence of oxygen at 573 K improves the LEED spots quality as the high intensity backgrounds around each spot are reduced and the next higher order low intensity spots appear [see Fig. 7.1(c)]. Fig. 7.2 shows the

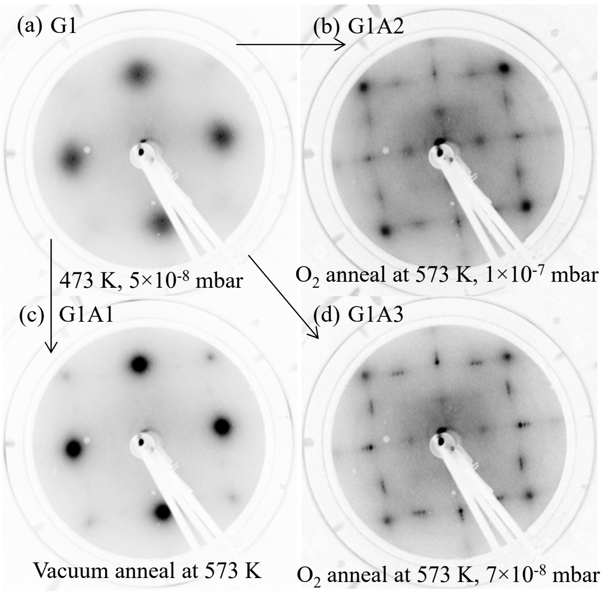

Figure 7.1: LEED images at 85 eV beam energy for different growth and post-growth annealing conditions of a 3 ML Fe$_x$O film. All the growth and post-growth conditions are labeled by G1 and G1A1, G1A2, G1A3, respectively. (a) Grown at 473 K substrate temperature and 5×10^{-8} mbar oxygen partial pressure (G1). (b) Oxygen annealing at 573 K and 1×10^{-7} mbar (G1A2). (c) Vacuum annealing at 573 K (G1A1). (d) Oxygen annealing at 573 K and 7×10^{-8} mbar (G1A3).

LEED patterns of 3 ML Fe_xO films grown at two more substrate temperatures and corresponding post-growth annealing conditions. Growth at RT with 5×10^{-8} mbar oxygen pressure and immediate post-growth annealing with the same oxygen pressure at 723 K (G2A1) shows somewhat similar superstructure LEED pattern as described in the case of Fig. 7.1(d). Similar LEED superstructure has also observed by Merte *et al.* [216] for the initial stages of iron oxide film growth on Ag(001). They have shown that these superstructures correspond to the oxygen-rich hexagonal multilayer phase of Fe_xO. Growth at intermediate 373 K with 5×10^{-8} mbar oxygen pressure show a regular (1×1) structure with high background intensity [see Fig. 7.2(b)]. Upon annealing in absence of oxygen at 473 K, the spot intensity improves indicating the presence of low defect density in the film as shown in Fig. 7.2(c). So, the surface crystalline quality is improved significantly in the growth modes G2A1 and G3A1 [Fig. 7.2] than the G1A1 and G1A2 [Fig. 7.1] despite the presence of multi-domain superstructure.

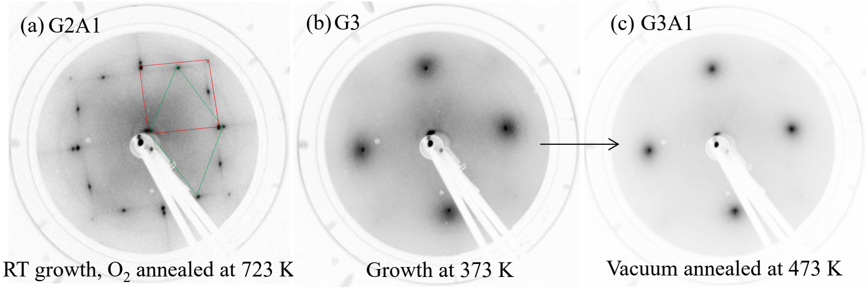

Figure 7.2: LEED images of 3 ML Fe_xO at 85 eV for (a) RT growth and immediate oxygen annealing at 723 K (G2A1), (b) Growth at 373 K (G3), and (c) post-growth vacuum annealing at 473 K (G3A1).

Fig. 7.3(a) show the corresponding Fe $2p$ XPS spectra for different growth and post-growth annealing conditions as discussed in the LEED study. The growth at 473 K with 5×10^{-8} mbar oxygen pressure (G1) show a non-stoichiometric Fe_xO film as the $2p_{3/2,1/2}$ peaks are shifted to the lower binding energies relative to the corresponding positions of the stoichiometric FeO film. The spectrum primarily

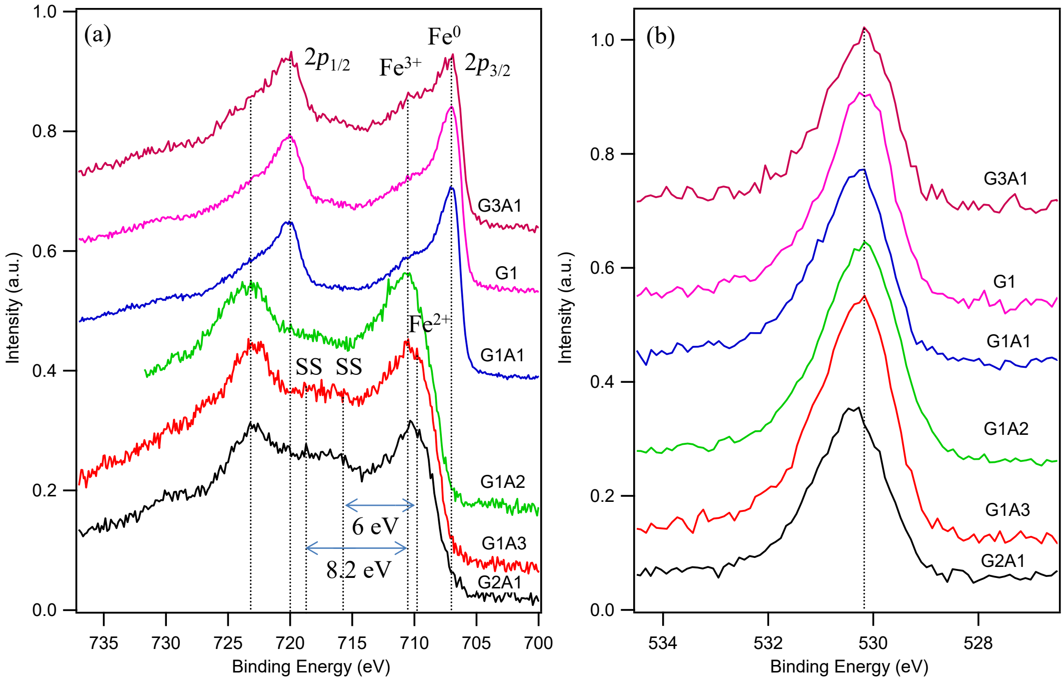

Figure 7.3: Core level XPS spectra of 3 ML Fe_xO at different growth and post-growth conditions. (a) Fe 2p spectra show the evolution of $2p_{3/2,1/2}$ and their respective shake-up satellites. (b) O 1s spectra show no significant change in binding energy upon growth and post-growth conditions except for the growth G2A1.

consists of metallic Fe^0 peak at 707 eV with minor contributions of Fe^{2+}/Fe^{3+} at about 710.5 eV. Upon post-growth annealing in absence of oxygen (G1A1), the Fe 2p peak positions do not change despite the improvement of $p(1 \times 1)$ LEED spot intensity. However, the post-growth annealing at higher oxygen partial pressures (G1A2 and G1A3) result in the shift of 2p core level towards higher binding energy with the superstructure LEED patterns. Now the spectra consist of Fe^{2+}/Fe^{3+} emissions and the characteristic weak intensity shake-up satellites. These satellites are located at well-known binding energies according to the cation species [222]. The Fe $2p_{3/2}$ shake-up satellites of Fe^{2+} and Fe^{3+} are located at 714.9 eV and 719.2 eV binding energies, respectively [223]. Moreover, the energy separation between $2p_{3/2}$ and the corresponding shake-up satellite is also an important indicator to investigate the iron oxides stoichiometry. Stoichiometric FeO has a gap of ∼ 6 eV between $2p_{3/2}$

and Fe^{2+} satellite [215]. Here, the best possible observed values of $2p_{3/2}$ and Fe^{2+} satellite are 709.8 eV and 715.8 eV, respectively, with a separation of 6 eV [see Fig. 7.3(a)]. In addition to that, the $2p_{3/2}$ peak and the corresponding shake-up satellite of Fe^{3+} are also observed at 710.5 eV and 718.7 eV, respectively, with a separation of 8.2 eV indicating Fe_2O_3 stoichiometry [see Fig. 7.3(a)]. All these Fe^{2+}/Fe^{3+} peaks and corresponding satellites separations are consistent with the Fe_xO/Fe_2O_3 stoichiometries, respectively [222, 223].

So, it is evident that the grown sample contains both Fe^{2+} and Fe^{3+} with a ratio, which needs to be estimated. The main task of this growth optimization is to increase the Fe^{2+} contains in the Fe_xO film grown on Ag(001). Growth at RT followed by the post-growth oxygen annealing at the higher temperature (G2A1) also provides similar Fe $2p$ spectrum with all the features at the same binding energies as G1A2 and G1A3. Growth at 373 K followed by post-growth annealing in absence of oxygen (G3A1) again shows a non-stoichiometric growth as the peaks are shifted to the lower binding energies. The O $1s$ peak is almost at the same binding energy position for all the growth and post-growth annealing conditions except for the RT growth(G2A1). So, for all the growth conditions the films are either non-stoichiometric with the contributions of $Fe^0/Fe^{2+}/Fe^{3+}$ cations or the superstructured LEED suggesting to tune the growth conditions further for desired (1×1) stoichiometric FeO growth.

7.2.2 Coverage dependent evolution of surface geometric and electronic structure

Growth mechanism of ultrathin layers of Fe_xO on a metallic substrate and their geometric and electronic structures can differ from bulk due to the finite size effects in reduced dimension. In order to investigate these aspects coverage dependent growth studies have been performed using LEED and XPS. Three different films of coverages 3 ML, 6 ML, and 9 ML were grown at 423 K with 2×10^{-8} mbar oxygen

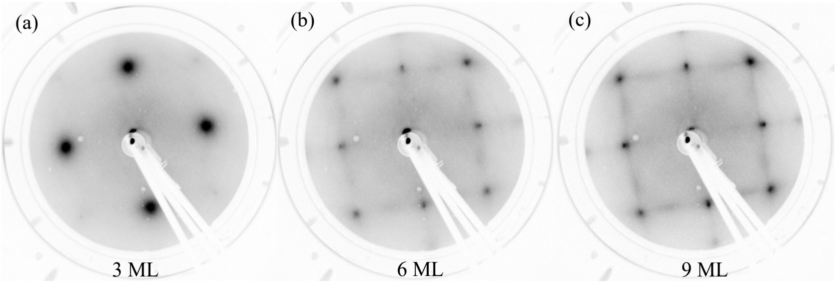

Figure 7.4: Coverage dependent LEED patterns for (a) 3 ML (b) 6 ML (c) 9 ML Fe_xO/Ag(001). All the images were taken at 85 eV beam energy.

partial pressure. Fig. 7.4 shows the LEED patterns of these films taken at 85 eV electron beam energy. At 3 ML coverage, a p(1×1) pattern with distinct first order spots was observed. As the coverage increases the higher order spots also get equally intense with a stripe-like LEED pattern [see Fig. 7.4(b)-(c)]. The appearance of these

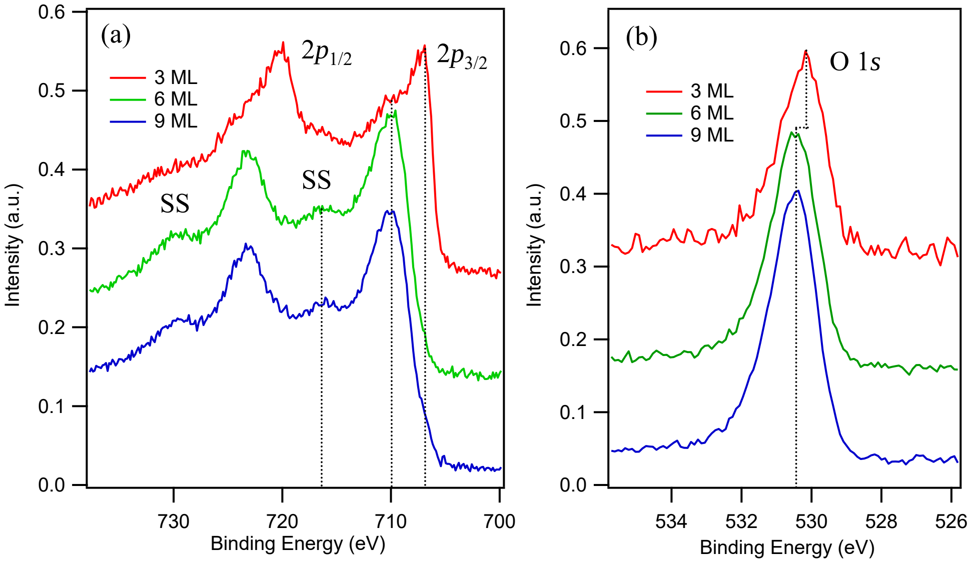

Figure 7.5: (a) Coverage dependent evolution of (a) Fe $2p$ and (b) O $1s$ spectra of Fe_xO/Ag(001). The shake-up satellites are denoted by SS.

stripe structure could be due to the oxygen vacancy ordering with a distribution for higher film coverages as it is generally considered that the required oxygen doses also increases with increasing coverage for stoichiometric growth. The expected pseudomorphic growth at 3 ML coverage is also consistent with the observed stripe-free (1×1) LEED pattern. Fig. 7.5(a)-(b) show the Fe $2p$ and O $1s$ spectra for the above mentioned three $\mathrm{Fe}_x\mathrm{O}$ coverages, respectively. It is quite striking that 3 ML film shows non-stoichiometric growth, however, at the same growth conditions for 6 and 9 ML films showing the Fe $2p$ features corresponding to $\mathrm{Fe}_x\mathrm{O}$ growth. Similarly, O $1s$ spectrum is also shifted to lower binding energy for 3 ML film relative to the 6 ML or 9 ML film coverages. From 6 ML onwards, we have observed $2p_{3/2}$ peak and the corresponding shake-up satellite of Fe^{2+} at 710 eV and 716.2 eV, respectively, with a gap of 6.2 eV and O $1s$ peak at 530.5 eV are in good agreement with the available stoichiometric FeO data [215]. The characteristic shake-up satellites of Fe^{2+} are more prominent relative to the main $2p_{3/2}$ peak for higher film coverages indicates an increase of the Fe^{2+} content in $\mathrm{Fe}_x\mathrm{O}$. Detailed investigation of the stoichiometry of the $\mathrm{Fe}_x\mathrm{O}$ film will be discussed in the next section.

7.2.3 Stoichiometry of $\mathrm{Fe}_x\mathrm{O}$ film: XPS analysis

Fig. 7.6(a) show the Fe $2p$ spectra of 9 ML $\mathrm{Fe}_x\mathrm{O}$ fitted with CasaXPS to extract the stoichiometric information of the film. The Shirley background has been used to effectively describe the inelastic electron background under the whole spectrum. The $2p_{3/2,1/2}$ peaks and their corresponding shake-up satellites (SS) are fitted with the mixed Gaussian-Lorentzian (GL) curves to obtain the raw area under the spectrum. Similarly, the raw area under the background subtracted O $1s$ peak also estimated as shown in Fig. 7.6(b). These raw areas were normalized (divided) by the photoionization cross section at the used photon energy. The atomic concentration of Fe in $\mathrm{Fe}_x\mathrm{O}$ or Fe:O ratio has been estimated by the ratio of the normalized area under Fe $2p$ and O$1s$ peaks. The Fe:O ratio is found to be $0.53 : 0.47$ which is an overestimation for several possible reasons. Firstly, the Fe $2p$ peak area we measured is a sum of all the individual peak areas which were multiple overlapped and were

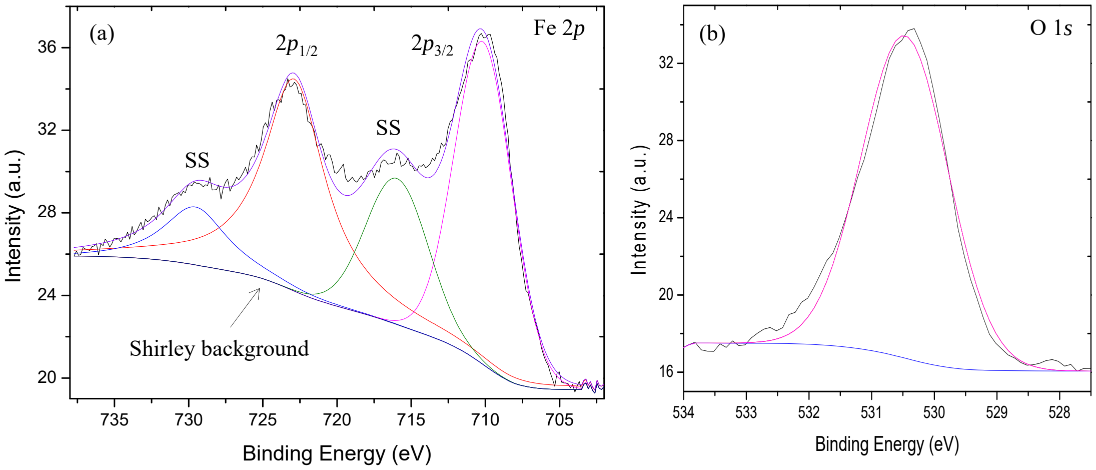

Figure 7.6: (a) Fe 2p spectra of 9 ML Fe$_x$O fitted with Gaussian-Lorentzian line-shapes (Gaussian:Lorentzian=40:60) showing individual components. The shake-up satellites are denoted by SS. (b) O 1s spectra.

not considered properly. Secondly, it depends on the choice of the relative sensitivity factors (RSF)/photoionization cross sections of the 2p lines used for calculating the atomic concentration. Wagner *et al.* [224] had shown that the sensitivity factors for the 2p lines of transition metals varied quite significantly with the chemical state due to the multi-electron processes. Therefore, it is difficult to determine the Fe oxidation

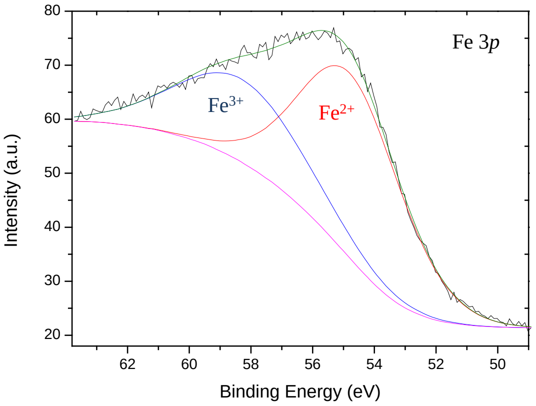

Figure 7.7: Fe 3p spectra of 9 ML Fe$_x$O showing both Fe^{2+} and Fe^{3+} components. The curve fitting was carried out using the GL ratio=40 (Gaussian:Lorentzian=60:40).

state accurately with the use of general sensitivity factors. An alternative way is to use Fe 3*p* peak to avoid the complexity of Fe 2*p* spectra. It is a single peak without any interfering satellite peaks. The peak has been fitted considering both Fe^{2+} and Fe^{3+} components [see Fig. 7.7]. The ratio of $Fe^{2+} : Fe^{3+} = 0.63 : 0.37$ is obtained from the Fe 3*p* spectra. Since $Fe_{1-y}O$ can be expressed as $2yFe^{3+}(1-3y)Fe^{2+}O$, the $Fe_{1-y}O$ having ionic ratio of $Fe^{2+} : Fe^{3+} = 0.63 : 0.37$ should have y=0.16. So, the 9 ML film is estimated to have a composition of $Fe_{0.84}O$. However, it is known that wustite is the most unstable iron oxide even under ultrahigh vacuum conditions; the surface layer of this oxide become progressively further oxidized, leading to changes in the surface stoichiometry of the material.

7.3 Growth of Fe_xO film on 5 ML MgO/Ag(001)

The growth mechanism of oxide films on a substrate may vary depending upon the different parameters of the concerned substrate such as lattice misfit, crystal plane orientation, film-substrate interaction, surface energy etc. There are several growth studies of FeO on polar (111) as well as non-polar metallic surfaces known in the literature [215, 216, 225]. However, the growth of FeO on oxide surfaces are still limited. Surface X-ray diffraction study of MgO/Fe(001) interface reveals the presence of a substoichiometric FeO layer between the bulk Fe(001) substrate and MgO adlayers [226]. So it is evident that the presence of MgO layer adjacent to Fe_xO film can control the stoichiometry as well as the growth dynamics. We have taken MgO(001) as the oxide substrate to grow Fe_xO due to the small lattice mismatch between them. Bulk MgO is a wide gap insulator which prevents the photoemission as well as LEED measurements due to the space charge effects. In order to rule out this issue, 5 ML MgO film was grown on Ag(001) and used as a substrate for Fe_xO growth. All the growth of Fe_xO on 5 ML MgO/Ag(001) has been performed at 473 K with an oxygen background pressure of 7×10^{-9} mbar, which is quite lower than that of the Fe_xO/Ag(001) system.

7.3.1 Coverage dependence: LEED and XPS study

Fig. 7.8 shows the LEED pattern at 85 eV for different film coverages of Fe$_x$O grown on 5 ML MgO/Ag(001). A well-ordered p(1×1) LEED pattern with intense sharp spots has been observed for the lower film coverages. With increasing coverage the spot quality degrades due to the presence of increased defect states in the sample. However, the overall LEED quality is superior to that observed during film growth on Ag(001) [see Figs. 7.1 and 7.2]. The strain in Fe$_x$O film on 5 ML MgO/Ag(001) is slightly lower than that on the bare Ag(001) as MgO grows almost pseudomorphocally on Ag(001) up to initial few layers and the strain relaxes at higher coverages by the formation of misfit dislocation network ascribed to the mosaic structure. The growth details of MgO on Ag(001) has already been discussed in chapter 4. These reduced strain in Fe$_x$O results in the improvement of surface crystalline quality for the lower film coverages [see Fig. 7.8(a)-(c)]. For higher coverages, there appears a

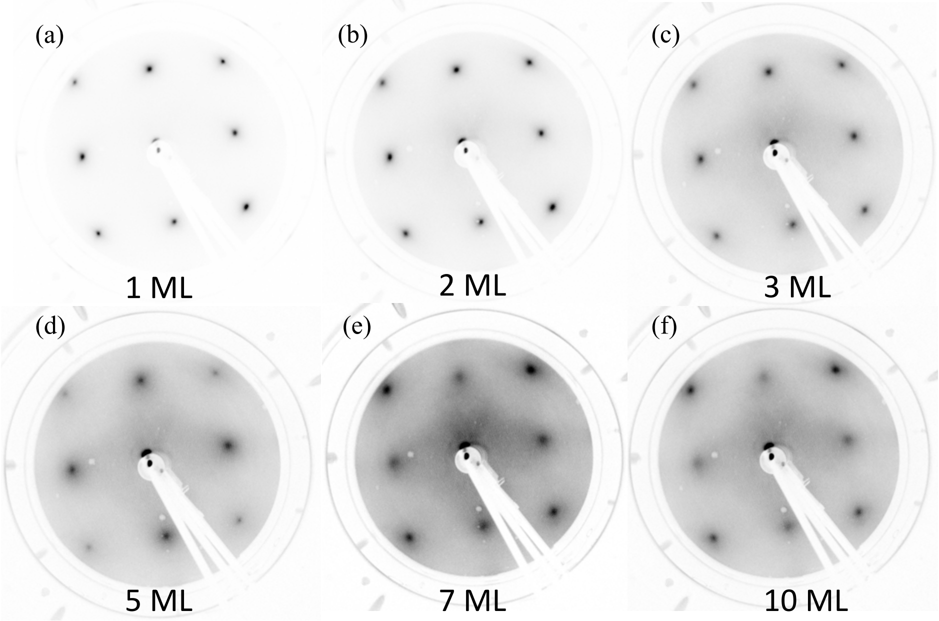

Figure 7.8: Coverage dependent LEED images collected at 85 eV for (a) 1 ML, (b) 2 ML, (c) 3 ML, (d) 5 ML, (e) 7 ML and (f) 10 ML Fe$_x$O on 5 ML MgO/Ag(001).

background around each LEED spot ascribed as the increased defect density for the higher film coverages [see Fig. 7.8(d)-(f)]. Fig. 7.9 (a)-(b) show the XPS spectra of Fe $2p$ and O $1s$ for various Fe$_x$O film coverages grown on 5ML MgO/Ag(001). The binding energies of $2p_{3/2}$ and the corresponding shake-up satellite are found to be at 709.9 eV and 716 eV with a separation of 6.1 eV. Here the characteristic Fe^{2+} satellites are more prominent relative to that of the Fe$_x$O/Ag(001) system indicating the enhancement of Fe^{2+} content in these samples. The O $1s$ binding energy positions are found to be at 530.6 eV for all the coverages which are very close to the reported value [215]. Moreover, the estimated stoichiometry of 10 ML Fe$_x$O (Fe$_{0.92}$O) is also found to be improved compared to the case of Ag(001) (not shown). It is reported that $2p_{3/2}$ satellite peak is absent for Fe$_3$O$_4$ which rule out the possibility of Fe$_3$O$_4$ stoichiometry [227]. However, Fe$_2$O$_3$ has also satellite peak approximately 8 eV higher binding energy than from the main $2p_{3/2}$ peak as it

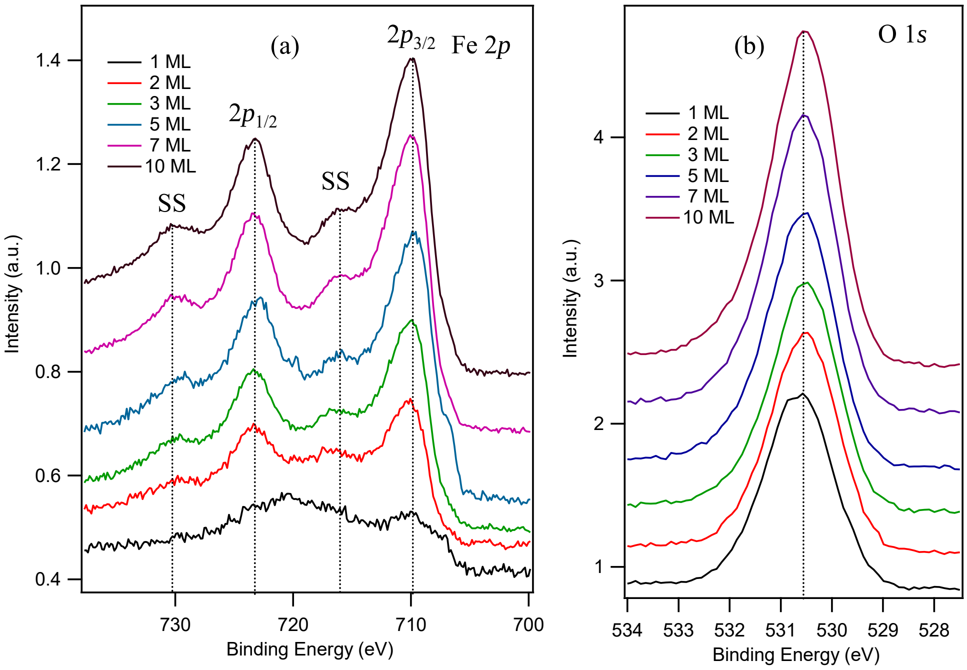

Figure 7.9: Coverage dependent (a) Fe $2p$ and (b) O $1s$ spectra of Fe$_x$O films on 5 ML MgO/Ag(001).

the intrinsic feature of Fe^{2+}. The reported values of $2p_{3/2}$ peak of Fe_2O_3 are lying between 710.6 eV to 711.2 eV [222, 227]. Our observed values are found to be about at 709.9 eV with approximate 6 eV satellite separation is a clear indication of the Fe_xO stoichiometry [215]. The growth of Fe_xO on MgO/Ag(001) has improved the surface crystalline quality as well as the enhancement of Fe^{2+} content as explained qualitatively using LEED and XPS results, respectively. In order to investigate the role of the MgO spacer layer between Fe_xO and Ag(001), Mg 1*s* core level was monitored with film coverage [see Fig. 7.10]. With increasing Fe_xO coverages, Mg 1*s* is shifted to lower binding energy till 3 ML and returned to the same binding energy with further the increase in coverage. This Mg 1*s* peak shift to the lower

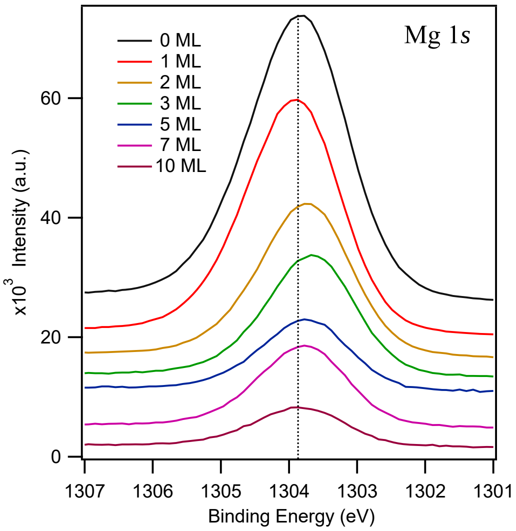

Figure 7.10: Evolution of Mg 1*s* spectra of 5 ML MgO/Ag(001) with Fe_xO film coverages.

binding energy is likely due to the reduction of MgO lattice oxygen to form Fe_xO interfacial layer. However, it is reported that for the growth of 3 ML Mg films on preoxidized FeO/Fe(001) surface, MgO films are formed through the oxygen transfer from FeO to Mg which is the opposite case to our results [228]. It is to be noted that the bond dissociation energy of MgO is slightly lower than FeO, 394 and 409 KJ/mole, respectively [229]. Moreover, in the strained ultrathin MgO film, the formation energy of MgO become larger than FeO, in favour of our results [228]. We observe Fe_xO induced metallic Mg feature at the interface in terms of Mg 1s peak shift to the lower binding energies upon deposition of Fe_xO layers on stoichiometric MgO/Ag(001) surface. With increasing Fe_xO coverage this process is stabilized by the formation of interfacial FeO layers. For 3 ML Fe_xO, the intensity of the metallic Mg signal probed by XPS is maximum as the peak is shifted towards lower binding energy. With increasing coverage, the metallic Mg contribution probed by the XPS decreases due to increased amount of MgO signal and the Mg 1s peak is shifted back to the same binding energy position.

7.3.2 ARPES of Fe_xO/5 ML MgO/Ag(001): Temperature dependence

The magnetic structure of bulk FeO is well known as it has been studied extensively using neutron diffraction technique [17, 160, 220, 230]. However, the situation is different for the ultrathin films as the growth of stoichiometric FeO film is difficult, which always show some Fe-deficiency. In this work, our primary motive was to grow a well-ordered Fe_xO film with maximum possible Fe^{2+} content and to study the surface magnetism and electronic structure using exchange scattered LEED intensity and ARPES techniques, respectively. Despite the well-ordered $p(1 \times 1)$ LEED pattern on both Ag(001) and on 5 ML MgO/Ag(001) substrates, the absence of exchange scattered half-ordered LEED spots well below the bulk Nèel temperature (198 K) restricted our investigation to the temperature dependent ARPES measurement only. There are several probable reasons for the absence of antiferromagnetic half-order spots. Firstly, the insufficient surface crystalline quality, disorder and surface non-stoichiometry can cause the absence of these weak intensity exchange scattered LEED spots. Secondly, the antiferromagnetic ordering temperature may be reduced below 120 K due to non-stoichiometry of the film which is beyond our experimental temperature range. We have preferred MgO supported 10 ML Fe_xO films for valence band electronic structure studies over Fe$_x$O on Ag(001) due to improve surface crystalline quality and to investigate the effects of reduced image charge screening on the valence band structure.

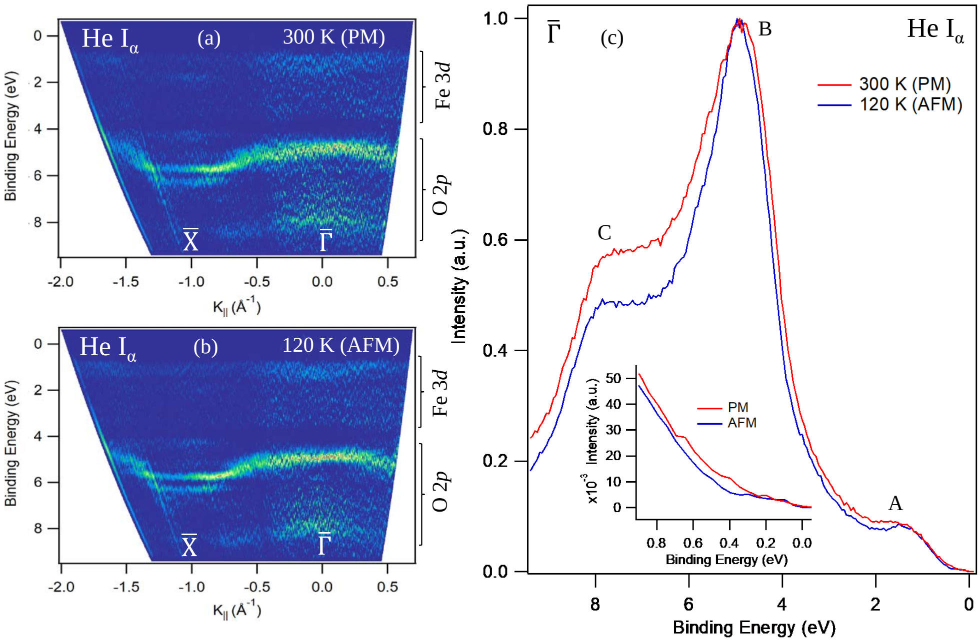

Figure 7.11: (a)-(b) Temperature dependent 2nd derivatives of ARPES band dispersions of 10 ML Fe$_x$O on 5 ML MgO/Ag(001) using He I$_\alpha$ towards $\overline{\Gamma} - \overline{X}$ direction. (c) Angle-resolved energy distribution curve at $\overline{\Gamma}$ for both PM and AFM phase.

Fig. 7.11(a)-(b) show the ARPES band dispersions (second derivatives) along $\overline{\Gamma} - \overline{X}$ direction of 10 ML Fe$_x$O(001) film grown on 5 ML MgO/Ag(001) using He I$_\alpha$ at both paramagnetic (300 K) and antiferromagnetic phases (120 K), respectively. The density of states within 0-3 eV binding energy range are of Fe 3d origin whereas the intense O 2p bands are visible in the 4-8 eV binding energy region. Upon cooling down to 120 K, no major changes in the band dispersions have been observed except the small band narrowing at low temperature. The density of states corresponding to Fe 3d are bit narrower at 120 K and forms a weakly dispersing and low intensity band about 1.5 eV below Fermi level. The O 2p bands also get narrower at 120 K relative to 300 K. The band narrowing is clearly shown in Fig. 7.11(c) using the

ARPES energy distribution curves at $\overline{\Gamma}$ for both 300 K and 120 K temperatures. All the features A, B, and C are narrower with reduced peak width at 120 K, possibly due to the reduced phononic contribution. Moreover, a gap of ~0.1 eV at the valence band-edge [see the inset of Fig. 7.11(c)] indicates the enhanced insulating nature of Fe_xO at low temperature is consistent with the paramagnetic to antiferromagnetic transition. Apart from the persistence of short-range antiferromagnetic order above T_N, the presence of Fe^{2+} vacancy induced Fe^{3+} ions can leads to ferromagnetic interaction between Fe^{2+} and Fe^{3+} as well. Despite the absence of exchange scattered half-order spots it is expected that there exists an antiferromagnetic ordering as suggested our ARPES results as well as the bulk magnetic property studies in the literature. Moreover, almost identical band structure was observed for both PM and AFM phases in presence of long-range AFM order in prototype systems such as NiO and CoO supports our findings [56, 57]. The exchange scattered LEED intensities strongly depends on the arrangement of magnetic moments as well as on the surface crystal structures. Moreover, the Fe^{2+} vacancy-induced ferromagnetic interaction can also lead to the noncollinear spin arrangement near the vacancy sites. Further experiments and theoretical calculations are necessary for a complete understanding of this system.

7.4 Summary

The growth of Fe_xO film on Ag(001) has been performed at different growth and post-growth treatment conditions to obtain the well-ordered Fe_xO film with minimum Fe^{2+} deficiency. The growth at 473 K substrate temperature and 5×10^{-8} mbar oxygen partial pressure show under stoichiometric Fe_xO film with diffuse p(1×1) LEED pattern. The stoichiometry improves significantly upon post-growth oxygen annealing at higher temperature and oxygen partial pressure, however, there appears different superstructure depending upon the post-growth treatments. The coverage dependent XPS and LEED study reveals the under stoichiometric features at low film coverage and the strained p(1×1) LEED pattern at higher coverages, respectively. The stoichiometry of the 9 ML Fe_xO film has been estimated using the Fe $3p$ spectra considering both Fe^{2+} and Fe^{3+} contributions. The estimated stoichiometry is found to be $Fe_{0.84}O$ and is consistent with the Fe $2p$ core levels and the corresponding satellite positions as well. Further, Fe_xO was grown on 5 ML MgO/Ag(001) to investigate the effects of MgO spacer layers on the growth of Fe_xO overlayers. Here, all the growth were performed at 473 K with an oxygen background pressure of 7×10^{-9} mbar. The coverage dependent LEED and XPS study show the well-ordered p(1×1) pattern and improved stoichiometry ($Fe_{0.92}O$) with enhanced Fe^{2+} shake-up satellite intensity, respectively. The Fe_xO/MgO interface chemistry was probed by the evolution of Mg $1s$ core level with Fe_xO film coverage. Temperature dependent ARPES results show no major changes in the band dispersion except the band-edge shift at the low temperature which is an indication of paramagnetic to antiferromagnetic transition. In addition to that, there might be Fe^{2+} vacancy induced ferromagnetic interaction between Fe^{2+} and Fe^{3+} making the magnetic behavior even more complex. Further experiments and theoretical calculations considering the Fe^{2+} vacancies are necessary to understand more insight of the magnetic behavior of Fe_xO.

8

Incommensurate growth of Co on Ag(111)

8.1 Introduction

Study of magnetic thin films since last few decades has been an area of immense interest due to its technological applications. Magnetic thin film in the monolayer regime shows enhanced magnetic moments at the surface and interfaces relative to the bulk moments of the material. Thin layer of ferromagnetic Co is a promising candidate for its potential use like magnetic sensor in the magnetic storage technology [40] *etc.* Moreover, strong out of plane magnetic anisotropy opens up its magneto-optical applications [41, 42]. However, to utilize these properties one has to better understanding of the crystalline structure of the film and the interfaces. Growths of ultrathin Co film on several closed pack polar substrates are controversially described by several groups. At low coverage, two atomic layered polygonal islands of Co on Au(111) and subsequent lateral growth with increasing film coverage was studied by Scanning Tunneling Microscopy (STM) [43]. A temperature dependent growth shows three different shapes of islands of Co on Pd(111) in the different temperature range at low coverages [44]. The Pulsed laser deposition study [46] of Co/Cu(111) system describes the layer-by-layer face centered cubic (fcc) growth of Co up to 6 ML coverage, above this critical coverage, growth exhibits a structural phase transition from fcc to more energetically favorable hexagonal close packed (hcp) structure.

There are several studies available on the structural evolution and magnetic behavior of Co film on Ag(001) surface [231–233]. However, there is only one report [45] available on the growth and structural evolution of Co on Ag(111) to the best of our knowledge. They have shown an incommensurate low temperature growth of Co/Ag(111) up to 2 ML film coverage with corrugated Moiré pattern, with increasing coverage, commensurate growth was observed with decreasing Moiré reconstructions. Here, we have shown the incommensurate growth of Co thin film on Ag(111) and the evolution of the surface geometric structure of the film with increasing coverage using LEED and XPS studies. The core level electronic structure was investigated by XPS study. To investigate the valence band electronic structure of the film, coverage dependent ARPES experiments were performed at $\overline{\Gamma}$ of the surface Brillouin zone of the Co(111) film.

8.1.1 Coverage dependent LEED study

All the experiments were performed in an ultrahigh vacuum (UHV) system having a base pressure better than 8×10^{-11} mbar. Different coverages of Co films were grown on clean Ag(111) single crystal at room temperature (RT) in the similar manner as described for the oxide growth earlier in the chapter. The evolution of LEED pattern with increasing film coverage is shown in Fig. 8.1. A well-ordered p(1×1) incommensurate LEED pattern was observed for 1 ML Co film on Ag(111) as there is a relatively less intense extra spot at a larger distance from the center of the surface Brillouin zone with respect to the p(1×1) pattern. These low intense extra spots correspond to the Co overlayer deposited on clean Ag(111) because the smaller surface lattice parameter of hcp Co(0001) plane (2.51 Å) in reciprocal space will be in a longer distance than the Ag(111) surface lattice parameter (2.89 Å). A closer inspection of the lower film coverage (up to 2 ML) reveals the 6-fold Moiré reconstructions around each Ag spot [see the inset of Fig. 8.1(a)]. Similar Moirè structures were already observed in several Co growth studies on different substrates [45, 234]. They have observed a Co bilayer islands growth with the orientation of (0001) facet parallel to the surface. These incommensurate islands growth resulting in the 6-fold Moirè pattern influenced by the underlying Ag(111) substrate. The lattice strain-field causes

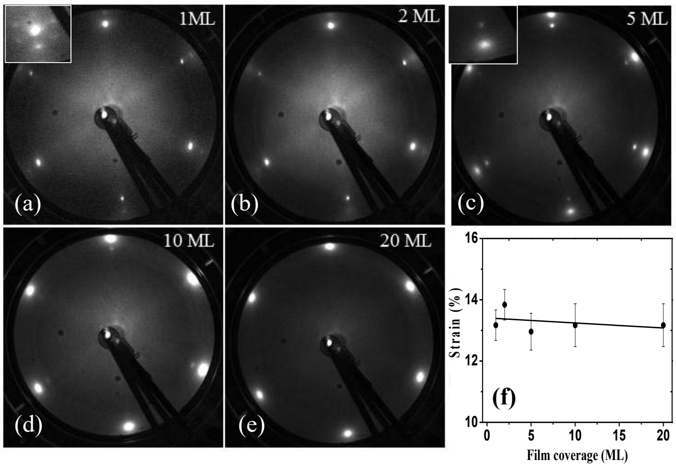

Figure 8.1: Fig. (a)-(e) represents the coverage dependent LEED study at 65 eV primary beam energy. Up to 2 ML coverage, 6-fold Moiré patterns were observed at high gain and exposure time [inset of Fig. 8.1(a)]. Above 2 ML coverage, no Moiré pattern was observed [inset of Fig. 8.1(c)] but the Ag spots were observed till 10 ML film coverage. (f) Surface lattice strain (lattice misfit) was plotted as a function of film coverage. Almost a constant strain (13%) was found in the whole range of film coverage.

a periodic height undulation of the sub-angstrom regime of the film in the low film coverage which may also cause the formation of 6-fold Moiré reconstructions. Beyond 2 ML coverage, no such 6-fold patterns were observed even at maximum gain and exposure time [see the inset of Fig. 8.1(c)]. With increasing Co coverage, the intensity of these spots enhanced and the inner Ag spots intensity gradually attenuates. After 10 ML, Ag spots completely attenuate, i.e., the Co layers wet the whole Ag(111) surface along with bulk-like 3D islands growth. This non-pseudomorphic growth can be understood using the lattice strain measured from the relative position shift of the spots with incident electron beam energy. Almost a constant strain (13%) [Fig.

8.1(f)] in the whole coverage range and a bulk-like relaxed growth from the first ML itself supports the non-pseudomorphic growth.

8.1.2 Coverage dependent XPS study

The role of surface structure and kinetics in the growth of Co films on Ag(111) substrate is an important aspect need to be addressed to understand the growth mechanism properly. A simple consideration of surface diffusion and surface free-energy differences explains why a layer-by-layer growth is unlikely to occur for this system [231]. The bimetallic interface chemistry and the electronic structure can be substantially modified in reduced dimensions relative to the bulk counterpart. The core level XPS measurements were performed to investigate the electronic structure and growth mode of ultrathin Co film on Ag (111). The binding energy positions of the Co $2p_{3/2}$ and Co $2p_{1/2}$ doublets at 778.4 and 793.3 eV, respectively with a spin-orbit splitting of 14.9 eV [Fig. 8.2(a)] are in good agreement with the literature [235]. Further, the well-shaped Co $2p$ doublet, without any satellite ruled out the possibility of Co-Ag alloy formation at RT unlike the case of Mn/Ag(001) system [236]. The coverages of the films were estimated using XPS [237]. The estimated film coverage is quite consistent with the deposited coverage up to 10 ML as shown in Fig. 8.2(b). Beyond this coverage, they deviate due to the finite mean free path, which is a function of the kinetic energy of the photoelectron. Despite the coverage consistency, we cannot conclude here about the growth mode as the photoemission intensity provides the collective information from the macroscopic sample surface. The XPS data can also provide further insights into the growth of Co on Ag(111). The relative area under the curve of Co $2p_{3/2}$ increases almost linearly up to 5 ML [see the inset of Fig. 8.2(b)]. Simultaneously, the curve for Ag $3d_{5/2}$ decreases linearly till 5 ML. In case of typical layer-by-layer growth, one expects to have breaks in the slope during completion of each monolayer or when the growth mode changes from one to

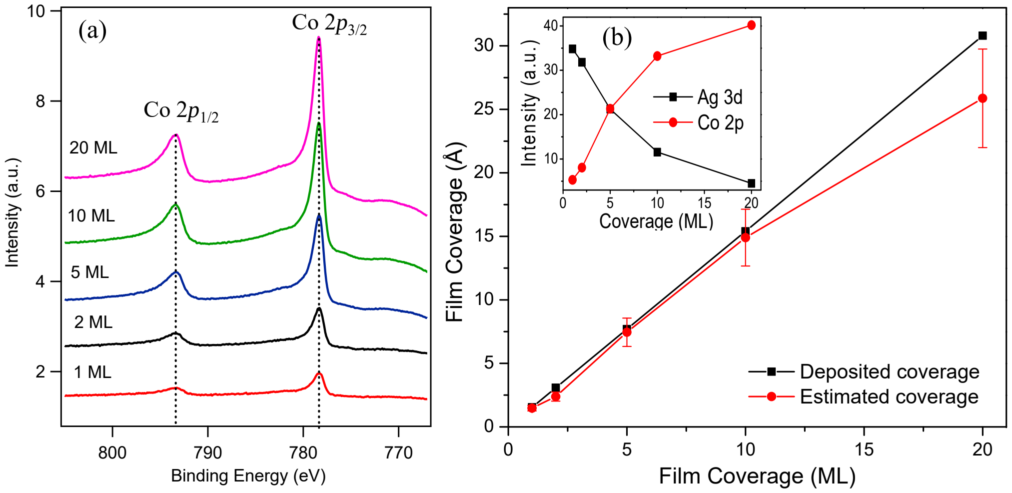

Figure 8.2: (a) Coverage dependent XPS study using monochromatic Al K_α, 1486.7 eV. (b) Comparison of coverage measured by XPS and deposited coverage. The intensity variation of Co $2p_{3/2}$ and Ag $3d_{5/2}$ with film coverage are shown in the inset.

another [238]. Thus, the smooth intensity variation with the absence of any sharp breaks in the slope suggests a similar growth mode at least up to 5 ML. Above 5 ML coverage, the Ag signal drops discontinuously with Co coverage and almost vanishes around 20 ML coverage. Simultaneously, the intensity of the Co $2p_{3/2}$ increases up to a coverage of 20 ML where the intensity reaches almost its saturation value since the Co film has become substantially thicker than the photoelectron mean free path. The overall nature of the growth curves appears to differ from the layer-by-layer growth mode. Even though XPS is not very conclusive in this regard, LEED also suggested the non-pseudomorphic bulk-like 3D islands growth. Microscopic studies are necessary to look into the more details of the growth mechanism which is beyond the scope of this thesis.

8.1.3 Valence band electronic structure: ARPES study

The controlled fabrication of elemental materials offers new phases that either do not exist in nature or that exist only under extreme conditions of temperature and pressure. These new phases have a significant interest in both scientific and technological fields due to their exotic electronic and magnetic properties. Bulk Co has hexagonal closed pack (hcp) structure at RT and transforms into the face-centered cubic (fcc) structure above 700 K [239], accompanied by the drastic change of the magneto-crystal anisotropy. Investigating electronic structure of fcc Co using ARPES is extremely difficult at such a high temperature. Thus by growing fcc Co films, one can study the electronic structure using spin and momentum resolved photoemission spectroscopy at RT. We have probed the valence band electronic structure of Co(111) film using ARPES with He I_α (21.2 eV) photons. The second derivative of the ARPES data, extracted following Zhang *et al.* [148] for a better visualization of the weakly dispersive features. The band dispersion along $\overline{\Gamma}$-$\overline{K}$ direction of 5 ML Co on Ag (111) is shown in Fig. 8.3(a). Near Fermi level, Co 3*d* valence band splits up into two bands at the most symmetric $\overline{\Gamma}$ point of the surface Brillouin zone of Co(111). The spectral features corresponding to these bands are assigned as 'A' and 'B' in as shown in Fig. 8.3(b) using ARPES spectra at $\overline{\Gamma}$ point. The feature 'A' indicates the beginning of the Fermi edge, appears in the surface photoemission from electronic states right at E_F. It is also important to mention that the presence of the feature 'A' near 0.2 eV indicates the formation of well-ordered Co layers since Heimann *et al.* [240] have found that this feature is absent in polycrystalline Co. The feature 'B' is originated due to the direct transition to the photoemission final state from the initial majority-spin *d* bands [240]. The energy gap of 0.7 eV between the band feature 'A' and 'B' seems consistent with the magnetic exchange splitting of 1 layer of Co on Cu(111) at $\overline{\Gamma}$ point [241]. Further, the magnetic exchange splitting (0.85 ± 0.02 eV) of upper *d* band at $\overline{\Gamma}$ point of Co(0001) single crystal is also close to our observed value [242]. This clearly indicates that magnetic exchange splitting of 5 ML Co on Ag(111) is similar to that of the bulk Co as both hcp and fcc are closed pack structure. Ag 4*d* bands are visible within 4 to 6 eV below the Fermi level with a strong contribution from the exposed area of Ag(111) surface. Intensity behaviors

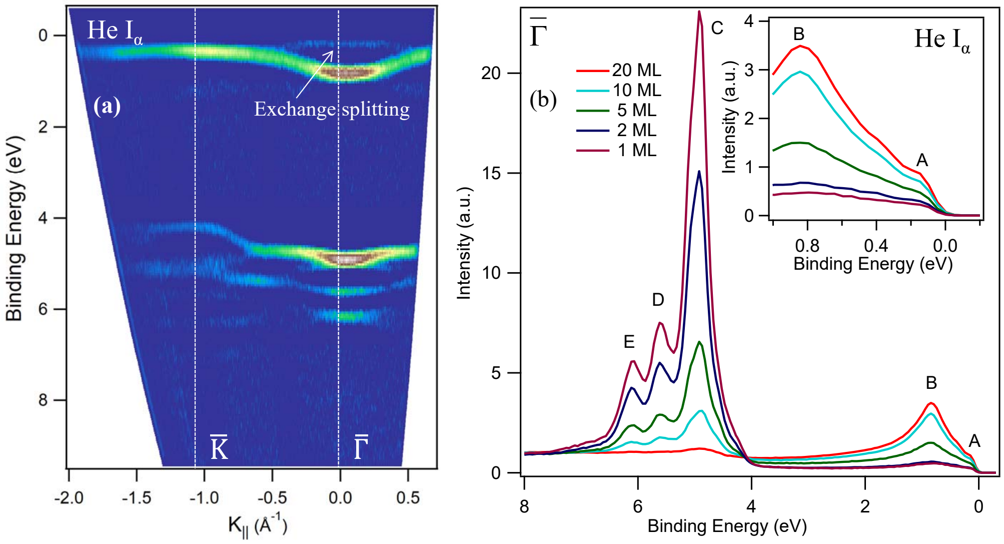

Figure 8.3: (a) ARPES band mapping of 5 ML Co/Ag(111) using He I$_\alpha$ (21.2 eV). Magnetic exchange splitting (0.7 eV) of Co 3d was observed at $\overline{\Gamma}$. (b) ARPES spectra at $\overline{\Gamma}$ for different film coverages. Zoomed-in view of the features 'A' and 'B', near Fermi level are shown in the inset.

of these bands with increasing film coverage are shown in Fig. 8.3(b). Three features in the Ag 4d band specified by 'C', 'D', 'E' which are gradually decreasing with increasing Co coverage, as Ag get buried for higher film coverage, conversely Co 3d bands get enhanced with increasing film coverage. So, the presence of intense Ag bands even at 5 ML Co coverage suggests that it is not a layer-by-layer growth as observed in LEED.

8.2 Summary

In this chapter, growth and electronic structure of Co metal on close packed Ag(111) has been investigated. The incommensurate well-ordered growth of Co film on Ag(111) surface was studied by LEED, XPS, and ARPES techniques. For lower film coverages, we observed an incommensurate $p(1 \times 1)$ LEED with the formation of 6-fold Moiré patterns. At higher coverage, bulk-like 3D islands growth was observed as it takes 10

ML Co to wet the Ag(111) surface completely. For a better understanding of the growth mechanism, one has to use microscopic techniques like Scanning Tunneling Microscopy (STM). A systematic coverage dependent XPS study confirms the well-ordered growth without any inter-diffusion or surface alloying between the film and the substrate. Valence band electronic structure of Co(111) film shows the magnetic exchange splitting (0.7 eV) of Co $3d$ band at $\overline{\Gamma}$ point.

Bibliography

[1] Heiler, M., Chassé, A., Schindler, K.-M., Hollering, M., and Neddermeyer, H. *Surface Science* **454**, 36–40 (2000).

[2] Sindhu, S., Heiler, M., Schindler, K.-M., Widdra, W., and Neddermeyer, H. *Surface Science* **566**, 471–475 (2004).

[3] Cheng, C.-M., Wang, C.-C., Jeng, H.-T., Hsue, C., Hsu, B., Huang, D.-J., and Tsuei, K.-D. *Physica B: Condensed Matter* **403**(5), 1539–1541 (2008).

[4] Yang, S., Seong, S., and Kim, J. *Journal of the Korean Physical Society* **57**(5), 1312–1316 (2010).

[5] Das, J. and Menon, K. S. *Journal of Electron Spectroscopy and Related Phenomena* **203**, 71–74 (2015).

[6] Kundu, A. K., Barman, S., and Menon, K. S. *Physical Review B* **96**(19), 195116 (2017).

[7] Freund, H.-J., Heyde, M., Nilius, N., Schauermann, S., Shaikhutdinov, S., and Sterrer, M. *Journal of Catalysis* **308**, 154–167 (2013).

[8] Tasker, P. *Journal of Physics C: Solid State Physics* **12**(22), 4977 (1979).

[9] Noguera, C. *Journal of Physics: Condensed Matter* **12**(31), R367 (2000).

[10] Hassel, M. and Freund, H.-J. *Surface Science* **325**(1-2), 163–168 (1995).

[11] Mocuta, C., Barbier, A., and Renaud, G. *Applied Surface Science* **162**, 56–61 (2000).

[12] Bednorz, J. G. and Müller, K. A. *Zeitschrift für Physik B Condensed Matter* **64**(2), 189–193 (1986).

[13] Mott, N. F. *Proceedings of the Physical Society. Section A* **62**(7), 416 (1949).

[14] Terakura, K., Williams, A. R., Oguchi, T., and Kübler, J. *Physical Review Letters* **52**, 1830–1833 May (1984).

[15] Bredow, T. and Gerson, A. R. *Physical Review B* **61**, 5194–5201 Feb (2000).

[16] Van Elp, J., Wieland, J., Eskes, H., Kuiper, P., Sawatzky, G., De Groot, F., and Turner, T. *Physical Review B* **44**(12), 6090 (1991).

[17] Roth, W. *Physical Review* **110**(6), 1333 (1958).

[18] Rechtin, M. and Averbach, B. *Physical Review B* **5**(7), 2693 (1972).

[19] Hillebrecht, F., Ohldag, H., Weber, N., Bethke, C., Mick, U., Weiss, M., and Bahrdt, J. *Physical Review Letters* **86**(15), 3419 (2001).

[20] Gao, C., Wulfhekel, W., and Kirschner, J. *Physical Review Letters* **101**(26), 267205 (2008).

[21] Wulfhekel, W. and Gao, C. *Journal of Physics: Condensed Matter* **22**(8), 084021 (2010).

[22] Menon, K. S. R., Mandal, S., Das, J., Menteş, T. O., Niño, M. A., Locatelli, A., and Belkhou, R. *Physical Review B* **84**, 132402 Oct (2011).

[23] Palmberg, P., DeWames, R., and Vredevoe, L. *Physical Review Letters* **21**(10), 682 (1968).

[24] Das, J. and Menon, K. S. *Journal of Magnetism and Magnetic Materials* **449**, 415–422 (2018).

[25] Das, J., Kundu, A. K., and Menon, K. S. *Vacuum* **112**, 5–11 (2015).

[26] Das, J. *Advanced Science Letters* **22**(1) (2016).

[27] Palmberg, P., De Wames, R., Vredevoe, L., and Wolfram, T. *Journal of Applied Physics* **40**(3), 1158–1163 (1969).

[28] Hanf, M., Krembel, C., Bolmont, D., and Gewinner, G. *Physical Review B* **68**(14), 144419 (2003).

[29] Altieri, S., Finazzi, M., Hsieh, H., Haverkort, M., Lin, H.-J., Chen, C., Frabboni, S., Gazzadi, G., Rota, A., Valeri, S., et al. *Physical Review B* **79**(17), 174431 (2009).

[30] Zaanen, J., Sawatzky, G., and Allen, J. *Physical Review Letters* **55**(4), 418 (1985).

[31] Anderson, P. W. In *Solid State Physics*, volume 14, 99–214. Elsevier (1963).

[32] Duffy, D. and Stoneham, A. *Journal of Physics C: Solid State Physics* **16**(21), 4087 (1983).

[33] Altieri, S., Tjeng, L., Voogt, F., Hibma, T., and Sawatzky, G. *Physical Review B* **59**(4), R2517 (1999).

[34] Yang, S., Park, H.-K., Kim, J.-S., Phark, S.-H., Chang, Y. J., Noh, T., Hwang, H.-N., Hwang, C.-C., and Kim, H.-D. *Surface Science* **616**, 12–18 (2013).

[35] Wollschläger, J., Erdös, D., and Schröder, K.-M. *Surface Science* **402**, 272–276 (1998).

[36] Altieri, S., Tjeng, L., and Sawatzky, G. *Physical Review B* **61**(24), 16948 (2000).

[37] Butti, G., Trioni, M., and Ishida, H. *Physical Review B* **70**(19), 195425 (2004).

[38] Droubay, T. C., Chambers, S. A., Joly, A. G., Hess, W. P., Németh, K., Harkay, K. C., and Spentzouris, L. *Physical Review Letters* **112**(6), 067601 (2014).

[39] Hazen, R. M. and Jeanloz, R. *Reviews of Geophysics* **22**(1), 37–46 (1984).

[40] Hylton, T. *Applied Physics Letters* **62**(19), 2431–2433 (1993).

[41] Zeper, W., Greidanus, F., Carcia, P., and Fincher, C. *Journal of Applied Physics* **65**(12), 4971–4975 (1989).

[42] Ferré, J., Pénissard, G., Marlière, C., Renard, D., Beauvillain, P., and Renard, J. *Applied Physics Letters* **56**(16), 1588–1590 (1990).

[43] Voigtländer, B., Meyer, G., and Amer, N. M. *Physical Review B* **44**(18), 10354 (1991).

[44] Wasniowska, M., Janke-Gilman, N., Wulfhekel, W., Przybylski, M., and Kirschner, J. *Surface Science* **601**(14), 3073–3081 (2007).

[45] Morgenstern, K., Kibsgaard, J., Lauritsen, J. V., Lægsgaard, E., and Besenbacher, F. *Surface Science* **601**(9), 1967–1972 (2007).

[46] Zheng, M., Shen, J., Barthel, J., Ohresser, P., Mohan, C. V., and Kirschner, J. *Journal of Physics: Condensed Matter* **12**(6), 783 (2000).

[47] Soriaga, M. P. *Thin Films: Preparation, Characterization, Applications: Preparation, Characterization, Applications.* Springer Science & Business Media, (2002).

[48] Goniakowski, J., Finocchi, F., and Noguera, C. *Reports on Progress in Physics* **71**(1), 016501 (2007).

[49] Duò, L., Finazzi, M., and Ciccacci, F. *Magnetic Properties of Antiferromagnetic Oxide Materials: Surfaces, Interfaces, and Thin Films.* John Wiley & Sons, (2010).

[50] Bach, H. and Krause, D. *Thin Films on Glass.* Springer Science & Business Media, (2013).

[51] Messier, R. *Journal of Vacuum Science & Technology A* **4**(3), 490–495 (1986).

[52] Zaanen, J., Sawatzky, G., and Allen, J. *Physical Review Letters* **55**(4), 418 (1985).

[53] Brookes, N., Law, D.-L., Warburton, D., Wincott, P., and Thornton, G. *Journal of Physics: Condensed Matter* **1**(26), 4267 (1989).

[54] Anisimov, V. I., Zaanen, J., and Andersen, O. K. *Physical Review B* **44**(3), 943 (1991).

[55] Terakura, K., Oguchi, T., Williams, A., and Kübler, J. *Physical Review B* **30**(8), 4734 (1984).

[56] Shen, Z.-X., Allen, J. W., Lindberg, P. A. P., Dessau, D. S., Wells, B. O., Borg, A., Ellis, W., Kang, J. S., Oh, S.-J., Lindau, I., and Spicer, W. E. *Physical Review B* **42**, 1817–1828 Jul (1990).

[57] Shen, Z.-X., Shih, C. K., Jepsen, O., Spicer, W. E., Lindau, I., and Allen, J. W. *Physical Review Letters* **64**, 2442–2445 May (1990).

[58] Anderson, P. W. *Physical Review* **115**(1), 2 (1959).

[59] Hubbard, J. *Proc. R. Soc. Lond. A* **276**(1365), 238–257 (1963).

[60] Anderson, P. W. *Science* **235**(4793), 1196–1198 (1987).

[61] Das, J. *Electronic and Magnetic Structures of Antiferromagnetic Thin Films*. PhD thesis, (2015).

[62] Lang, X., Zheng, W., and Jiang, Q. *Physical Review B* **73**(22), 224444 (2006).

[63] Li, Y. and Baberschke, K. *Physical Review Letters* **68**(8), 1208 (1992).

[64] Huang, F., Kief, M., Mankey, G., and Willis, R. *Physical Review B* **49**(6), 3962 (1994).

[65] Van der Zaag, P., Ijiri, Y., Borchers, J., Feiner, L., Wolf, R., Gaines, J., Erwin, R., and Verheijen, M. *Physical Review Letters* **84**(26), 6102 (2000).

[66] Bloch, D. *Journal of Physics and Chemistry of Solids* **27**(5), 881–885 (1966).

[67] Massey, M., Chen, N., Allen, J., and Merlin, R. *Physical Review B* **42**(13), 8776 (1990).

[68] Zhang, W.-B., Hu, Y.-L., Han, K.-L., and Tang, B.-Y. *Physical Review B* **74**(5), 054421 (2006).

[69] Abarra, E., Takano, K., Hellman, F., and Berkowitz, A. *Physical Review Letters* **77**(16), 3451 (1996).

[70] Mills, D. *Physical Review B* **3**(11), 3887 (1971).

[71] Hofmann, P. *Surface Physics: An Introduction.* Philip Hofmann, (2013).

[72] Seah, M. P. and Dench, W. *Surface and Interface Analysis* **1**(1), 2–11 (1979).

[73] Vanhove, M. A., Weinberg, W. H., and Chan, C.-M. *Low-Energy Electron Diffraction: Experiment, Theory and Surface Structure Determination*, volume 6. Springer Science & Business Media, (2012).

[74] Wood, E. A. *Journal of Applied Physics* **35**(4), 1306–1312 (1964).

[75] Damascelli, A., Hussain, Z., and Shen, Z.-X. *Reviews of Modern Physics* **75**(2), 473 (2003).

[76] Hüfner, S. *Very High Resolution Photoelectron Spectroscopy*, volume 715. Springer, (2007).

[77] Kevan, S. D. *Angle-Resolved Photoemission: Theory and Current Applications*, volume 74. Elsevier, (1992).

[78] Hüfner, S. *Photoelectron Spectroscopy: Principles and Applications.* Springer Science & Business Media, (2013).

[79] Reinert, F. and Hüfner, S. *New Journal of Physics* **7**(1), 97 (2005).

[80] Hertz, H. *Annalen der Physik* **267**(8), 983–1000 (1887).

[81] Einstein, A. *Annalen der Physik* **322**(6), 132–148 (1905).

[82] Nordling, C., Sokolowski, E., and Siegbahn, K. *Physical Review* **105**, 1676–1677 (1957).

[83] Siegbahn, K. *Philosophical Transactions of the Royal Society of London. Series A, Mathematical and Physical Sciences* **268**(1184), 33–57 (1970).

[84] Berglund, C. N. and Spicer, W. E. *Physical Review* **136**, A1030–A1044 Nov (1964).

[85] Chiang, T.-C. *Surface Science Reports* **39**(7), 181–235 (2000).

[86] Doniach, S. and Sunjic, M. *Journal of Physics C: Solid State Physics* **3**(2), 285 (1970).

[87] Christmann, K. *Berichte der Bunsengesellschaft für physikalische Chemie* **93**(1), 104–105 (1989).

[88] Mahatha, S. and Menon, K. S. *Current Science (00113891)* **98**(6) (2010).

[89] Lüth, H. *Surfaces and Interfaces of Solid Materials.* Springer Science & Business Media, (2013).

[90] Liu, Y. *Angle-Resolved Photoemission Studies of Two-Dimensional Electron Systems.* University of Illinois at Urbana-Champaign, (2010).

[91] Lüth, H. *Solid Surfaces, Interfaces and Thin Films*, volume 4. Springer, (2001).

[92] Ezpeleta, A. M. *Electronic Structure of Low-Dimentional System Analyzed by Angle-Resolved Photoemission Spectroscopy.* PhD thesis, Donostia, (2002).

[93] `https://www.lesker.com/newweb/deposition_materials/materialdepositionchart.cfm?pgid=0`.

[94] Detian, L. and Yongjun, C. *Vacuum* **85**(7), 739–743 (2011).

[95] Moghadam, A. H., Dashtizad, V., Kaflou, A., and Yoozbashizadeh, H. *Vacuum* **111**, 9–14 (2015).

[96] Guidotti, R., Atkinson, G., and Wong, M. *Journal of the Less Common Metals* **52**(1), 13–28 (1977).

[97] Logothetis, E., Park, K., Meitzler, A., and Laud, K. *Applied Physics Letters* **26**(4), 209–211 (1975).

[98] Moussa, S., Abdelsayed, V., and El-Shall, M. S. *Chemical Physics Letters* **510**(4), 179–184 (2011).

[99] Lu, A., Chen, Y., Zeng, D., Li, M., Xie, Q., Zhang, X., and Peng, D.-L. *Nanotechnology* **25**(3), 035707 (2014).

[100] Mackay, J. L. and Henrich, V. E. *Physical Review B* **39**(9), 6156 (1989).

[101] Gorschlüter, A. and Merz, H. *Physical Review B* **49**(24), 17293 (1994).

[102] Tjernberg, O., Chiaia, G., Karlsson, U., and De Groot, F. *Journal of Physics: Condensed Matter* **9**(45), 9863 (1997).

[103] Wdowik, U. D. and Parlinski, K. *Physical Review B* **75**(10), 104306 (2007).

[104] Sebastian, I. and Neddermeyer, H. *Surface Science* **454**, 771–777 (2000).

[105] Shantyr, R., Hagendorf, C., and Neddermeyer, H. *Thin Solid Films* **464**, 65–75 (2004).

[106] Hagendorf, C., Shantyr, R., Meinel, K., Schindler, K.-M., and Neddermeyer, H. *Surface Science* **532**, 346–350 (2003).

[107] Sebastian, I., Bertrams, T., Meinel, K., and Neddermeyer, H. *Faraday Discussions* **114**, 129–140 (1999).

[108] Sindhu, S., Heiler, M., Schindler, K.-M., and Neddermeyer, H. *Surface Science* **541**(1), 197–206 (2003).

[109] Allegretti, F., Parteder, G., Gragnaniello, L., Surnev, S., Netzer, F., Barolo, A., Agnoli, S., Granozzi, G., Franchini, C., and Podloucky, R. *Surface Science* **604**(5), 529–534 (2010).

[110] Gragnaniello, L., Agnoli, S., Parteder, G., Barolo, A., Bondino, F., Allegretti, F., Surnev, S., Granozzi, G., and Netzer, F. *Surface Science* **604**(21), 2002–2011 (2010).

[111] Gubo, M., Ebensperger, C., Meyer, W., Hammer, L., Heinz, K., Mittendorfer, F., and Redinger, J. *Physical Review Letters* **108**(6), 066101 (2012).

[112] Kundu, A. K. and Menon, K. S. *Surface Science* **659**, 43–51 (2017).

[113] Bertrams, T. and Neddermeyer, H. *Journal of Vacuum Science & Technology B: Microelectronics and Nanometer Structures Processing, Measurement, and Phenomena* **14**(2), 1141–1144 (1996).

[114] Caffio, M., Cortigiani, B., Rovida, G., Atrei, A., and Giovanardi, C. *The Journal of Physical Chemistry B* **108**(28), 9919–9926 (2004).

[115] Giovanardi, C., Di Bona, A., and Valeri, S. *Physical Review B* **69**(7), 075418 (2004).

[116] Torelli, P., Soares, E., Renaud, G., Valeri, S., Guo, X., and Luches, P. *Surface Science* **601**(13), 2651–2655 (2007).

[117] Wollschläger, J., Erdös, D., and Schröder, K.-M. *Surface Science* **402**, 272–276 (1998).

[118] Zhang, X., Pashley, D., Neave, J., Hart, L., and Joyce, B. *Journal of Applied Physics* **78**(11), 6454–6457 (1995).

[119] Langell, M., Anderson, M., Carson, G., Peng, L., and Smith, S. *Physical Review B* **59**(7), 4791 (1999).

[120] Carson, G., Nassir, M., and Langell, M. *Journal of Vacuum Science & Technology A* **14**(3), 1637–1642 (1996).

[121] Petitto, S. C., Marsh, E. M., Carson, G. A., and Langell, M. A. *Journal of Molecular Catalysis A: Chemical* **281**(1), 49–58 (2008).

[122] Padmore, T., Thornton, G., and Padmore, H. *Vacuum* **38**(4-5), 261–265 (1988).

[123] Krembel, C., Hanf, M., Peruchetti, J., Bolmont, D., and Gewinner, G. *Physical Review B* **44**(20), 11472 (1991).

[124] Thornton, G., Brookes, N., L-Law, D., Warburton, D., and Wincott, P. *Physica Scripta* **41**(4), 625 (1990).

[125] Meyer, W., Biedermann, K., Gubo, M., Hammer, L., and Heinz, K. *Physical Review B* **79**(12), 121403 (2009).

[126] Heimann, P., Neddermeyer, H., and Roloff, H. *Journal of Physics C: Solid State Physics* **10**(1), L17 (1977).

[127] Colbourn, E. A. *Surface Science Reports* **15**(8), 281–319 (1992).

[128] Henrich, V. and Cox, P. *The Surface Science of Oxides.* Cambridge University Press, Cambridge, (1994).

[129] Chambers, S. A. *Surface Science Seports* **39**(5), 105–180 (2000).

[130] Pacchioni, G. and Freund, H. *Chemical Reviews* **113**(6), 4035–4072 (2012).

[131] Freund, H.-J. and Pacchioni, G. *Chemical Society Reviews* **37**(10), 2224–2242 (2008).

[132] Netzer, F. P., Allegretti, F., and Surnev, S. *Journal of Vacuum Science & Technology B, Nanotechnology and Microelectronics: Materials, Processing, Measurement, and Phenomena* **28**(1), 1–16 (2010).

[133] Yadavalli, S., Yang, M., and Flynn, C. *Physical Review B* **41**(11), 7961 (1990).

[134] Park, Y., Fullerton, E. E., and Bader, S. *Journal of Vacuum Science & Technology A: Vacuum, Surfaces, and Films* **13**(2), 301–304 (1995).

[135] Valeri, S., Altieri, S., Di Bona, A., Luches, P., Giovanardi, C., and Moia, T. *Surface Science* **507**, 311–317 (2002).

[136] Pal, J., Smerieri, M., Celasco, E., Savio, L., Vattuone, L., and Rocca, M. *Physical Review Letters* **112**(12), 126102 (2014).

[137] Peterka, D., Tegenkamp, C., Schröder, K.-M., Ernst, W., and Pfnür, H. *Surface Science* **431**(1), 146–155 (1999).

[138] Hesper, R., Tjeng, L., and Sawatzky, G. *EPL (Europhysics Letters)* **40**(2), 177 (1997).

[139] Müller, F., De Masi, R., Steiner, P., Reinicke, D., Stadtfeld, M., and Hüfner, S. *Surface Science* **459**(1), 161–172 (2000).

[140] Wollschläger, J., Erdös, D., Goldbach, H., Höpken, R., and Schröder, K. *Thin Solid Films* **400**(1), 1–8 (2001).

[141] Dynna, M., Vassent, J., Marty, A., and Gilles, B. *Journal of Applied Physics* **80**(5), 2650–2657 (1996).

[142] Das, J., Biswas, S., Kundu, A. K., Narasimhan, S., and Menon, K. S. *Physical Review B* **91**(12), 125435 (2015).

[143] Springholz, G., Bauer, G., and Holy, V. *Surface Science* **365**(2), 453–460 (1996).

[144] Markov, I. *Crystal Growth for Beginners: Fundamentals of Nucleation, Crystal Growth and Epitaxy.* World Scientific, (2003).

[145] Chambers, S., Gao, Y., and Liang, Y. *Surface Science* **339**(3), 297–309 (1995).

[146] Nelin, C. J., Uhl, F., Staemmler, V., Bagus, P. S., Fujimori, Y., Sterrer, M., Kuhlenbeck, H., and Freund, H.-J. *Physical Chemistry Chemical Physics* **16**(40), 21953–21956 (2014).

[147] Nelin, C. J., Bagus, P. S., Brown, M. A., Sterrer, M., and Freund, H.-J. *Angewandte Chemie International Edition* **50**(43), 10174–10177 (2011).

[148] Zhang, P., Richard, P., Qian, T., Xu, Y.-M., Dai, X., and Ding, H. *Review of Scientific Instruments* **82**(4), 043712 (2011).

[149] Shayeganfar, F., Vasu, K., Nair, R., Peeters, F., and Neek-Amal, M. *Physical Review B* **95**(14), 144109 (2017).

[150] Kiguchi, M., Goto, T., Saiki, K., Sasaki, T., Iwasawa, Y., and Koma, A. *Surface Science* **512**(1-2), 97–106 (2002).

[151] Schintke, S., Messerli, S., Pivetta, M., Patthey, F., Libioulle, L., Stengel, M., De Vita, A., and Schneider, W.-D. *Physical Review Letters* **87**(27), 276801 (2001).

[152] Jaouen, T., Jézéquel, G., Delhaye, G., Lépine, B., Turban, P., and Schieffer, P. *Applied Physics Letters* **97**(23), 232104 (2010).

[153] Mattheiss, L. *Physical Review B* **5**(2), 290 (1972).

[154] Brandow, B. *Advances in Physics* **26**(5), 651–808 (1977).

[155] Kunz, A. B. and Surratt, G. *Solid State Communications* **25**(1), 9–12 (1978).

[156] Koiller, B. and Falicov, L. *Journal of Physics C: Solid State Physics* **7**(2), 299 (1974).

[157] Shen, Z.-X., Shih, C., Jepsen, O., Spicer, W., Lindau, I., and Allen, J. *Physical Review Letters* **64**(20), 2442 (1990).

[158] Henrich, V. E. *Reports on Progress in Physics* **48**(11), 1481 (1985).

[159] Freund, H.-J. and Umbach, E. *Adsorption on Ordered Surfaces of Ionic Solids and Thin Films: Proceedings of the 106th WE-Heraeus Seminar, Bad Honnef, Germany, February 15–18, 1993*, volume 33. Springer Science & Business Media, (2013).

[160] Shull, C. G., Strauser, W., and Wollan, E. *Physical Review* **83**(2), 333 (1951).

[161] Magnuson, M., Butorin, S., Guo, J.-H., and Nordgren, J. *Physical Review B* **65**(20), 205106 (2002).

[162] Tomiyasu, K., Inami, T., and Ikeda, N. *Physical Review B* **70**(18), 184411 (2004).

[163] Hiraoka, N., Okamura, H., Ishii, H., Jarrige, I., Tsuei, K., and Cai, Y. *The European Physical Journal B* **70**(2), 157–162 (2009).

[164] El-Batanouny, M. *Journal of Physics: Condensed Matter* **14**(24), 6281 (2002).

[165] Ambrose, T. and Chien, C. *Physical Review Letters* **76**(10), 1743 (1996).

[166] Csiszar, S., Haverkort, M., Hu, Z., Tanaka, A., Hsieh, H., Lin, H.-J., Chen, C., Hibma, T., and Tjeng, L. *Physical Review Letters* **95**(18), 187205 (2005).

[167] Tang, Y., Smith, D. J., Zink, B., Hellman, F., and Berkowitz, A. *Physical Review B* **67**(5), 054408 (2003).

[168] Gotter, R., Offi, F., Ruocco, A., Da Pieve, F., Bartynski, R., Cini, M., and Stefani, G. *EPL (Europhysics Letters)* **94**(3), 37008 (2011).

[169] Marcus-Saubat, B., Beaufils, J., and Barbaux, Y. *Journal de Chimie Physique* **83**, 317–321 (1986).

[170] Norman, M. R. *Physical Review B* **40**, 10632–10634 Nov (1989).

[171] Norman, M. R. *Physical Review Letters* **64**, 1162–1165 Mar (1990).

[172] Ojala, E. J. and Terakura, K. *Physical Review B* **33**(4), 2733 (1986).

[173] Elp, J. *The Electronic Structure of Doped Late Transition Metal Monoxides*. PhD thesis.

[174] Mattheiss, L. *Physical Review B* **5**(2), 306 (1972).

[175] Fujimori, A. and Minami, F. *Physical Review B* **30**, 957–971 Jul (1984).

[176] Fujimori, A., Kimizuka, N., Akahane, T., Chiba, T., Kimura, S., Minami, F., Siratori, K., Taniguchi, M., Ogawa, S., and Suga, S. *Physical Review B* **42**(12), 7580 (1990).

[177] Van Elp, J., Potze, R., Eskes, H., Berger, R., and Sawatzky, G. *Physical Review B* **44**(4), 1530 (1991).

[178] Van Elp, J., Eskes, H., Kuiper, P., and Sawatzky, G. *Physical Review B* **45**(4), 1612 (1992).

[179] Eder, R. *Physical Review B* **78**(11), 115111 (2008).

[180] Oguchi, T., Terakura, K., and Williams, A. R. *Physical Review B* **28**, 6443–6452 Dec (1983).

[181] Hermsmeier, B., Osterwalder, J., Friedman, D., and Fadley, C. *Physical Review Letters* **62**(4), 478 (1989).

[182] Sinković, B., Hermsmeier, B., and Fadley, C. *Physical Review Letters* **55**(11), 1227 (1985).

[183] Nekrasov, I., Pavlov, N., and Sadovskii, M. *Journal of Experimental and Theoretical Physics* **116**(4), 620–634 (2013).

[184] Gillen, R. and Robertson, J. *Journal of Physics: Condensed Matter* **25**(16), 165502 (2013).

[185] Rödl, C., Fuchs, F., Furthmüller, J., and Bechstedt, F. *Physical Review B* **79**, 235114 Jun (2009).

[186] Feng, X. *Physical Review B* **69**, 155107 Apr (2004).

[187] Ibach, H. *Physics of Surfaces and Interfaces*, volume 12. Springer, (2006).

[188] Schrön, A. and Bechstedt, F. *Physical Review B* **92**(16), 165112 (2015).

[189] Kim, K. S. *Physical Review B* **11**, 2177–2185 Mar (1975).

[190] Zhang, W., Koepernik, K., Richter, M., and Eschrig, H. *Physical Review B* **79**(15), 155123 (2009).

[191] Khan, D. and Erickson, R. *Journal of Physics and Chemistry of Solids* **29**(12), 2087–2090 (1968).

[192] Rechtin, M. and Averbach, B. *Physical Review B* **6**(11), 4294 (1972).

[193] Kernavanois, N., Ressouche, E., Brown, P., Henry, J., and Lelievre-Berna, E. *Journal of Physics: Condensed Matter* **15**(20), 3433 (2003).

[194] Desjonqueres, M.-C. and Spanjaard, D. *Concepts in Surface Physics*. Springer Science & Business Media, (2012).

[195] Li, Q., Liang, J., Luo, Y., Ding, Z., Gu, T., Hu, Z., Hua, C., Lin, H.-J., Pi, T., Kang, S., et al. *Scientific Reports* **6**, 22355 (2016).

[196] Borchers, J. A., Carey, M. J., Erwin, R. W., Majkrzak, C. F., and Berkowitz, A. E. *Physical Review Letters* **70**, 1878–1881 Mar (1993).

[197] Borchers, J., Carey, M., Berkowitz, A., Erwin, R., and Majkrzak, C. *Journal of Applied Physics* **73**(10), 6898–6900 (1993).

[198] Altieri, S., Tjeng, L., Voogt, F., Hibma, T., Rogojanu, O., and Sawatzky, G. *Physical Review B* **66**(15), 155432 (2002).

[199] Peacor, S. and Hibma, T. *Surface Science* **301**(1-3), 11–18 (1994).

[200] James, M. and Hibma, T. *Surface Science* **433**, 718–722 (1999).

[201] Giovanardi, C., Di Bona, A., Altieri, S., Luches, P., Liberati, M., Rossi, F., and Valeri, S. *Thin Solid Films* **428**(1-2), 195–200 (2003).

[202] Towler, M., Harrison, N., and McCarthy, M. *Physical Review B* **52**(7), 5375 (1995).

[203] Rota, A., Altieri, S., and Valeri, S. *Physical Review B* **79**(16), 161401 (2009).

[204] Wagner, F. and Ross Jr, P. *Surface Science* **160**(1), 305–330 (1985).

[205] De Santis, M. *Habilitationa diriger des recherches, Institut Néel, CNRS/UJF* **27** (2014).

[206] Rechtin, M., Moss, S., and Averbach, B. *Physical Review Letters* **24**(26), 1485 (1970).

[207] Namikawa, K. *Journal of the Physical Society of Japan* **44**(1), 165–171 (1978).

[208] Prudnikov, P. V., Prudnikov, V. V., and Medvedeva, M. A. *JETP Letters* **100**(7), 446–450 (2014).

[209] Luijten, E., Blöte, H. W., and Binder, K. *Physical Review E* **56**(6), 6540 (1997).

[210] Negovetic, I. and Konstantinović, J. *Solid State Communications* **13**(3), 249–252 (1973).

[211] Corneille, J. S., He, J.-W., and Goodman, D. W. *Surface Science* **338**(1-3), 211–224 (1995).

[212] Somorjai, G. A. and Li, Y. *Introduction to Surface Chemistry and Catalysis.* John Wiley & Sons, (2010).

[213] Mallinson, J. C. *The foundations of magnetic recording.* Elsevier, (2012).

[214] Waddill, G. D. and Ozturk, O. *Surface Science* **575**(1-2), 35–50 (2005).

[215] Abreu, G., Paniago, R., and Pfannes, H.-D. *Journal of Magnetism and Magnetic Materials* **349**, 235–239 (2014).

[216] Merte, L. R., Shipilin, M., Ataran, S., Blomberg, S., Zhang, C., Mikkelsen, A., Gustafson, J., and Lundgren, E. *The Journal of Physical Chemistry C* **119**(5), 2572–2582 (2015).

[217] Kim, K. J., Moon, D. W., Lee, S. K., and Jung, K.-H. *Thin Solid Films* **360**(1-2), 118–121 (2000).

[218] Weiss, W. and Ranke, W. *Progress in Surface Science* **70**(1-3), 1–151 (2002).

[219] Couet, S., Schlage, K., Saksl, K., and Röhlsberger, R. *Physical Review Letters* **101**(5), 056101 (2008).

[220] Roth, W. *Acta Crystallographica* **13**(2), 140–149 (1960).

[221] Koike, K. and Furukawa, T. *Physical Review Letters* **77**, 3921–3924 Oct (1996).

[222] Yamashita, T. and Hayes, P. *Applied Surface Science* **254**(8), 2441–2449 (2008).

[223] Grosvenor, A., Kobe, B., Biesinger, M., and McIntyre, N. *Surface and Interface Analysis* **36**(12), 1564–1574 (2004).

[224] Wagner, C., Davis, L., Zeller, M., Taylor, J., Raymond, R., and Gale, L. *Surface and Interface Analysis* **3**(5), 211–225 (1981).

[225] Ritter, M., Ranke, W., and Weiss, W. *Physical Review B* **57**(12), 7240 (1998).

[226] Meyerheim, H., Popescu, R., Jedrecy, N., Vedpathak, M., Sauvage-Simkin, M., Pinchaux, R., Heinrich, B., and Kirschner, J. *Physical Review B* **65**(14), 144433 (2002).

[227] Hawn, D. D. and DeKoven, B. M. *Surface and Interface Analysis* **10**(2-3), 63–74 (1987).

[228] Oh, H., Lee, S., Seo, J., Min, H., and Kim, J.-S. *Applied Physics Letters* **82**(3), 361–363 (2003).

[229] Dean, J. *Materials and Manufacturing Processes* **5**(4), 687–688 (1990).

[230] Battle, P. and Cheetham, A. *Journal of Physics C: Solid State Physics* **12**(2), 337 (1979).

[231] Zimmermann, C., Yeadon, M., Nordlund, K., Gibson, J., Averback, R., Herr, U., and Samwer, K. *Physical Review Letters* **83**(6), 1163 (1999).

[232] Degroote, B., Dekoster, J., and Langouche, G. *Surface Science* **452**(1-3), 172–178 (2000).

[233] Ortega, J. and Himpsel, F. *Physical Review B* **47**(24), 16441 (1993).

[234] Haag, N., Laux, M., Stöckl, J., Kollamana, J., Seidel, J., Großmann, N., Fetzer, R., Kelly, L., Wei, Z., Stadtmüller, B., et al. *New Journal of Physics* **18**(10), 103054 (2016).

[235] Lebugle, A., Axelsson, U., Nyholm, R., and Mårtensson, N. *Physica Scripta* **23**(5A), 825 (1981).

[236] Schieffer, P., Krembel, C., Hanf, M., and Gewinner, G. *Surface Science* **400**(1-3), 95–108 (1998).

[237] Sanz, J. and Tyuliev, G. *Surface Science* **367**(2), 196–202 (1996).

[238] Chen, J. G., Menning, C. A., and Zellner, M. B. *Surface Science Reports* **63**(5), 201–254 (2008).

[239] Frey, F., Schneider, J., Prandl, W., Zeyen, C., and Ziebeck, K. *Journal of Physics F: Metal Physics* **9**(4), 603 (1979).

[240] Heimann, P., Marschall, E., Neddermeyer, H., Pessa, M., and Roloff, H. *Physical Review B* **16**(6), 2575 (1977).

[241] Miranda, R., Yndurain, F., Chandesris, D., Lecante, J., and Petroff, Y. *Physical Review B* **25**(1), 527 (1982).

[242] Himpsel, F. and Eastman, D. *Physical Review B* **21**(8), 3207 (1980).